Production of Hyperpolarised ^{129}Xe for NMR Spectroscopy and Imaging

by

Elliot Woolley, MPhys

Thesis submitted to The University of Nottingham
for the degree of Doctor of Philosophy

August 2007

Abstract

Hyperpolarised ^{3}He has been used extensively in the neutron community and for magnetic resonance imaging (MRI) of the lungs. ^{129}Xe has many desirable advantages compared to ^{3}He for NMR, namely its chemical sensitivity, solubility, adsorption capability and atmospheric abundance. In this work we present the design and construction of a ^{129}Xe spin exchange polariser that operates at gas pressures between 0.6 and 3 bar. The design incorporates a novel Volume Holographic Grating (VHG) spectrally narrowed, high power laser diode device as the optical pump source for a continuous gas flow cylindrical polarisation cell. Nuclear polarisations of 34 ± 3 % are achieved in ^{129}Xe gas. Magnetisation production factors in excess of 80 % cm^3 min^{-1} are achieved using a pseudo batch-flow operation method. Major parameters affecting ^{129}Xe gas polarisation are discussed and the first measurements of cell heating from laser light absorption by Rb vapour are made. Hyperpolarised ^{129}Xe gas produced from our system is imaged inside a low field, whole body MRI scanner. NMR measurements from inside a human lung are made using hyperpolarised ^{129}Xe. Preliminary work on dissolved solution NMR is presented as are studies on the feasibility of using hyperpolarised ^{129}Xe for porosity characterisation of porous media in low magnetic fields.

Dedication

For my Gem, with all my love.

Acknowledgements

Although one name appears on the title page of this thesis, it is, in reality, the result of the combined efforts of a number of people, to all of whom, I owe a great deal.

Firstly, I would like to thank my supervisors: Dr John Owers-Bradley whose knowledge of this field and whose trust in my ability were quite simply invaluable to my success. Prof. Herman Bachelard who in life taught me how to judge a man, but in death, brought me to realise that I shouldn't. I remember a wonderful mentor who will never know my respect for him. Dr. Mike Barlow is recognised for his work in initiating the project and in procuring and developing laser devices.

I reserve my deepest gratitude for a man who has given me more professional support and encouragement than any other throughout the course of this work. Dr Steven Parnell has helped me nurture my skills and has freely given his time and knowledge when, as we say, the going got tough. I will never be able to thank him enough.

I wish to thank Stephen Boag whose long-term help, reassurance and friendship, I would have found it difficult to have managed without. Marius Mada kindly sacrificed time on his own work to operate the MRI scanner for me. Simon Nankervis has been an electronics support equivalent of a knight in shining armour as well as a good buddy. Neveen Hosny developed and produced instrumental parts of the polariser. Rob Morris and Dr Martin Bencsik provided the sintered glass samples and worked to achieve the associated results. Paul Reynolds helped me in the early days with technical support and in the latter days with technical advice.

Continuing on a professional level, Ian Thexton, Geoff Smith, Dave Holt, Pete Smith, storeman Jeph and Ian Taylor have all aided the work presented in this thesis, so I thank them too. I thank my friends from both the SP-MMRC and Physics, who make hard work a little more enjoyable. I must also acknowledge the funding provided by the Engineering and Physical Sciences Research Council which enabled this research to take place.

As if giving me life and bringing me up wasn't enough, my mother and my father have given me the support and encouragement I have needed throughout my education. I can never repay that to them, but instead, I hope I make them proud. I thank my brothers for allowing me to be the best in at least one thing.

I am eternally grateful for my friends who know nothing about physics, but are always willing to offer their advice, food and beer in appropriate quantities. They know who they are and I thank them so very much.

Finally, words cannot express my gratitude for the continued love and support given to me by my partner Gemma, even when the money stopped rolling in and I turned into Mr Grumpy. I look forwards to our future together.

Contents

Chapter 1

Introduction

The need for hyperpolarised gases in medicine arises from the absence of a convenient medium in lung spaces with which to perform magnetic resonance imaging (MRI) and nuclear magnetic resonance (NMR) measurements. The very low density of protons in the lungs provides very little signal when performing MRI. Motion correction is also problematic using proton MRI to study the lungs. Hyperpolarised gas may be administered to a patient, providing a high signal NMR medium with which to image their lungs and air spaces and perform quantitative measurements of these spaces. Furthermore, hyperpolarised gases have also found uses in material and particle physics, including: the determination of the neutron spin structure function measured by scattering polarised, high energy electrons from highly polarised targets of ^{3}He [1]; studies of surface interactions [2, 3]; studies of fundamental symmetries [4,5]; and as neutron polarisers and polarimeters [6]. For lung studies and neutron filters, hyperpolarised ^{3}He has been used extensively. However the limited global supply of ^{3}He (a by-product of tritium decay) will prevent the large scale introduction of hyperpolarised ^{3}He as a medical diagnostic medium in MRI. ^{129}Xe has many advantages over ^{3}He including an almost unlimited supply (it is naturally abundant), high chemical sensitivity to its environment (^{3}He is chemically inert, which may be advantageous in some studies) and its solubility in a large range of solutions and high adsorption rates onto material surfaces. This makes ^{129}Xe ideal as a functional MRI medium for lung spaces and for the characterisation of porous media using MRI. However, ^{129}Xe has a number of disadvantages with respect to ^{3}He, namely lower NMR sensitivity, shorter storage times in its polarised state and anaesthetic affects on living organisms. These factors should be considered when working with hyperpolarised ^{129}Xe.

Hyperpolarisation describes the generation of highly non-equilibrium nuclear polarisation in selected chemical species that have non-zero spin. Besides a 'Brute Force' method which utilises low temperatures and high magnetic fields to generate large nuclear polarisations in small samples, two techniques exist to facilitate hyperpolarisation in gases. Using these methods enhancements of 10^5 can be achieved in comparison to thermal polarisation of gases in typical laboratory magnetic fields of around 1 T. The first of these hyperpolarisation techniques is metastable optical pumping (MEOP) [7]; an unstable but relatively long lived energy state is stimulated in an atom by a radio frequency excitation. From this state, the atom may be optically pumped to generate electronic polarisation which induces nuclear spin polarisation by collision processes. Although MEOP is suitable for producing high polarisations in ^{3}He, it cannot be used for ^{129}Xe as no convenient metastable state exists. For hyperpolarisation of ^{129}Xe gas, it is necessary to use spin exchange optical pumping (SEOP).

In the early 1950's, the French physicist Alfred Kastler, along with his contemporaries, developed a technique for optically pumping alkali metal vapours [8,9] which facilitated observations of Hertzian resonances in atoms.

For his contributions to this field, he was awarded the Nobel Prize for Physics in 1966. Kastler's work not only identified a method with which to polarise electronically alkali metal vapours but, since light was absorbed and re-emitted in this process, paved the way for the development of Masers and Lasers. In 1960 Bouchiat [10] was the first to polarise the nuclei of noble gases indirectly using an alkali metal as a spin exchange medium. An optical pumping source is used to polarise electronically an alkali metal vapour which transfers its polarisation, via spin exchange interactions, to the nucleus of a noble gas atom. This was the birth of the technique known as SEOP.

A number of well written review papers exist on the spin exchange polarisation of ^{129}Xe gas and its uses [11–15]. The technology for this technique however, is constantly advancing, and these reviews should be used only as guides on the fundamentals of this field.

The motivation for the work presented in this thesis is threefold; the development of a ^{129}Xe SE polariser based on new high powered, narrow linewidth optical pumping lasers facilitating the use of more efficient low pressure regimes; the application of hyperpolarised ^{129}Xe gas for *in vivo* medical imaging; and the characterisation of porous material using hyperpolarised ^{129}Xe. A brief overview of these motivations is given below.

Historically, SE polarisers have been operated at high gas pressures which facilitated matching of the alkali metal absorption spectrum to the emission of available broadband lasers (pressure broadening). High pressure polarisation cells are generally spherical (optically inefficient), lead to fast relaxation rates of the polarised gas and are liable to rupture. With the advent of high power laser diodes, a number of spectral narrowing techniques have been developed which allow the use of low pressure polarisation cells. Low gas pressures enable higher overall polarisation of ^{129}Xe gas at high flow rates. Hersman and Ruset [16] have shown that the use of low gas pressure facilitates high production rates of hyperpolarised ^{129}Xe in their SE polariser. We have designed and built a continuous flow polariser that operates at mid-range pressures (between 0.6 and 3 bar) and incorporates a frequency narrowed high powered laser diode.

Human lung imaging has been carried out using ^{3}He MRI for a number of years. Quantitative studies of the lung have been made using diffusion and relaxation measurements of hyperpolarised ^{3}He. More recently, hyperpolarised ^{129}Xe has been used in lung imaging studies but the potential of ^{129}Xe has not been fully investigated in this difficult to probe environment. The ability of ^{129}Xe to perfuse into the blood stream through the human respiratory system is expected to enable mapping of the oxygen uptake of lungs with the chemical shift acting as a means to differentiate between free and absorbed ^{129}Xe gas. For this study, we have access to a dedicated low field (0.15 T) MRI scanner.

The structure of porous materials have been studied using hyperpolarised ^{129}Xe. Correlations between the porous structure and the chemical shift and rate of relaxation of ^{129}Xe have been identified. We explore the possibilities of using hyperpolarised ^{129}Xe in a continuous flow system leading into a high field NMR spectrometer to investigate porous samples. An investigation of porous media was carried out in the low field MRI scanner.

This thesis is divided into six main chapters as follows:

Chapter 2 - Optical Pumping; a survey of laser devices appropriate for the optical pumping of Rb vapour is given. Following this is an outline of the theory behind the absorption of laser light by the Rb vapour and relaxation of Rb polarisation. The spin exchange mechanisms that enable the transfer of electronic polarisation from the alkali metal to the nucleus of the noble gas are explained along with the role of the buffer gases within the polarisation cell. Relaxation mechanisms affecting hyperpolarised ^{129}Xe gas are described.

Chapter 3 - NMR and MRI; the fundamental physics pertaining to nuclear polarisation are discussed with relation to hyperpolarised gases. It is shown how the nuclear polarisation relaxes over time and how the excitation of bulk nuclei may be modelled. The chemical (resonance) shift of nuclei is described and the chapter concludes with a brief description of MRI techniques relevant to the work carried out in the experimental section of this thesis.

Chapter 4 - ^{129}Xe SEOP Experimental Design; the design of our SEOP apparatus is presented in detail. Each component of the polariser is justified and the operation of the system explained. This chapter also contains details of cell production and preparation and laser safety issues are considered.

Chapter 5 - SE Polariser Characterisation; the two-stage, low field polarisation calibration method used in this work is outlined. The operational parameters of temperature, laser power, cell pressure and gas flow rate are discussed and optimised for hyperpolarised ^{129}Xe production. The effects of thermal runaway of Rb vapour within our SE cell are also presented.

Chapter 6 - Imaging of Hyperpolarised ^{129}Xe for Medical Studies; hyperpolarised gas sample production procedures are described as well as delivery of the gas to a volunteer. Details of the whole body scanner and NMR arrangement used our investigations are presented. Images from gas samples and NMR spectra from within a volunteer's lungs are presented and discussed.

Chapter 7 - ^{129}Xe in Liquids and Porous Materials; the sample production of hyperpolarised ^{129}Xe inside porous materials and dissolved in liquids is described. NMR and MRI results from ^{129}Xe in these environments are presented and discussed.

General conclusions, implications of our results and an outline of future work are presented in *Chapter 8*.

Chapter 2

Optical Pumping Theory

Many factors determine the level of polarisation achieved in a gas when using the spin exchange optical pumping technique; power and spectral width of the pump laser, alkali metal vapour density within the polarisation cell, gas composition and level of impurities within the system are to name but a few. It is therefore needless to say that a great deal of consideration should be given to the design of a new SEOP apparatus to attain the highest possible polarisation of gas.

This chapter explains some of the fundamental physics and techniques behind SEOP and also describes some of the more recent developments enabling higher and faster polarisations in applicable noble gases.

2.1 Lasers for Optical Pumping

Probably the most vibrantly advancing area of optical polarisation lies within the domain of laser devices. In SEOP, laser light is required to polarise electronically an alkali metal vapour in the proximity of the gas to be polarised. It is this electronic polarisation from the vapour that transfers to the nuclei of the gas in spin exchange (SE) collisions. Generally, if the alkali metal vapour is more highly polarised, this will result in an increase in gas polarisation also. Hence, the desired function of the laser, is to polarise this alkali metal vapour as effectively as possible, which generally dictates that higher powers and narrower emission spectra are desirable, whilst optical pumping cell design, gas composition, pressure and temperature remain important for good polarisation.

2.1.1 Spectral Absorption Lines

The most common alkali metal used in SEOP is currently Rb which can be vaporised to a suitable density ($\sim 10^{14}$ to 10^{15} atoms cm^{-3}) at fairly low temperatures and has relatively high absorption and spin exchange coefficients negating the need for hybrid alkali mixtures. Rb can be electronically polarised (see section 2.2.2) using a circularly polarised light source of 794.7 nm to excite the atoms through the *D1* transition from the ground state, with transitions from $m_s = 1/2$ to $m_j = -1/2$ for right hand polarised light (σ^+). The absorption line width of Rb is in the region 18 GHz bar^{-1} [18] or 0.04 nm bar^{-1} at 795 nm. For this reason, research groups using SEOP have resorted to using high pressure buffer gases in their polarisation cells to broaden the absorption spectra of their vapours ($\sim$ 0.5 nm at 10 bar) to better match that of the emission spectra from their pumping sources which can be several nm wide. An increase in pressure in the cell leads to an increase in the number of collisions experienced by the Rb atoms. These collisions can supply or remove small amounts of energy at the moment of photon absorption which enables them to absorb a broader range of wavelengths. Pressure broadening is not ideal however since high pressure glass cells have a tendency to rupture. Pressure dependent relaxation of the hyperpolarised gas is also increased, which reduces the length of time the gas may be stored in a polarised state (see section 2.2.6) and decreases the ultimate polarisation achievable.

2.1.2 A Survey of SEOP Lasers

In the 1950's, when the first optical polarisation experiments were being carried out using circularly polarised light from incandescent sodium lamps [8], polarisation of Rb vapour was to a very low level. After the 1960's, with the advent of laser devices, the Ti:sapphire solid state laser (tuneable between 650 and 1100 nm) was eventually incorporated into practically every SEOP setup. The device remained the pumping source of choice for many years with a linewidth of only a few GHz (at an output of several milliwatts of power). Matching the Rb absorption spectra to that of the laser was not difficult and indeed the device lent itself to the low pressure polarisation regime ($\sim$10 Torr) producing small quantities of very highly polarised gas [19]. In more recent years the ti:sapphire laser has been developed and currently modules exist that have output powers in excess of a few watts. Despite this, at atmospheric gas pressures where high production of polarised gases is far easier, the linewidth of the ti:sapphire laser is too narrow to match the available pumping spectrum of the Rb, wasting optical pumping potential.

The late 1990's saw the development of the Fibre Array Packaged (FAP) laser which had a linewidth of a few nm, broader than the highest pressure broadened Rb spectra, but capable of a few tens of watts output power. Using this device it was reasonable to trade off line width with laser power in high pressure, high flow rate polarisers. A further advantage of this system was that it eliminated the need for two large laser devices being incorporated within the polariser: the ti:sapphire was not only a cumbersome object itself, it also had to be pumped by another lower powered laser to stimulate the emission of radiation. The FAP laser however offered a relatively small laser head that was powered by fibre delivery from the main unit which could be positioned more conveniently, away from the polariser, in the equipment control rack.

High powered semiconductor lasers, although first produced in the 1980s, were not really utilised by research groups as pumping sources for hyperpolarised gas production [11, 20] until well into the 90s. Some earlier work on the lasers had resolved the problem that they were not truly tuneable due to mode hopping (black holes) [21]. The ability of microscopic $p - n$ junctions to produce fractions of watts of power and also be aligned in very close proximity to one another allowed the production of diode array bars, housed in a package the size of a match box and capable of producing a few watts of power. The inherent small size and geometry of these semiconductor lasers allowed several lower power devices to be stacked into an array configuration giving rise to a low cost pumping source of a few nm bandwidth, more powerful than the predecessor FAP units, at over 100 watts. In fact despite the broader emission spectra of the laser diode arrays (LDAs), their cost is $\sim$100 times lower than that of the ti:sapphire with respect to output power per nm spectral width. Despite the low cost of LDAs however, they were only slightly more successful than other available pumping sources at polarising ^{129}Xe since their line widths were still generally 1-3 nm, much greater than the broadened absorption widths of 0.1-0.5 nm of even high pressure gas-vapour systems. It was the work of Chann, Nelson and Walker [22] that first demonstrated the frequency narrowing of an LDA using an external cavity feedback method to reduce the spectral full width half maximum (FWHM) of their laser diode to 0.2 nm with only a $<$2 dB power loss.

2.1.3 Frequency-Narrowed External Cavity

The external cavity diode laser (ECDL) configuration is a relatively cheap, effective and reliable way of narrowing the emissions of a broad area diode laser (BAL) to a fraction of its original FWHM with only moderate losses in power. The design is optics based and utilises an optical diffraction grating to feedback light of the desired wavelength into the diode causing it to self-seed.

Before any spectral narrowing of the beam can take place, the divergent beam, typical of any LDA, must be corrected to provide a parallel beam shape for the diffraction grating. Typically the divergence perpendicular to the arrangement of the array (fast axis) is of the order 35° and parallel to the array (slow axis), 10°. The fast axis divergence is normally corrected by a low numerical apperture[1] (NA) aspheric microlens lens affixed directly on to the front of the LDA whilst the slow axis divergence can be corrected some distance further along the z-axis with a cylindrical lens (fig 2.1). Next in the optical setup is an afocal telescope used to maximise the region of feedback grating irradiated by the laser light. A $\lambda/2$ plate is placed within the telescope arrangement to exploit the polarisation sensitivity of the grating and as Babcock explains [26], is a useful device for adjusting the proportion of light fed back into the laser. A spectral narrowing problem arises with LDAs since often a nonlinearity exists in the physical alignment of the emitters in the diode bar called ‘smile’, which means that some light from some emitters will be operated upon a different region of grating. This condition limits the degree to which the spectrum of an LDA may be narrowed. The diffraction grating is positioned at an angle θ to the incident beam where the Littrow feedback condition is [22],

---

[1] The NA defines the angle of light over which the lens is effective.

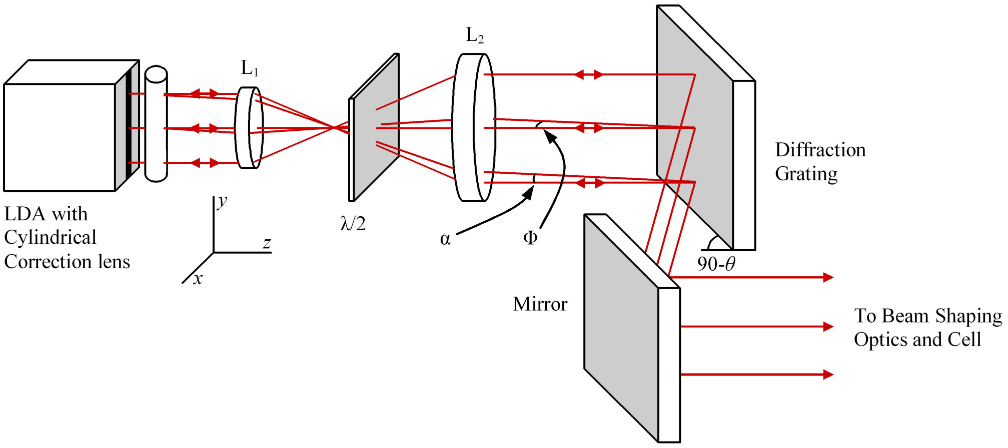

Figure 2.1: Typical ECDL setup. Some example rays have been illustrated. Angles shown are those referred to in equ. 2.1. The length of this setup including the beam shaping optics is typically 1.5 to 2 m.

$$\lambda = 2d\sin(\theta - \phi)\cos\alpha \tag{2.1}$$

where $\lambda_0 = 2d\sin\theta$ and where α is the divergence of light in y and ϕ is due to the smile of the LDA (in the direction x). Divergence in both of these directions limits the effectiveness of the narrowing procedure. The angle θ is required between the incident light and the normal of the Littrow grating and d is the grating's line spacing.

The light returned to the LDA is the first order diffraction from the grating and is ideally spectrally narrow (~0.1 nm). The light retraces its path back into the active region of the semiconductor where the presence of this specific power density $\bar{W}(\omega)$ preferentially induces stimulated emission from select (desired) transitions between energy states. The active region is then forced to lase preferentially at this wavelength from the time that the device is powered on. A steady state output is quickly achieved.

If we consider four energy levels from which permitted transitions may only occur involving ϵ_1 and our feedback wavelength corresponds to $\bar{W}(\omega_{13})$,

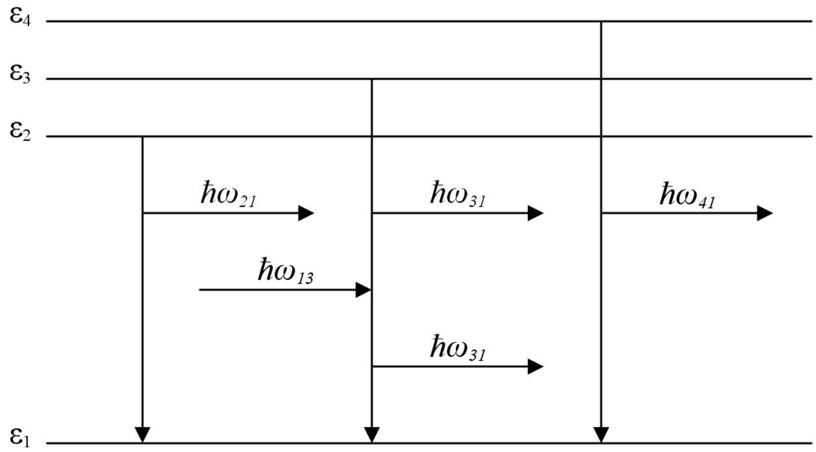

Figure 2.2: Energy transitions as described in equ. 2.2. Light is predominantly produced from $\epsilon_3 \rightarrow \epsilon_1$ transitions which are of a single wavelength.

then the overall change in populations can be expressed as

$$\left(\frac{dN_1}{dt}\right) = A_{21}N_2 + A_{31}N_3 + B_{31}N_3\bar{W}(\omega_{31}) - B_{13}N_1\bar{W}(\omega_{13}) + A_{41}N_4$$

$$\approx -\left(\frac{dN_3}{dt}\right) \tag{2.2}$$

since $\sum_1^4 \frac{dN}{dt} = 0$ and N_2 and N_4 will be small. A and B are the spontaneous and stimulated Einstein coefficients respectively for energy transitions and N is the energy level population (see fig. 2.2).

The narrowed light has a high enough power density to overcome the diffraction of the grating. A mirror is used to direct the reflected light towards the optical pumping cavity. A series of optics are employed to match the beam shape to the geometry and size of the cell.

Power losses caused by this frequency narrowing technique, due to stray reflections and absorbed light, are typically in the region of ∼30% [26] with narrowed linewidths as little as 0.2 nm FWHM.

2.1.4 Volume Holographic Grating Narrowed LDAs

Recently a new device for narrowing LDAs has been demonstrated [27, 28] to narrow the bandwidth of a diode to <0.3 nm [29] with minimal overall power loss. A Bragg type grating is generated in the bulk volume of a glass slide which, in a similar way to the ECDL, feeds a single wavelength of light back into the LDA causing it to self seed (see section 2.1.3). The technology is based on an inorganic photorefractive glass that changes refractive index when exposed to UV light enabling the construction of a volume holographic grating (VHG). This grating is not a multitude of parallel lines but rather a modulation in the refractive index of the glass which facilitates a much lower power loss than narrowing LDAs via the ECDL method. Furthermore, the VHG is a much smaller device (5 × 8 mm) than the conventional grating and requires positioning close to the diode emitters (see fig. 2.3) providing local frequency selective feedback for individual emitters, negating the need to accurately image feedback onto the diode. There is also a significant reduction in the number of optics required which decreases overall power loss through surface reflections. The ability of VHGs to transmit and selectively reflect light efficiently leads to ultimate power transmissions approaching 100% [30].

As with the ECDL technique, it is not necessary for the spectral emission of the bare, unnarrowed diode to be centralised with the ultimate lasing wavelength but simply requires the desired wavelength to be in the device's original spectral footprint. Even if this is not the case, semiconductor diodes can be manipulated by both temperature and current tuning to shift this footprint to include the desired wavelength of light. The VHG itself is quite resilient to current and temperature variations which proves valuable for the overall stability of the device, though fine tuning (~0.02 nm A^{-1} and

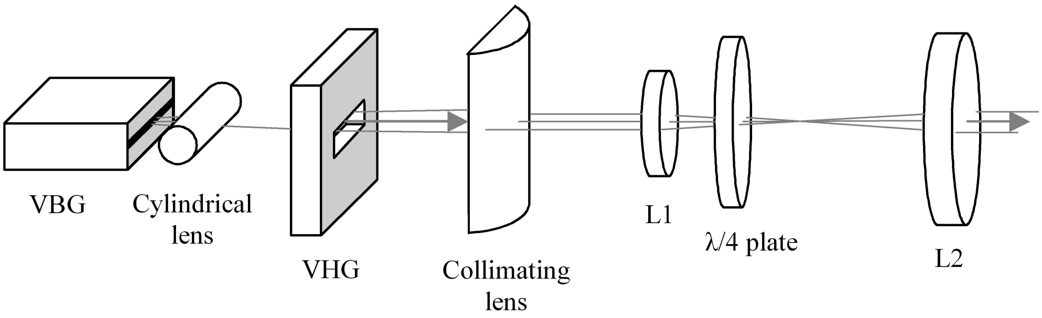

Figure 2.3: VHG setup for narrowing of LDA spectral width. The post-narrowing beam shaping optics (slow-axis collimating lens and telescope) with some example ray paths are shown. The whole arrangement is typically less than 1 m in length.

~0.01 nm °C^{-1} [27]) is still possible.

Although these devices are difficult to manufacture at the precise wavelength desired, they may be rotated slightly to further adjust the feedback condition, but extra losses in power are incurred. Alternatively, Ondax Inc. now make a chirped VHG which has a varying modulation in refractive index enabling the user to adjust the linear position of the device to select the desired feedback wavelength thus ensuring that the device will be suitable for its intended use. This stems from the technology that allows multiple gratings to be implemented into the same volume providing a number of individual feedback wavelengths [31]. Since VHGs exhibit no changes in composition with age, they almost completely eliminate the effects of redshift associated with aging LDAs.

2.2 Spin Exchange Optical Pumping

The optical polarisation of certain noble gases may be performed in either one of two ways: Metastable Optical Pumping (MEOP) or Spin Exchange Optical Pumping (SEOP), but for ^{129}Xe there exists no convenient metastable state from which the atom may be optically pumped. For this reason SEOP is used for the hyperpolarisation of ^{129}Xe, the process being in many ways similar to that for the polarisation of ^{3}He using the same technique. Essentially the ^{129}Xe is 'diluted' within a He and N_2 mixture (which subdues relaxation mechanisms) and an alkali metal vapour which acts as the spin exchange medium. The sample, inside a magnetic holding field (B_0), is then irradiated by circularly polarised light, resonant with an electronic transition within the group one metal vapour, which becomes polarised. This non-thermal polarisation transfers via spin exchange collisions to the nuclei of the ^{129}Xe, whose overall spin vector increases in magnitude in the direction of the externally applied magnetic field. The gas composition and pressure, the absence of impurities and the polarisation cell geometry define the rate of relaxation of the ^{129}Xe nuclei back to the level predicted by Boltzmann's statistics. Using this technique, a gain in polarisation of the order 10^5 is attainable over that induced by thermal excitation in the same static magnetic field. This section aims to give an insight into the SE physics relevant to the main body of work carried out in this thesis.

2.2.1 Rb as a Spin Exchange Medium

Rubidium is just one of the alkali metals that can and has been used for the production of hyperpolarised gases using SEOP. In fact K, Cs were investigated by Zeng *et al.* [32] for use in the production of hyperpolarised ^{129}Xe as early as 1985. Zeng found Cs to have a higher spin exchange efficiency (the number proportion of alkali metal atoms that successfully transfer their polarisation to the nucleus of the noble gas), η_{SE}, than Rb by 10 % although more recent studies [33] have shown this number to be closer to a factor of

1.6 higher at lower B_0 fields. More extensive research has been conducted on the η_{SE} of K and Na for ^{3}He polarisation and rates found to be 0.23 [34] and 0.75 [35] respectively compared to the rate found for Rb of 0.015 [34]. The redeeming factor of Rb against these superior spin exchange efficiencies is its high photon efficiency (the number of polarised atoms per incident photon), η_γ, which renders the overall polarisation efficiency of the metals, κ_{SE}, similar in value, with Rb actually favourable. When taking into account the optical pumping wavelengths required for each of the metals in question, 794.7nm (required for the Rb D_1 line) is the most easily engineered and in available as an 'off the shelf' high power laser diode. This is why the most used and understood alkali metal for SEOP remains Rb though new technologies now enable the production of 894.3nm diode lasers which match the D_1 transition line for Cs and deliver 10 % greater efficiency and have longer operational lifetimes than 794.7 nm diodes [36]. New studies have been conducted into the possibilities of hybrid SEOP which employs the use of two alkali metal vapours, to increase the overall photon and spin exchange efficiencies of the system. An optical pumping source is used to polarise the Rb where κ_{SE} is high and then this polarisation is largely passed on to the second alkali metal (usually K or Na with good η_{SE}) via efficient intermediate interactions and then finally via spin exchange collisions to the noble gas. So far these studies have only been carried out using ^{3}He but promising results of $> 70\%$ polarisations have been presented [37].

2.2.2 Optical Polarisation of Rb

According to its energy level diagram, Rb can be polarised at two separate wavelengths of light, either via the D_1 (794.7 nm) or via the D_2 (780 nm) transition. Absorption by the two lines can be evaluated by comparing the

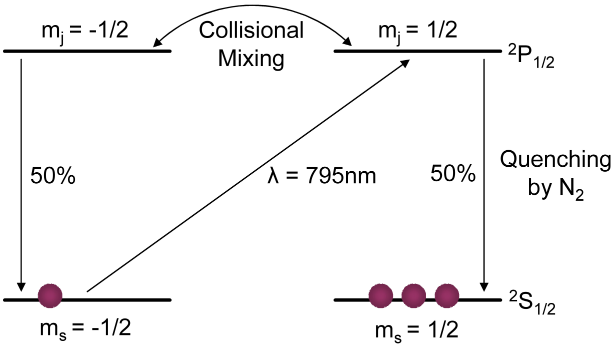

Figure 2.4: A simplified schematic of the D_1 interaction of left (σ^+) circularly polarised light inducing the transition $^2S_{1/2}$ to $^2P_{1/2}$ between two Zeeman sublevels.

products of the maximum absorption intensity, I_{max}, and the FWHM of the absorption spectra, $\delta\nu_{FWHM}$, from similar lasers and optical pumping cells. This reveals D_1 to be favourable [38] and so research groups commonly polarise via this line and reserve the D_2 line for analytical probing. The D_1 transition corresponds to an elevation from the $^2S_{1/2}$ to the $^2P_{1/2}$ state (see fig 2.4) induced by either right or left circularly polarised light. The average photon absorption rate by the Rb, $\langle\delta\Gamma\rangle$, is given by [11],

$$\langle\delta\Gamma\rangle = (1 - \langle S_z\rangle)R_p \tag{2.3}$$

where R_p is the absorption rate for unpolarised Rb atoms, dependent on the pump beam intensity and the absorption cross section of the Rb, and $\langle S_z\rangle$ is the average Rb polarisation throughout the cell. The rate of change of the average total spin is then given by,

$$\frac{d\sum\langle S_z\rangle}{dt} = \frac{1}{2}\langle\delta\Gamma\rangle - \Gamma_{Rb}\langle S_z\rangle \tag{2.4}$$

where Γ_{Rb} is the overall Rb spin relaxation rate. After time, $t = \infty$, the average Rb polarisation in the cell is [39],

$$\langle S_z \rangle_{t\infty} = P_{Rb} = \frac{R_p}{R_p + \Gamma_{Rb}}. \tag{2.5}$$

Thus, when the average polarisation of the Rb tends toward 1,

$$\langle \delta\Gamma \rangle = \Gamma_{Rb} P_{Rb}. \tag{2.6}$$

It is necessary to consider the pumping rate, R_p, to identify the true relevance of the above equations. R_p is dependent upon both the intensity of the incident light, I, and the Rb vapour absorption cross section, σ. I is primarily defined by both the power and spectral width of the laser emission and in a practical sense, also affected by transmission losses due to any beam conditioning techniques and optical windows (eg. the face of the polarisation cell). So the intensity of light entering the polarisation volume is in fact $I(\nu) = I_0(\nu)K_{TL}(\nu)$, where $K_{TL}(\nu)$ is the transmission loss factor for that particular optical setup. Over the length of the cell, L, light intensity decreases as the Rb absorbs light at the front of the cell and less light reaches the rear of the cell. This function is dependent on the intensity of the incident light and the density of the unpolarised Rb vapour, $\delta_U(x, T)$, where T is the temperature in the cell at a particular distance, x, from the front face. If we postulate that the density of alkali metal vapour within the cell is too high, then most of the light will be absorbed near the entrance of the cell and the intensity of light throughout the cavity also becomes a function of this density, which yields,

$$I(\nu, x, T) = \int_{T_{min}}^{T_{max}} \int_0^L \int_0^\infty I_0(\nu)K_{TL}(\nu)\delta_U(x, T) d\nu dx dT. \tag{2.7}$$

If we now consider the Rb absorption cross section, we find that this cross section is not only defined by the frequency of the incident light but also by the velocity of the individual vapour atoms. Kinetic theory of ideal gases states that $\langle \frac{1}{2}mv^2 \rangle = \frac{3}{2}kT$, which means that the average absorption cross section is also dependent on T as well as ν, yielding,

$$R_p = \int_{T_{min}}^{T_{max}} \int_0^L \int_0^\infty I_0(\nu) K_{TL}(\nu) \delta_U(x,T) \sigma(\nu,T) d\nu dx dT \tag{2.8}$$

as the general equation for the alkali vapour pumping rate, R_p.

Since R_p is dependent on both the density of the Rb vapour and the intensity of the laser pumping source it is essential to match these two for optimum performance. It is possible to temperature tune the Rb vapour to match the spectral width of any laser pumping source and temperature-density studies on a range of alkali metal vapours were carried out as early as the 1920's [40]. The temperature at which Rb boils (688 °C) defines a vapour pressure of 1 bar and from this we can deduce the vapour pressure-temperature relationship from the equation,

$$log_{10} P_v = c - \frac{d}{T} \tag{2.9}$$

where $c = 4.147$ and $d = 3957$ for Rb [41]. Then we can relate the number density, N_ρ of the vapour to its pressure by [26],

$$N_\rho = \frac{7.336 \times 10^{-21}}{T} P_v \tag{2.10}$$

where T is the absolute temperature in Kelvin. Figure 2.5 shows the Rb alkali density curve with respect to temperature as well as the curves for other alkali metals. It is regarded that the optimum N_ρ for optical pumping is between 10^{14} and 10^{15} atoms per cm^{-3} which we can see corresponds to a temperature range between 150°C and 210°C.

From the overall pressure of the Rb vapour it is possible to identify the

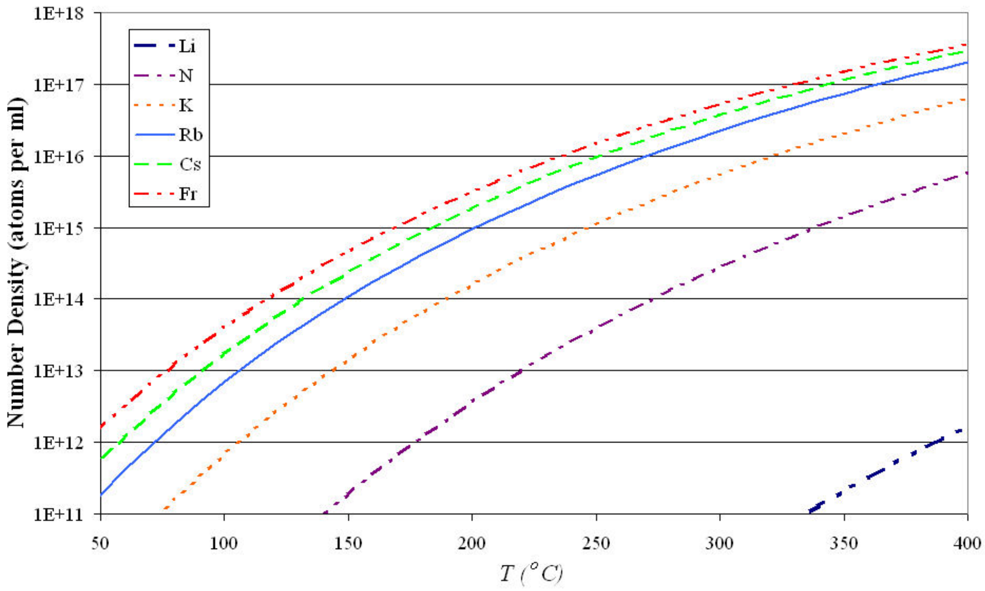

Figure 2.5: Vapour number densities for the alkali metal group with respect to temperature calculated from equ. 2.10. *c* and *d* coefficients used are derived from experimental values quoted in ref. [41]. The curve for francium is produced from extrapolated results.

optimum pumping linewidth given that the absorption linewidth is broadened by 18 GHz bar^{-1} [18] or at 795nm, 0.04 nm bar^{-1}. Pressure broadening of the Rb absorption linewidth occurs due to atomic collisions that either increase or decrease the absorption energy of the Rb atom. The spectral broadening, $\Delta\nu$, is proportional to the collision rate,

$$\Delta\nu = \frac{1}{2\pi\tau} \tag{2.11}$$

where τ is the mean time between collisions. For atoms of mass, m, τ can be defined by,

$$\tau = \frac{1}{4\sigma p}\left(\frac{mkT}{3}\right)^{1/2} \tag{2.12}$$

where σ is the mean free path of the Rb atom. This shows that the absorption spectral broadening of the Rb vapour is dependant on both pressure, p, and temperature, T. k is Bolzmann's constant.

Providing that the spectrum of the laser device is roughly Gaussian (which is true for narrowed sources), the FWHM of the device in nanometres needs to be half the value of the Rb pressure in bars. Any wider than this and light will pass through the cell without being absorbed, any narrower than this and Rb atoms that could potentially be polarised will be left unaffected. As previously shown, the intensity, I, of the light also plays a part in determining the ultimate polarisation of the Rb and consequently, the ^{129}Xe. I needs to be selected for the setup such that a uniform rate of absorption is achieved throughout the cell with the minimum of light leaving the rear of the cell for spectral sampling purposes. If I is too high, then a large proportion of light is absorbed by the Rb vapour near the entry to the cell and this causes localised heating which results in higher vapour densities in that region, absorbing more light and eventually thermal runaway is observed. In this circumstance the front of the cell has large ^{129}Xe relaxation due to increased density of Rb and the rear of the cell is pitched into darkness. If the intensity of light is correct for the cell, practically all of the available photons at 794.8 nm should be absorbed. In this case, the cell is gaining this energy as both polarisation and, predominantly, as heat. Therefore the cell is being heated by the power of laser absorbed by the Rb and this must be considered when selecting the temperature at a cell is conditioned for polarisation.

2.2.3 Relaxation of Rb

Once polarised, the Rb metal atoms are subject to an average lifetime in the higher energy state governed by transferral of polarisation via spin exchange collisions and spin rotation destruction within the cell,

$$\Gamma_{Rb} = \Gamma_{SE} + \Gamma_{sd} \tag{2.13}$$

We shall firstly consider the spin rotation relaxation which is largely determined by four independent mechanisms. Relaxation of Rb due to spin exchange will be dealt with in the following subsection. These relaxation mechanisms are each determined by exclusive parameters which dominate under different circumstances. Of these mechanisms, one that is always present (but not necessarily dominant) is wall relaxation, Γ_{wall}, due to spin interactions with particles within the material of the polarisation cell when polarised Rb atoms collide with the walls. Because wall collisions last a relatively long time (compared to other collisions in the cell), it has been observed [42] that polarisation of the Rb is practically always destroyed in this process. Since the mean rate of collision is proportional to the rate of diffusion of the gas, it is therefore also proportional to the pressure of any interacting buffer gases within the cell. The contribution to the relaxation of Rb due to wall collisions can then be written,

$$\Gamma_{wall} = V\delta_P D_{Rb} \tag{2.14}$$

where V is a constant for the cell geometry, volume and also pump beam geometry, while δ_P and D_{Rb} are the density and the diffusion coefficient of the polarised Rb vapour in the cell respectively.

Rb depolarisation also occurs via short lived collisions with the buffer gases in the cell. The rate of relaxation is therefore proportional to the rate of these collisions and hence the pressure of the buffer gas. We may express the relaxation rate due to buffer gas collisions as,

$$\Gamma_{gas} = N_{gas}U \tag{2.15}$$

where N_{gas} is the number density of the buffer gas in question and U is a constant relating to the cross sectional areas of the two bodies and their mean velocities. Multiple terms exist for this type of relaxation if multiple buffer species are present.

So-called alkali-alkali relaxation occurs in polarisation cells and has previously been attributed to binary collisions since the rate of relaxation carries a strong alkali density dependence. Kadlecek [43] reports however, that this relaxation can be subdued at high magnetic fields which over-rules the previously accepted theory. He explains the difficulty in defining the exact cause of this relaxation.

Finally, a relaxation in singlet dimers in the alkali vapour (these account for about 1% of the vapour) occurs as the nucleus relaxes via the electric quadrupole interaction. This depolarisation is transferred to the polarised electron via the hyperfine interaction. This type of relaxation can also be decoupled by magnetic field but otherwise increases with alkali density and decreases with buffer gas pressure [43].

The total spin destruction relaxation rate can therefore be written as the sum of the above four mechanisms,

$$\Gamma_{sd} = \Gamma_{wall} + \sum \Gamma_{gas} + \Gamma_{alk} + \Gamma_{sing}. \tag{2.16}$$

During the relaxation of a Rb atom, the energy absorbed from the pump beam is be re-emitted in a random direction which can cause depolarisation of other polarised Rb (radiation trapping). This would constitute a secondary relaxation mechanism with a time scale proportional to $\frac{1}{\Gamma_{sd}}$ if it were not for the common inclusion of N_2 as a buffer gas which absorbs (or quenches) the stray light and redistributes the absorbed energy as heat within the cell (see section 2.2.5).

2.2.4 Rb -^{129}Xe Spin Exchange

The key process in hyperpolarisation by spin exchange is the ability of electronically polarised alkali metals to transfer their energy to the nucleus of a noble gas. This is spin exchange polarisation and it occurs by two mechanisms; binary collisions (two body collisions that predominate at high temperature and pressure), and van de Waals interactions (short lived molecules which form at low pressure and in low magnetic fields). A great deal of research has been carried out on the subject of spin exchange interactions, particularly by Happer and his group [11, 13, 32, 44] and this work should be consulted for a detailed account of these mechanisms. In this section we shall consider both mechanisms, their relative merits and their contributions to overall ^{129}Xe polarisation.

Over a period of time, the ^{129}Xe polarisation, P_{Xe}, in the cell asymptotically approaches a percentage of the Rb polarisation, P_{Rb}, described by equ. 2.5. Given that both, binary and van de Waals spin exchange processes occur for polarisation build up, P_{Xe} can be written as [39],

$$P_{Xe}(t) = P_{Rb}\frac{\Gamma_{SE}}{\Gamma_{SE} + \Gamma_{Xe}} \times [1 - e^{-t(\Gamma_{Rb}+\Gamma_{Xe})}] \tag{2.17}$$

where Γ_{SE} is defined in equ. 2.13 and Γ_{Xe} is the total spin destruction rate for the polarised Xe.

The overall Hamiltonian for spin exchange between the polarised alkali atom and the unpolarised ^{129}Xe remains the same regardless of which, if any, of the two spin exchange mechanisms is dominating. The direct transfer of energy from **S**, the alkali electron spin, to **K**, the noble gas nuclear spin occurs with an efficiency, α. Some of the energy from **S** is transferred to **N**, the orbital angular momentum of the two particle system, and this carries a coefficient of γ_t, where, the Breit-Rabi field parameter, $\frac{\gamma_t \mathbf{N}}{\alpha}$, (equal to 3.2 ± 0.3 [32] for Rb and ^{129}Xe), determines the fraction of alkali metal spins **S** which are transferred to rotational angular momentum **N** and noble gas nuclear spin **K**. The Hamiltonian for the interaction is,

$$\boldsymbol{H} = A\mathbf{I}\cdot\mathbf{S} + \gamma_t\mathbf{N}\cdot\mathbf{S} + \alpha\mathbf{K}\cdot\mathbf{S} \tag{2.18}$$

where $A\mathbf{I}\cdot\mathbf{S}$ is the isotropic hyperfine interaction between **S** and **I**, the alkali nuclear spin. The transition described by A serves only to satisfy the condition **F** (the total atomic spin) $= \mathbf{I} + \mathbf{S}$ and has no influence on the spin transfer coefficients.

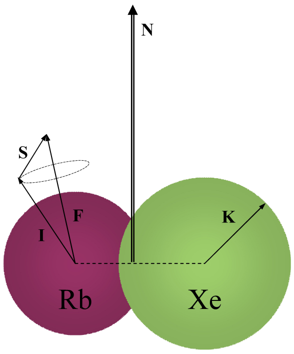

Figure 2.6: Angular momenta referred in by equ. 2.18.

Binary Collisions

Spin exchange via binary collisions arises from simple two-body interactions (fig. 2.7) with fast incident velocities. This is why this type of polarisation transfer applies more strongly to lighter atoms such as ^{3}He rather than heavier, slower atoms like ^{129}Xe, but governs almost all spin exchange at pressures over a few bar. Furthermore, Happer *et al.* [44] showed that the application of a few hundred gauss or more was sufficient to suppress the occurrence of van de Waals molecules and hence any spin exchange in a cell would then be caused purely by binary collisions.

Although these collisions are rapid (lifetime $\sim 10^{-12}$ seconds), the characteristic time scale for alkali nucleonic precession is 10^{-9} to 10^{-10} seconds which means that most collisions do not change the nuclear spin of the alkali metals [45] and so the collisions are often ineffective at polarisation transfer. Above $\sim$ 3 bars of pressure, spin exchange can be treated as purely due to binary collisions, but because these are less efficient then the longer lived van de Waals interactions, Γ_{SE} is reduced with respect to the number of atoms present. At higher pressures, the number of spin exchange collisions per second is greater, which yields faster but less efficient polarisation of gas then

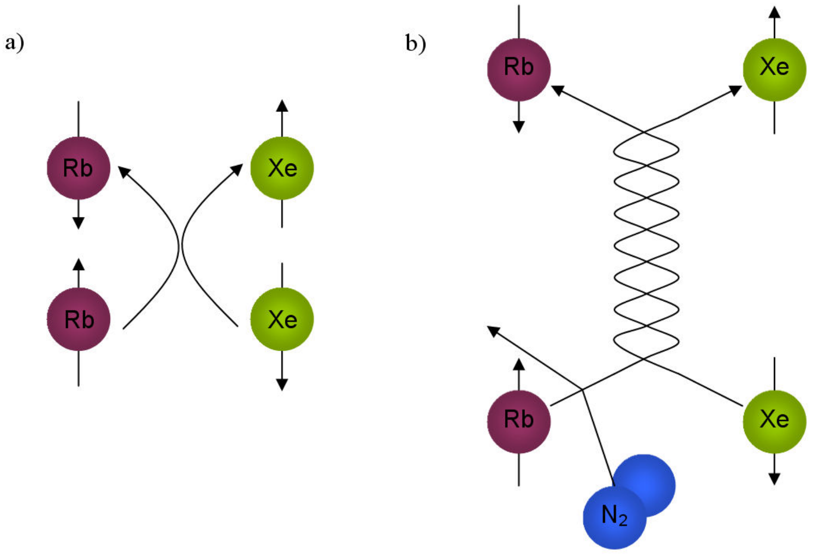

Figure 2.7: a) Classical illustration of a Rb-^{129}Xe binary spin exchange collision, and b) formation and separation of a van de Waals molecule between the two particles and a third body, in this case a N_2 molecule.

by van de Waals collisions.

Binary collisions also occur between Rb and ^{131}Xe which reduces the number of polarised Rb atoms without increasing the polarisation of the ^{129}Xe. This loss in efficiency should be accounted for in the value of Γ_{gas} in equ. 2.15.

Formation of van de Waals Molecules

At low pressures, the rate of polarisation from binary collisions falls due to the reduction of velocities of the gas molecules required for transfer of polarisation. Instead, three (or four) body collisions occur during which van de Waals molecules form (fig. 2.7), offering a more efficient mechanism for polarisation transfer between the Rb and ^{129}Xe atoms. Some research groups prefer to operate at lower pressures to take advantage of this more efficient process, but this is only suitable for small samples [19] or high flow rates [39].

The transfer occurs in three stages; the formation of a molecule via a three body collision, the evolution of the spins during the lifetime of the molecule and finally the break-up of the molecule due to another collision. The spin transfer coefficients in the Hamiltonian, $\boldsymbol{H}$, are dependent on the lifetime of the molecule, τ. The average lifetime of van de Waals collisions is inversely proportional to the number density of the gas, therefore as the pressure in the cell decreases, τ increases and so the efficiency of polarisation transfer also increases. For pressures ≈ 0.2 bar, the average lifetime of the molecules is 10^{-9} to 10^{-10} seconds. Again, if we compare this to the nuclear spin precession time scale, it is reasonable to see that the overall efficiency of the mechanism is still only $\sim 20\%$ at best.

The three body collisions occur most efficiently with N_2 molecules as the third component and so it is important to ensure that for low pressure experiments, the gas composition in the cell contains a reasonable percentage of N_2.

2.2.5 Buffer Gases

In order for effective polarisation of ^{129}Xe to take place, a small number of other gases also need to be included in the polarisation cell. For efficient absorption of laser light, the Rb needs to be pressure broadened and this is generally done by the inclusion of ^{4}He in the cell (0.04 nm/bar at 795 nm) which does not interact with the photons. The inclusion of ^{4}He also decreases relaxation of the alkali metal by reducing the number of wall collisions.

As previously explained, the other gas which is essential during the polarisation of any noble gas by spin exchange is N_2. A polarised Rb atom has only a short lifetime before it decays radiatively back to its ground state. When this does happen, a non-polarised photon is emitted in a random direction which can depolarise other Rb atoms and the overall effect can greatly reduce the overall polarisation of the Rb vapour in the cell. The inclusion of nitrogen in the cell inhibits the depolarisation caused by this stray light by absorbing it. The energy from the light is then redistributed in the cell as heat which can affect the density of Rb present and should be accounted for when controlling the temperature of the spin exchange oven. Failure to do this may result in thermal runaway (see section 2.2.2). As the partial pressure of N_2 increases, the probability of radiative decay decreases and is given by [46],

$$\omega_\gamma \approx \frac{3}{3 + 750 p_{N_2}} \tag{2.19}$$

where p_{N_2} is the partial pressure of nitrogen in atmospheres at 300 K. The amount of N_2 required in a system therefore is determined by the vapour pressure of the Rb and not by the ^{129}Xe concentration.

Obviously as the partial pressure of buffer gases increases, the relaxation of ^{129}Xe due to interactions with these species will also increase though the relaxation due to wall collisions will be reduced which generally accounts for the majority of the depolarisation. The inclusion of buffer gases in the polarisation cell is certainly essential if the largest gains in polarisation are to be achieved via the spin exchange method.

The exact gas composition required depends upon the pressure regime in which it operates and the application requirements of the polarised gas. In the case of high pressure regimes (∼10 bar) a common composition is 1% Xe, 1% N_2 and 98% ^{4}He [20] as the p_{N_2} remains high at low concentrations but for lower pressure regimes (∼1 bar), the optimum N_2 percentage is larger. Fukutomi *et al.* [47] showed that at low pressures, 10% nitrogen concentration produced the best magnetisation of gas in a flow system. Groups which operate at very low pressures (a few mbar) and are interested only in the ultimate polarisation of the gas, omit the ^{4}He and use only N_2 as a buffer gas to increase p_{N_2} to a maximum [19]. In general, p_{N_2} is required to be 0.1 amagat for effective radiation trapping of the Rb to occur[2].

The concentration of Xe in the gas mixture will depend on the intended application, but generally ranges from 1 to 10%. A few groups have studied the effect of varying ^{129}Xe concentrations [16, 47, 48] including both natural abundance (26.4% ^{129}Xe) and isotopically enriched (typically 80 to 90% ^{129}Xe) Xe contributions. Using enriched Xe is advantageous as it reduces the concentration of ^{131}Xe which is harmful to the polarisation process of the 129-isotope (increases spin relaxation rates), though enriched mixtures can cost several times that of the natural abundance gases for similar compositions of ^{129}Xe.

2.2.6 Hyperpolarised ^{129}Xe Relaxation

The most desirable quality for a hyperpolarised gas sample to have is a long spin lattice relaxation time, T_1. This is for two reasons, the first being that the polarisation should last long enough to deliver it to the application. The second is that if T_1 is very short and the sample relaxes almost as fast as it polarises, then only low polarisations will ever be attainable in the polariser.

With ^{129}Xe gas, there are two main terms in the overall spin destruction rate,

$$\Gamma_{Xe} = \Gamma_w + \Gamma_{sr} \tag{2.20}$$

where subscripts w and sr refer to wall and spin rotation interactions re-

---

[2] amagat= $\frac{\rho}{\rho_{STP}}$

spectively. Wall relaxation arises from polarised ^{129}Xe coming into contact with the cell wall which inevitably contains impurities which may lead to relaxation of the gas. Wall relaxation is dependent on cell geometry and is directly proportional to its surface area to volume ratio,

$$\Gamma_w = K\frac{A_{cell}}{V_{cell}} \tag{2.21}$$

Where K is a constant defined by the level and type of impurities present on the cell wall and the pressure in the cell. Wall relaxation can be significantly reduced by ensuring that $\frac{A_{cell}}{V_{cell}}$ is as small as possible (which implies the use of spherical cells, but the disadvantages described in section 4.4 should be considered) and also by reducing the effects defined by K. Reducing K can be done by carefully selecting the type of glass used for the polarisation cell and by cleaning and coating the cell with a Xe repellent solution (see section 4.4.3).

Relaxation of ^{129}Xe due to spin rotation interactions occurs by two mechanisms, binary ^{129}Xe-Xe collisions and the formation van de Waals ^{129}Xe-Xe molecules. Until recently the fundamental limit for ^{129}Xe relaxation was considered to be due only to the binary collision interactions which yield an ultimate T_1 of 56.3 ± 2.6 hours·amagat at [49]. In practice, perhaps the longest T_1 measured has been 3.7 hours [50], which is still considerably shorter than the recognised optimum. It has been shown more recently however, that the occurrence of ^{129}Xe-Xe van de Waals molecules significantly reduces the maximum achievable polarisation in samples with densities less than 14 amagat to 4.1 hours for pure ^{129}Xe gas [51]. Spin rotation interactions define a fundamental limit on the lifetime of the gas and as such cannot be circumvented.

The rate of relaxation can hence be written,

$$\Gamma_{Xe} = \Gamma_w + (\Gamma_{Bin} + \Gamma_{vdW}) \tag{2.22}$$

where Γ_{Bin} refers to the ^{129}Xe-Xe binary collisions and Γ_{vdW} refers to the ^{129}Xe-Xe van de Waals molecules.

Chapter 3

NMR and MRI

Nuclear magnetic resonance (NMR) refers to the ability of a nucleus in a magnetic field to selectively absorb radio frequency (RF) radiation. First observed in 1945 [52, 53], NMR has found its largest application in magnetic resonance imaging (MRI), a technology mainly used in medical diagnosis. NMR allows the study of selected isotopes that have non-zero nuclear spin, such as ^{1}H, ^{3}He, ^{13}C and ^{129}Xe.

The aim of this chapter is to introduce the basic idea of NMR and how it relates to hyperpolarised gases. Within this thesis, NMR is repeatedly utilised as a diagnostic tool. A more detailed account of NMR is given in ref. [54].

3.1 Spin

All nuclei have a property called spin which defies accurate explanation by classical mechanics but is a quantum attribute. The spin of a nucleus is denoted by I and the total number of possible spin states is $2I + 1$. Electrons, protons and neutrons each have spin $= \frac{1}{2}$ which permits two possible

Species	Spin, I	$2I+1$	γ (kHz mT^{-1})
^{1}H	1/2	2	42.58
^{3}He	1/2	2	32.44
^{13}C	1/2	2	10.71
^{129}Xe	1/2	2	11.78

Table 3.1: A table showing properties of some common species used in hyperpolarised gas NMR studies.

spin states; $+\frac{1}{2}$ or $-\frac{1}{2}$. Species of interest for optical polarisation generally have nuclei with $I = \frac{1}{2}$ which means that in a magnetic field they have two possible orientations, either parallel or antiparallel with respect to the field direction. Table 3.1 shows the NMR properties of selected nuclei. The total spin angular momentum is given by $I\hbar$ such that the magnitude of the spin angular momentum is,

$$\underline{P} = \hbar\sqrt{I(I+1)}. \tag{3.1}$$

According to classical theory, the magnetic moment of the nucleus, $\underline{\mu}$, is $\gamma\underline{P}$ where γ is the gyromagnetic ratio of the nucleus, a property relating the spin frequency of the species and the magnetic field in which it resides. In a magnetic field, $\mathbf{B}$, the nuclei have an energy, E, equal to $\underline{\mu} \cdot \underline{B}$. For a magnetic field in the z-direction only, we hence have,

$$E = -\hbar\gamma B_z m_I \tag{3.2}$$

where m_I is the spin state of the nucleus. The frequency at which a nucleus spins is related to the magnetic field by,

$$\omega_L = \gamma B_z \tag{3.3}$$

where ω_L is called the Larmor frequency. In a magnetic field, the energy of nuclei in different spin states become distinct by an energy proportional to the magnetic field. This is called Zeeman splitting and the energy difference for two nuclei with a difference $\Delta m_I = 1$ is described by,

$$\Delta E = \hbar \gamma B_z = h\nu \tag{3.4}$$

which agrees with equ. 3.3 and shows that $\nu \propto B_z$ with a constant of proportionality $\frac{\gamma}{2\pi}$. Therefore a frequency, ν, may be applied to a nucleus in a particular spinstate, which provides the correct amount of energy to change the nucleus into another allowed spin state, and that ν is dependent on the external magnetic field, B_z. In this case $\frac{\nu}{2\pi}$ is equal to ω_L.

When a spin system is at equilibrium, the net magnetisation vector lies in the direction M_z with transverse magnetisation components (M_x and M_y) being equal to zero. When a nucleus is exposed to an electromagnetic field with frequency, ω_L, perpendicular to the z-axis, the simple alignment of the nuclei with the field direction is perturbed such that the magnetisation of the nuclei, $\underline{M}$, also contains M_x and M_y components. The evolution of the magnetisations after the excitation pulse are described by the Bloch equations;

$$M_x = \underline{M} \sin\theta \sin(\omega_L t) e^{(\frac{-t}{T_2})} \tag{3.5}$$

$$M_y = \underline{M} \sin\theta \cos(\omega_L t) e^{(\frac{-t}{T_2})} \tag{3.6}$$

$$M_z = \underline{M}[1 - (1 - \cos\theta) e^{(\frac{-t}{T_1})}] \tag{3.7}$$

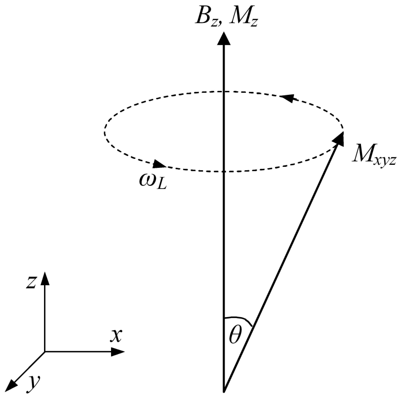

Figure 3.1: Magnetisation precession of a nucleus around an external field B_z with angular frequency ω_L.

where the excitation rotates the magnetisation by angle θ around M_z (fig. 3.1). This means that the magnetisation of the nuclei precesses about z-axis with magnitude $M_x sin\theta + M_y cos\theta = M_{xy}$.

3.2 Spin-Spin Relaxation (T_2)

The lifetime of the nuclear magnetic precession is characterised by the time constant, T_2, which describes the average time taken for the magnetisation in the xy plane to decrease by a factor e. The relaxation in this transverse plane arises from fluctuating magnetic fields generated by neighbouring spins which perturb nuclear spin precession. The macroscopic effect is that the magnetisation in the xy plane decays back into the z direction with some energy loss depending upon the induced excitation of the nuclei. The transverse magnetisation can be described by,

$$M_{xy} = M_{xy0} e^{-(\frac{t}{T_2})}. \tag{3.8}$$

where M_{xy0} is the transverse magnetisation at $t = 0$.

The processes described by T_2 are fundamental molecular interactions and describe the upper limit for the observed transverse relaxation of a precessing magnetic moment.

3.3 Dephasing Constant (T_2^*)

The decay in net magnitude of the magnetic precession is also caused by dephasing of the nuclei as each experiences a slightly different magnetic field. Consider a number of nuclei that have been subject to a 90° excitation pulse and have magnetic moments rotating in the xy plane. In an inhomogeneous magnetic field, the nuclei will precess at a distribution of frequencies, $\gamma \Delta B_0$, with some faster and some slower than the mean. With the passing of time, the faster precessions begin to precede the central frequency whilst slower precessions begin to lag; this is called dephasing. Therefore, the net magnetisation in the xy plane decays toward zero as time progresses and the rate at which this occurs is characterised by the dephasing constant, T_2^*, where [55],

$$\frac{1}{T_2^*} = \frac{1}{T_2} + \gamma \Delta B_0 \tag{3.9}$$

and where ΔB_0 is the variation in magnetic field over the sample volume. In the case of gases, T_2 is long and so the above equation may be reduced to $\frac{1}{T_2^*} \approx \gamma \Delta B_0$.

It is this dephasing that defines the envelope of a free induction decay (FID) from a transversely excited species. It has been demonstrated [89] that the decay of net magnetisation due to this dephasing follows a Lorentzian-Gaussian pattern defined by,

$$M_{xy} = M_{xy0}e^{-(\frac{t}{T_2^*})^{(1+b)^2}} \tag{3.10}$$

where, b, is a constant representing the shape of the experienced magnetic field. If $b = 0$ then the decay of the angle θ follows a simple exponential, but as $b \rightarrow 1$, a deviation from this exponential is exhibited.

A tuned NMR receiver coil in the yz-plane will have a voltage, V_{Rx}, induced in it by the precession of the dephasing nuclei in the x-plane within the pick-up region of the coil (see section 4.6.1). The induced voltage is proportional to the sum of the emfs generated by all of the rotating magnetic fields (from the nuclei) in this region,

$$V_{Rx} \propto \sum M_0 sin\theta sin(\omega_L t)e^{-(\frac{t}{T_2})^{(1+b)^2}} \tag{3.11}$$

where M_0 is the magnetisation of the nuclei at $t = 0$.

3.4 Spin-Lattice Relaxation (T_1)

In proton NMR, the rate at which the nuclei in a sample polarise inside a magnetic field is defined by the time constant, T_1, the time taken for the polarisation to increase by a factor $1 - \frac{1}{e}$. For hyperpolarised NMR, the term T_1 is used to describe the rate at which a polarised sample relaxes back to its non-zero thermally polarised state.

The lifetime of the z-component of magnetisation is defined by a time constant T_1 which describes the rate of spin lattice (longitudinal) relaxation at a fundamental level. This relaxation arises from interactions between polarised and unpolarised nuclei which return the higher energy nuclei to the lower energy state with the energy lost being converted into heat in the spin lattice (the unpolarised nuclei) and surroundings. Under ordinary conditions the polarisation, P, of a sample is determined by its thermal energy and the strength of the applied magnetic field by Boltzmann's statistics,

$$P = \frac{1 - e^{-\mu B_z/kT}}{1 + e^{-\mu B_z/kT}} \tag{3.12}$$

which for low B_z and high T can be shown to be approximate to

$$\frac{\gamma h B_z}{2kT} \tag{3.13}$$

where k is Boltzmann's constant. P can also be expressed as the population difference between the two possible spin states α and β. Hence,

$$P = \frac{N_\alpha - N_\beta}{N} \tag{3.14}$$

where N is the total number of nuclei in the sample. If the polarisation of the sample is increased from this equilibrium, using SEOP for example, then the population N_α will increase to a value $N_{\alpha pol}$. With the cessation of the polarisation process, the population difference will return to equilibrium with the time constant T_1 such that,

$$N_{\alpha pol}(t) = N_{\alpha pump} e^{-(t/T_1)} + N_{\alpha eq} \tag{3.15}$$

where $N_{\alpha pump}$ is the contribution to polarisation from the SEOP process and $N_{\alpha eq}$ is the equilibrium polarisation due to Boltzmann statistics. This is analogous to the decay of magnetisation in the sample,

$$M_z(t) = M_{z0} e^{-(t/T_1)} + M_{zRes} \tag{3.16}$$

where M_{zRes} is the residual magnetisation generated by thermal polarisation.

In reality, T_1 in a gas is not just determined by dipolar coupling to other like spins but also by collisions with impurities within the sample and with the sample container walls. These collisions can be much more destructive and can reduce the T_1 of a sample to a fraction of a percent of its maximum dipolar value.

If over time, the decaying polarised sample is irradiated with regular and identical low flip angle (θ) excitation pulses, then the magnetisation of the sample is found to follow [56],

$$M_z(i) = M_{z0}(\cos\theta)^{i-1}e^{-(i-1)(t_d/T_1)}. \tag{3.17}$$

where i is the sample number and t_d is the time delay between each pulse. Assuming a linear response from a detection coil which has voltage $V_{Rx}(i)$ induced in it and providing $T_1 > t_d$, plotting $logV_{Rx}(i)$ against (i) should give a linear fit from which θ can be deduced for a particular RF field strength.

3.5 Chemical Shift

Chemical shift phenomenon in which a nucleus in a sample, introduced into a particular environment may experience an additional localised magnetic field which has an affect on its Larmor frequency and hence its nuclear magnetic resonance frequency. In an NMR spectrum there may be a distribution of resonance frequencies from identical nuclei.

Let us, for example, take two identical nuclei and place them in a magnetic field, B_z. Both nuclei will have a Larmor frequency in accordance with equ. 3.3, where the magnetic field experienced by the nucleus is a sum of the applied field, any background field and the localised field generated around the nucleus by the orbiting electrons. The electrons, being an orbiting charge carrier, generate a small magnetic field which either increases (eg. electrons in P-orbitals) or decreases (eg. electrons in S-orbitals) the local magnetic field that the nucleus experiences. This is known as nuclear shielding or deshielding depending upon the effect. The resultant magnetic field, including shielding, can then be expressed as,

$$B = B_z(1 - \sigma) \tag{3.18}$$

where σ is the shielding provided by the electron cloud for a particular nucleus.

If the atoms were now to be adsorbed onto the surface of another substance, the charge distribution in the atom's electron cloud will be affected by the proximity of magnetic fields produced by neighbouring surface atoms. This charge redistribution leads to a revised level of nuclear shielding which affects the Larmor frequency of the absorbed atoms. From this adjustment in resonant frequency, it is possible to identify a particular relationship between the adsorbate and the adsorbant. An NMR spectrum will show two peaks separated by a frequency which depends on the externally applied magnetic field and the extent of the effect the bonding to the surface has on σ. So from equ. 3.18 the change in resonant frequency is,

$$\Delta\omega_L = -\sigma\gamma B_z. \tag{3.19}$$

The chemical shift of a nucleus, denoted by δ, is quantified by comparing the frequency change to that of a reference, which in hyperpolarised gas NMR spectroscopy is usually the resonant frequency of the free gas in question. The chemical shift is calculated by,

$$\delta = \frac{(\nu - \nu_{ref}) \times 10^6}{\nu_{ref}} \tag{3.20}$$

and is quoted in parts per million (ppm).

Because of the large electron cloud attributed to Xe, ^{129}Xe exhibits a large chemical shift range of $\sim$7000 ppm [57] (in comparison to ^{1}H which has a chemical shift range of $\sim$12 ppm [58]), it is a particularly valuable tool for spectroscopy of complex or unknown chemical samples. The large chemical shifts experienced by hyperpolarised ^{129}Xe are just another one of its advantages for NMR studies over hyperpolarised ^{3}He.

3.6 MRI

The use of the NMR phenomenon in medical imaging has been one of the greatest advancements in medicine in recent times. The technique takes advantage of the fact that nuclei can be forced to resonate at different frequencies with the application of a magnetic field gradient (equ. 3.3) and also that it is possible to vary the phase of precession of these nuclei giving two dimensions of selectivity over a sample. Introducing a gradient over a sample to selectively excite only a small volume (slice) allows imaging in three dimensions. Consider an object in a scanner that we intend to image. The object has dimensions in the x, y and z directions with z being in the direction of the B_0 field. By applying a magnetic gradient ($-g_z$ to $+g_z$) in this field direction the object is subject to a range of magnetic field strengths $B_0 - g_z$ to $B_0 + g_z$ and therefore has corresponding resonant frequencies. If we now excite the subject with a narrow bandwidth radio frequency, say $BW = \gamma(B_0 - \delta B_0)$ to $\gamma(B_0 + \delta B_0)$ where $\delta B_0 < g_z$, then only a selective slice of the subject will be excited and precess in the xy plane. The thickness of the slice will vary on the pitch of the gradient and the FWHM of the RF excitation.

After the cessation of the RF excitation, the slice selective gradient is switched off and the excited nuclei will continue to precess with uniform frequency and phase. The application of a phase encoding gradient in a second direction, e.g. the x-axis, forces the nuclei in the excited slice to precess with a range of frequencies. Switching this gradient off will cause the nuclei to revert back to their original precession frequency, but now there exists a phase shift over the sample in the x direction, which is dependent on the strength and duration of the applied phase encoding gradient.

The final part of the basic imaging technique, is to apply a read gradient in the final direction, ($-g_y$ to $+g_y$), which is called the frequency encoding gradient and causes a spread of frequencies in the y direction. The excited slice is now encoded in both the x and y directions and so using RF pickup coils, tuned to a narrow frequency band centralised on γB_0, situated in the yz plane, a 1D section of the subject may be read into a spectrometer as a range of frequencies which can be Fourier transformed to reveal the signal intensities of each 'element' along the array.

By systematically cycling the phase gradient through the slice plane, a 2D array of k-space may be constructed, containing the data required to generate a 2D image of the subject. Repeating this experiment for several slices enables the build up of a 3D image of the subject.

Without refinement, this basic technique is impractical since for thermally polarised nuclei, a repetition time of at least 1 T_1 for each pulse and acquire cycle would need to be observed, and for hyperpolarised nuclei, as the polarisation is not readily renewable, a new sample required for each 1D acquisition. To this end, an imaging technique was developed that takes ad-

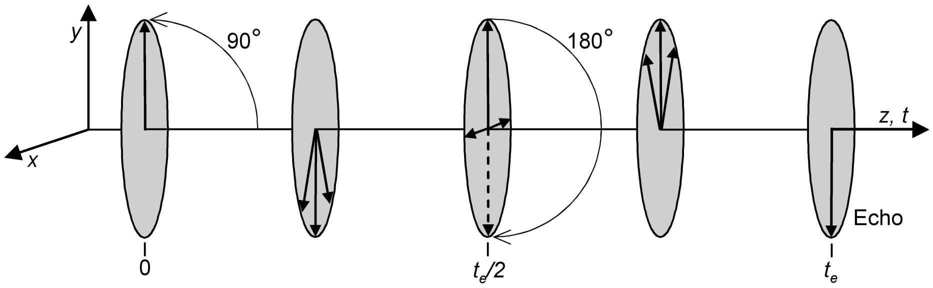

Figure 3.2: Evolution of nuclear spin during echo sequence.

vantage of the fact that an applied gradient will cause dephasing of a group of precessing nuclei (section 3.3), and reversing this effect will cause a spin echo.

3.6.1 Spin Echo

In 1949, Hahn accidentally discovered the nuclear spin echo [59] which forms the basis of the echo planar imaging technique developed by Mansfield [60] and Lauterbur [61] and allows 2D images to be taken using a single imaging sequence [60]. Consider a sample of nuclei in a magnetic field that are subject to a tipping pulse of 90°. In the inhomogeneity of any magnet system, the induced precessional moments will dephase with a time constant T_2^* and the net magnetic moment along the y direction will tend to zero. If after a time $t_e/2$, a 180° pulse (twice the energy of a 90°) is applied to the nuclei, their individual magnetic moments will be flipped by this energy and the faster precessing moments will now pursue the slower precessing moments (fig 3.2). Now after a further time $t_e/2$, all the moments will rephase, and this temporary coherence will induce a signal in a current loop. This short term rephasing is called a spin echo and the value of t_e can be engineered by the application of a suitable gradient in the B_0 direction.

The real usefulness of the spin echo arises from the fact that many echoes may be generated from a single 90° excitation followed by a train of 180° tipping pulses, each with an associated echo. Providing that the time between each 180° pulse, t_e, is much less than T_2 for the nuclei, then enough data may be collected in a single sequence to construct an entire 2D or even 3D image [62]. If a slice selection gradient is used for the 90° pulse, then this gradient must be reapplied during any 180° pulses to operate on the appropriate nuclei.

3.6.2 Diffusion Measurements

The ability to measure the diffusion of molecules is very desirable as a lot of information about a sample may be deduced from knowledge of the diffusion coefficient. For example, it is possible to determine the pressure, cavity size [63], and environment [64] of a sample which can be used to correlate results from other studies or make primary measurements.

Diffusion occurs in all substances at temperatures greater than 0 K and arises from natural interatomic collisions due to the thermal (kinetic) energy of the molecules. The result is that molecules do not remain in one position within a substance, but rather diffuse at a rate determined by their velocity and spacing (Brownian motion). Obviously then, the diffusion coefficient, D, of molecules in a solid ($\sim 10^{-8}$ cm s^{-1}) is much smaller then in a gas ($\sim 10^{-6}$ cm s^{-1}). The net diffusion of a stable solid or gas confined to a fixed cavity is 0 over long periods of time but measurements of diffusion on a smaller scale reveals useful information.

Stejskal and Tanner [65] developed a pulsed gradient method for determining the diffusion coefficients of substances with low diffusion. The technique utilises that of the spin echo sequence but applies a short parameterised

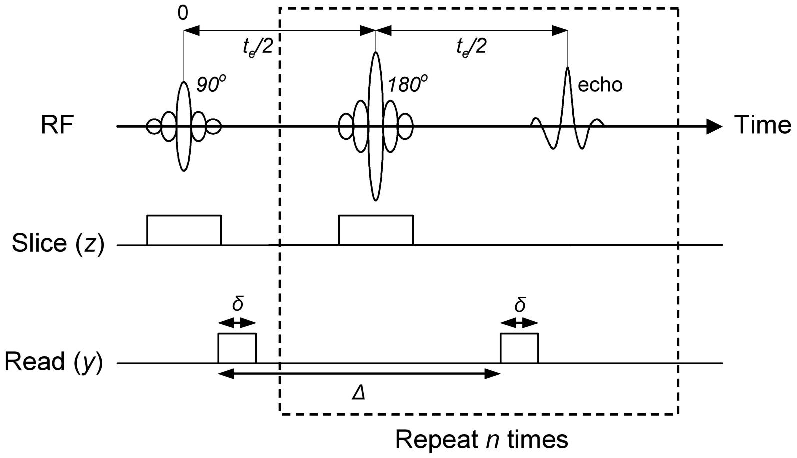

Figure 3.3: Pulsed gradient diffusion imaging sequence.

gradient, G, after the initial excitation (90°) pulse and before each spin inversion pulse (fig 3.3). This encodes each nucleus to its present position in one plane. Slice selection obviously restricts nuclear spin sensitivity to a further plane, making this type of measurement monodirectional. The application of the gradient encodes (generates specific precessional frequencies) the nuclei to a specific location in the (for example) y direction. The nuclei diffuse in the time between gradient pulses, such that when the gradient is reapplied, any nuclei that have moved a significant distance (δy) will be re-encoded by a slightly different magnetic field, and so the magnitude of their echo will be affected accordingly. The decay in the spin echo height can be described by [55],

$$ln\left[\frac{S}{S_0}\right] = -Dn(\gamma\delta G)^2\left(\Delta - \frac{\delta}{3}\right) \tag{3.21}$$

where S is the signal induced in the Rx coil and n is the echo number in the time response. The times described by Δ and δ are defined in figure 3.3. A full derivation of this equation can be found in ref [66].

In gas studies on lungs or porous media it is possible to correlate the diffusion of the gas with the cavity size of the environment in which it resides since the walls of the cavity impede the free diffusion of the gas. For example, the alveoli of the human lung are of the order 3×10^{-4} cm^3 whilst the free diffusion coefficient of ^{129}Xe (100%, 2 bar) has been measured at 2.86×10^{-2} cm^2 s^{-1} [67]. The mean displacement, $\bar{x}$, of a particle in one direction can be determined from the diffusion coefficient using,

$$\bar{x} = \sqrt{2Dt} \tag{3.22}$$

which yields $\bar{x}$ to be 0.24 cm in one second, many times the diameter of the alveoli. As this displacement obviously does not occur, this gives rise to an inhibited diffusion value called the Apparent Diffusion Coefficient (ADC). This ADC will naturally vary depending on the size of the cavity (restrictions on motion of the gas molecules) with a maximum value equal to the free diffusion coefficient. This method has been used to study porosity of aerogels using hyperpolarised ^{3}He [68] and of zeolites using hyperpolarised ^{129}Xe [63].

Chapter 4

^{129}Xe SEOP Experimental Design

Historically, SEOP polarisers have been built to operate at the high alkali metal vapour pressures necessary to make efficient use of available broadband optical pumping sources (see section 2.1.1). These high pressure polarisation cells, were limited to stronger spherical designs which do not make optimal use of pump beam geometry, and the increased pressures lead to increased relaxation rates of hyperpolarised gas within the cells. With the advent of high powered spectrally narrowed laser devices, the problems associated with high pressures can be negated. In the low pressure regime considerably higher polarisations can be achieved whilst greater production rates are also possible.

The hyperpolarised ^{129}Xe production apparatus constructed at Nottingham has been designed to work at mid-range pressures (0.6 to 3.0 bar) incorporating a continuous gas flow system with recirculation and Xe freeze-out capabilities. Figure 4.1 shows a picture of the SEOP apparatus with the major components labelled. A high powered VHG frequency-narrowed laser

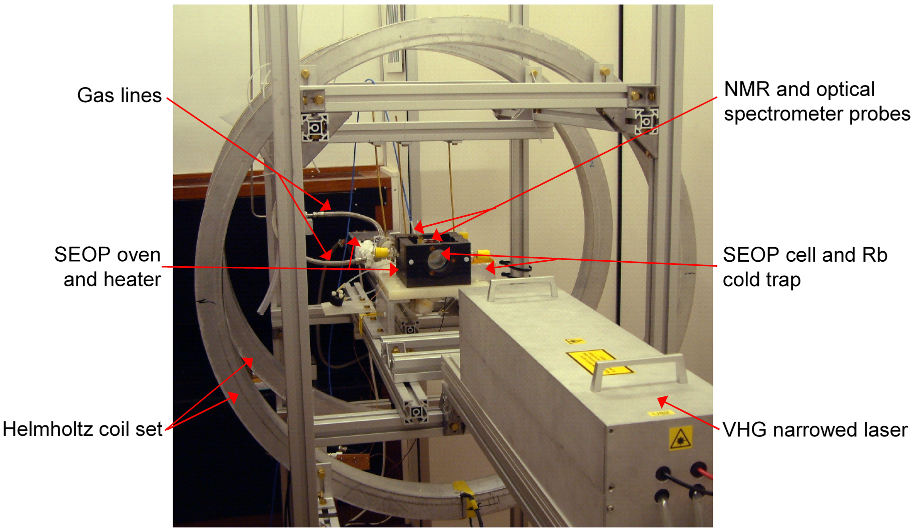

Figure 4.1: Photograph of the SEOP apparatus.

source is incorporated to optically polarise a low density Rb vapour as the SE medium. This chapter gives a detailed description of each of the polariser's major components, focusing on their design and construction whilst the following chapter evaluates and discusses the polariser's performance.

4.1 VHG Narrowed Pump Laser

The relative advantages of using a volume holographic grating narrowed optical pumping source have been discussed in section 2.1.4 and will not be repeated here. The VHG was the device of choice for narrowing our high powered laser diode, which provided the optical pumping source at the heart of our SEOP apparatus. Details of the alignment procedure for our pump laser setup are provided throughout the text. All laser alignment was carried out at the threshold power of the diode and in slightly dimmed laboratory lighting, where fluorescence of the ray tracing card was more obvious. Laser safety goggles were worn at all times during laser activation.

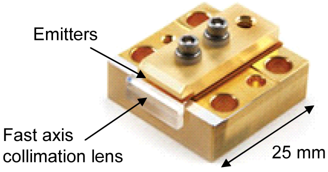

Figure 4.2: Picture of a diode array bar laser device similar to the one used in our ^{129}Xe SE polariser.

4.1.1 Laser Diode

The device used as our photon source is a 50 W 795 nm laser diode array bar (QPC Lasers Inc., California) with an integrated fast axis collimation lens (fig. 4.2). The integrated cylindrical microlens serves to collimate the light emitted from the active region of diode in the direction normal to that of the emitter array where the divergence is typically $\sim 35°$. The diode array consists of 25×200 μm emitters with a total emission length of 10.1 mm The device is powered by an LDC 3065 (Thorlabs Ltd, Cambridge, UK.) laser diode driver which is capable of operating at up to 65 A at 5 V. The power supply has an integrated interlock system that operates on the output of the supply. The switch end of the interlock is connected to the only door of the lab and turns off the laser in the event of unauthorised entry.

The laser diode is both current and temperature tuneable and although the use of a VHG renders fine tuning of the diode unnecessary, the best results are still obtained by narrowing a broad spectrum that is centralised on the desired wavelength. For this reason, the laser diode is mounted on a copper heat exchanger block that is temperature controlled by an MRC 300 thermoelectric recirculating liquid chiller (Melcor Corp., New Jersey). The temperature of the laser can hence be regulated between 2 and 40 °C, but typically is operated at 28.6 °C.

Optical detection of the laser light is made via an Ocean Optics Inc., HC4000 spectrometer which communicates to the laboratory control PC via USB interface. The fibre head of the spectrometer, which incorporates an integrating sphere, is positioned behind the polarisation cell, centralised with the SEOP oven's front optical window (shown in fig. 4.11). Initial alignment of the laser diode was made by activating the diode at low power and using a fluorescence card to trace the beam. The beam, which at this stage is a horizontal line, should pass through the centre of the front and rear optical windows in the SEOP oven. This minimises inefficiencies due to skew pumping [70], where polarised Rb atoms continue to absorb circularly polarised light even in the absence of spin relaxation.

4.1.2 VHG

The VHG for narrowing of our laser source (fig. 4.3), a so called 'LuxxMaster' device [27, 28], was manufactured by PD-LD Inc. Because of the difficulty in achieving precise feedback wavelength conditions from a VHG during manufacture, this PD-LD product was specially manufactured to have a chirped variation of refractive index throughout its plane. This chirped characteristic allows fine tuning of the feedback condition for light back into the active region of the laser diode by adjusting the position on the VHG that the laser light irradiates. For optimal feedback from the VHG, the position and alignment of the grating is critical. To facilitate this fine positioning, the grating was mounted in a six axis optics holder allowing adjustment to the position and angle of the grating in all three Cartesian planes.

With the VHG positioned close to the laser diode, optimisation of the feedback condition was carried out at normal operating power since the grating is not 100% efficient and displays a 0.01 nm/°C temperature drift as it

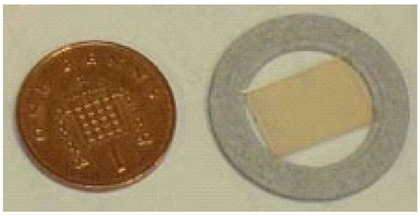

Figure 4.3: Photograph of the feedback VHG used in our laser spectral narrowing setup. The grating is held in a heat resistant Syndanio mount.

heats up. Once the grating's temperature had stabilised (after about 5 minutes), the output of the optical spectrometer was used to identify wavelength matching, line narrowing and maximum transmission by the VHG as it is finely adjusted using its six axis mount. Further details for the alignment of a VHG are presented in reference [69].

4.1.3 Beam Conditioning Optics

Before the laser light is suitable for optical pumping of an alkali metal vapour, two further conditions are required of it; circular polarisation of the light, and matching of the beam shape to the SEOP cell geometry. The first of these is an essential requirement for the success of electronic polarisation of the Rb vapour, and the second is a desirable factor for optimised pumping. The light produced by the laser diode is linearly polarised to a good degree (typically ∼1:100 extinction ratio [71]) and the inclusion of a preconditioning 1/2 wave plate is unnecessary. Therefore, for good circular polarisation of the light, a 1/4 wave plate is introduced into the laser optics at a convenient place (dependent on beam size, shape and spatial intensity), which for our setup was within the afocal telescoping section of the optics where the 1/4 wave plate could experience a good filling factor (fig 4.4).

After the VHG, the laser light is still diverging in the slow axis (in our

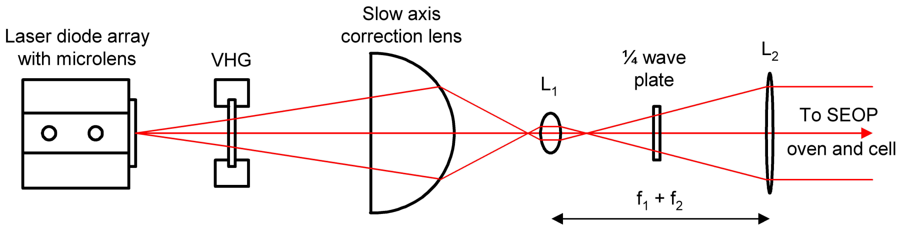

Figure 4.4: Diagram of the laser and optics arrangement with example ray paths. L$_1$ ans L$_2$ are lenses which make up the afocal telescope and have focal lengths f_1 and f_2 respectively.

case, the horizontal plane), and this needs to be corrected in order to focus as much pumping power as possible into the polarisation cell. The collimation of the light in this axis is purposefully over compensated using a cylindrical lens, such that the beam of light converges to a small point some distance after the lens. A short distance further along the central axis of the optics, a short focal length (f_1) convex lens, L$_1$ is placed. The purpose of this lens is to refocus the diverging beam which suppresses any spatial inhomogeneity in the beam. (Up to this point, the beam is mostly confined to the horizontal axis with minimal dispersion elsewhere). On the divergence of the beam from the focal point of L$_1$ the beam shape is rectangular and fairly homogeneous, although it was not quite possible to deconvolve a slightly more intense central line. A final lens, L$_2$, with a longer focal length is used to reconverge the expanding laser light into a parallel beam that best matches the geometry of the SEOP cell. Although the optical spectrometer samples only a small projection of the cell it is assumed that intensity of light achieved there is representative of the whole cell.

The laser diode, VHG, and beam conditioning optics are mounted to a mechanically rigid rail and housed inside a light tight aluminium casing (see fig 4.1). The total length of the laser and optics arrangement is less than

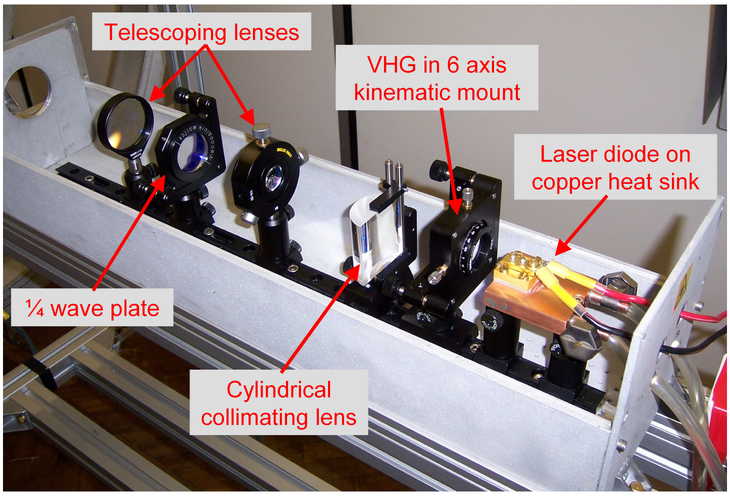

Figure 4.5: Photograph of the VHG spectrally narrowed diode laser as described in the text.

0.5 m, which to our knowledge, is the shortest spectrally narrowed high power laser device used for SEOP. The close proximity and linear alignment of the components in the optical pumping setup means the need for a bulky optical bench is negated and the short rigid mounting offers excellent resistance to vibration and misalignment due to accidental impact.

4.1.4 Laser Safety

The major cause of death in laboratories containing laser devices is due to electrocution caused by leaking coolant systems and high power drive units. To significantly reduce the risk of such an occurrence, a drain, which was left from a previous lab conversion, ensured any major leakages would be carried away from the lab floor and any electrical equipment. Also, a general lab procedure was enforced which ensured all electrical equipment and connections were above floor level. Finally, a built-in cut-out system on the laser chiller unit was designed to shut down the recirculation system in the event of low coolant levels.

The power output of the laser system, 50 W (max), puts it into the laser classification category 4, the most dangerous classification there is. The maximum permissible accidental exposure to the human retina is 1 mW for a CW laser of wavelength 795 nm (calculated from [72]). Obviously, the maximum exposure for our laser exceeds this level by a factor of 50,000 which equates to 1.3 GW m^{-2} over the area of a human retina. Coupling this exceptionally high power density with the fact that the wavelength of the laser system is 794.7 nm, which does not induce a human blink reflex (the human eye responds to wavelengths between 0.4 and 0.7 μm), means that even diffuse reflections from the pump beam could cause permanent damage to the naked eye. For these reasons, a number of safety precautions were implemented to reduce the risk of ocular damage or injury to the skin during laser operation.

For protection against laser radiation, the diode and optics are mounted inside a light tight container except for one orifice which allows access for the pump beam to incident the SEOP cell. During normal operation of the system, a tubular beam guide is placed between the laser housing and the forced air oven. This tube minimises the possibility of accidental interception of the beam by the user and the guide also significantly reduced the probability of scattered reflections from the optical window in the front of the oven. The only other optical path through the oven wall is the optical spectrometer sampling window, and here any possible light path is completely obscured by the spectrometer fibre detection head.

The entirety of the pump beam is therefore enclosed during normal laser operation, but because of regular alignment needs, it was not feasible to interlock each individual element of the beam guide. The SEOP laboratory, a purpose built 15 mm Palight partitioned area of a larger laboratory, has a basic key coded interlock system. The interlock only permits authorised code holders to enter the lab whist the laser is activated. Any entry to the lab without entry of a correct code activates the interlock and switches off power to the laser diode at its supply. This ensures that only fully trained and registered users are able to enter the lab whilst the laser is on. Access to the initiation key for the interlock is restricted to authorised users also.

The final level of protection for users against direct or diffuse radiation is in the form of laser safety spectacles which are worn at all times whilst the laser was activated. The spectacles used for our laser have an optical density[1] of greater than 5 for the appropriate wavelength range which is sufficient to reduce any accidental exposure to a safe level.

The above precautions (not exclusively) satisfied British and university safety regulations for the operation of a class 4 laser product.

4.1.5 Laser Performance

Using the VHG to spectrally narrow the emission from the diode array bar, reduced the FWHM of the output from 1.65 ± 0.01 nm for the unnarrowed diode output, to 0.21 ± 0.01 nm for the emission from the VHG narrowed device. The increase achieved in spectral density by using the VHG is obvious from a comparison of the two spectra shown in figure 4.6. The absorption spectral width of Rb for the pressures of 0.6 to 3 bar that we operate at, gives a maximum absorption width for Rb of 0.15 nm. Clearly the VHG narrowed spectral width of our laser is expected to increase the achievable polarisation of Rb in our cell and hence the achievable polarisation of ^{129}Xe.

The beam shape of the VHG narrowed laser diode emission is shown in figure 4.7 and is a good match to the geometry of our cylindrical cell. The

---

[1] The reduction in light intensity offered by an optical density (OD) is a factor of 10^{OD}.

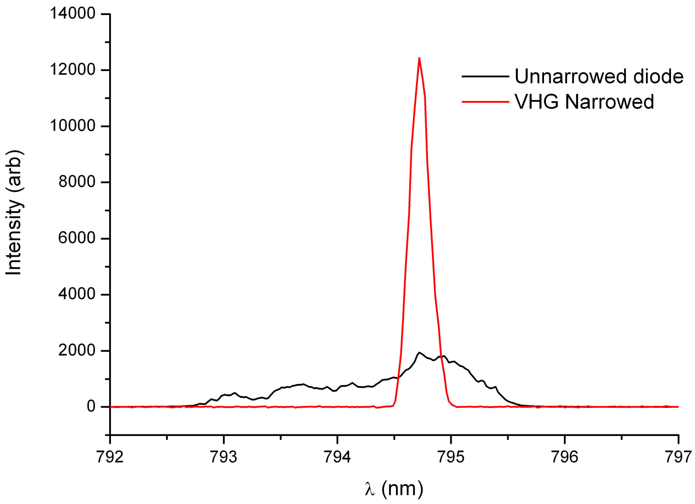

Figure 4.6: Comparison of the pumping beam spectra before and after the installation of the VHG.

power coupled into the SEOP oven from the output of the lasing diode was measured using a laser power meter and plotted (fig 4.8). The transmission efficiency of the VHG and beam condition optics was found to range between 50 and 75 % over operable laser currents which is comparable to findings of Chann *et al* [22] who developed the external cavity narrowed diode laser (ECDL). The decrease in power loss with respect to an increase in operation power is the converse effect to that observed by Babcock [26] who, for his ECDL, found that the power losses become greater with increased laser intensity. This highlights the difference in function between the two frequency narrowing methods and suggests that for even higher laser powers, such as in the work of Zhu *et al* [73], a VHG would yield more efficient spectral narrowing then using an ECDL. The increased transmittance of the optics at high powers is attributed to a decrease in relative reflectivity of the individual components. No significant variance in the FWHM of the narrowed laser spectra was observed over the investigated power range.

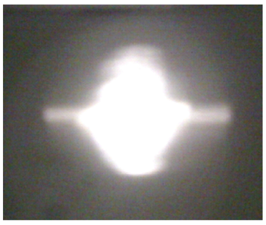

Figure 4.7: Picture of the pump beam profile on entry into the SEOP oven.

With the use of the VHG, ^{129}Xe polarisations of 11 % have been achieved in our uncoated spherical flow cell. This is triple the polarisation level observed in the same cell pumped by our unnarrowed laser diode, but otherwise in an identical setup with the same experimental parameters. Our highest achieved polarisation in ^{129}Xe gas is reported in chapter 5 following optimisation of experimental parameters.

We have shown here, that the use of a VHG to spectrally narrow a laser diode array bar is a simple yet effective method of matching the spectral width of a laser diode to the narrow absorption width of alkali metal vapours. In the current setup it is possible to achieve in excess of 35 W at a FWHM of 0.21 nm with only a 24 % loss in output power. Furthermore, this method of spectral narrowing is mechanically robust, easy to enclose and far shorter than other frequency narrowing methods. It is therefore suitable for compact or transportable SEOP apparatuses.

4.2 Magnetic Holding Field

Essential to the effective hyperpolarisation of noble gases via spin exchange is a magnetic holding field. Typically a homogeneity of 1 part in 10^4 is desirable over the volume of the cell in which polarisation takes place and preferably anywhere the polarised gas may be flushed to and collected. Many number of

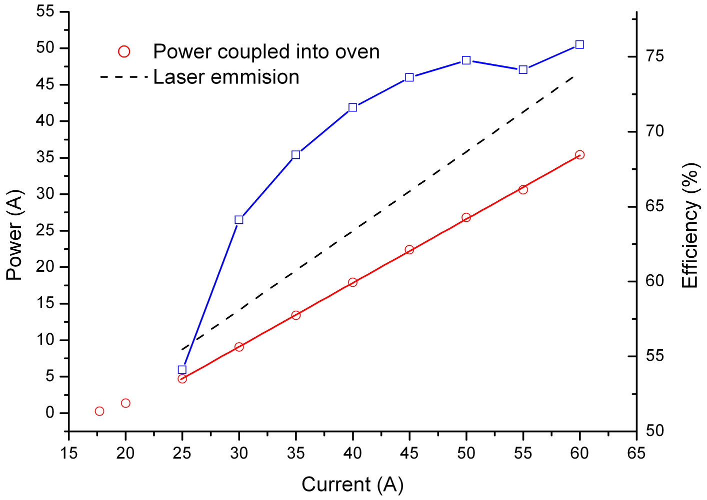

Figure 4.8: Plot of the laser power coupled into the SEOP oven in comparison to the bare diode emission (from product data sheet). The relative efficiency of the spectral narrowing and beam shaping optics in comparison to the emission from the bare diode is shown in blue.

ways have been developed to generate such fields [74–81], but by far the most common method is by using a Helmholtz pair (or set) of coils. These offer a simplistic design and are capable of providing high fields with good regions of homogeneity while keeping access to the polarisation cavity unrestricted.

4.2.1 Theory of Helmholtz

A Helmholtz pair consists of two identical coils of wire with N turns and radius R. An identical current, i, is passed through each coil (wired in series) which are separated by distance R. According to a derivative of the Biot-Savart law, the magnetic field, B_z, due to a current loop at a position z on the z-axis is given by [82],

$$B_0 = \frac{\mu_0}{2\pi}\frac{i\pi R^2}{(z^2+R^2)^{(3/2)}} \tag{4.1}$$

where B_z is in tesla, i is in amperes, z and R are in meters and μ_0 is the permeability of free space. Adapting this for a Helmholtz pair, to find B_0, the maximum magnetic field produced by the coils yields,

$$B_0 = \frac{\mu_0 N i}{R(\frac{5}{4})^{(3/2)}} \tag{4.2}$$

since in this case z=$R/2$. The inclusion of N in equation 4.2 accounts for coils of many turns and not just a single current loop as proposed by the Biot-Savart law. It is also possible from equation 4.1 to produce a model of the magnetic field along the z-axis of a Helmholtz arrangement by taking the reference point of the axis to be z_0=$R/2$ from both coil foci;

$$B_z = \frac{\mu_0 N i}{2R}\Big[\frac{1}{(\gamma^2+\gamma+\frac{5}{4})^{(3/2)}} + \frac{1}{(\gamma^2+\gamma+\frac{5}{4})^{(3/2)}}\Big] \tag{4.3}$$

where $\gamma = R/z$. Theoretically, due to symmetry, along the z-axis any perpendicular magnetic field components are zero inside the Helmholtz arrangement providing there exists no external field. Equation 4.3 models coils of a number of turns with an effective radius R. This radius can be determined for a coil with a cross section of many turns using the ratios [83];

$$\beta_1 = \frac{3-\alpha}{4} = \frac{L_1}{2R_1} \tag{4.4}$$

$$\text{and } \beta_2 = \frac{3\alpha-1}{4} = \frac{L_2}{2R_1} \tag{4.5}$$

where $\alpha = R_1/R_2$ (see fig 4.9). Adding β ratios yields,

$$\frac{L_1+L_2}{2R_1} = \frac{1+\alpha}{2} \tag{4.6}$$

and then finally substituting α gives,

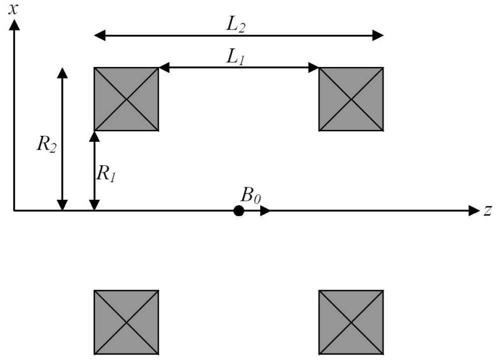

Figure 4.9: Cross sectional diagram of a Helmholtz pair of coils. The dimensions shown refer to those expressed in equations 4.4 to 4.7.

$$\frac{L_1 + L_2}{2} = \frac{R_1 + R_2}{2} \tag{4.7}$$

which is proof that the effective radius for coils with square cross sectional current paths, extends from the origin of the coil to the centre point of the cross section in both the x and z direction. Due to symmetry, the same applies for coils of rectangular cross sectional current paths also.

4.2.2 Helmholtz Coil Design

The Helmholtz coils surrounding the Nottingham SE oven are constructed from rolled aluminium channel sections (3”×2”×1/4”, 900 mm internal diameter) and wound, in house, with 2 mm diameter enamelled copper wire. Each coil has 484 turns and are wired in series to a Kenwood PDS120-6 constant current source accurate to 0.01 A and with a stability of 0.005%. In accordance with equation 4.7, the two coils are mounted at a separation of 480 mm, on a 44 mm Flexlink structural system which uses only non-magnetic components and is mounted on rubber soled feet as a means of vibration reduction. The Flexlink system forms the rigid frame on which the majority of the SE apparatus is attached (see fig. 4.1) including the frequency narrowed optical pumping source.

The background magnetic field in the laboratory exists due to Earth's magnetic field and fringe fields from nearby high field NMR spectrometers in the department. Though it is difficult to completely shield or correct for these unwanted fields in our magnetic environment, two methods of reducing their affect on the B_0 homogeneity in the SEOP apparatus were implemented. The first was to operate at as high field as possible (which is desirable for reduced longitudinal relaxation of the polarised gas anyway), this being determined by the heating of the Helmholtz coils to a safe level ($\sim$ 70 °C). The second method is to shim the magnetic field using a resistor connected in parallel across one coil. This also facilitates more accurate matching of the pair of coils should any difference between them exist. The coils were usually driven by 4.74 A which produced a field of 4.244 ± 0.001 mT at the isocentre of the coil arrangement.

4.2.3 Evaluation of Field Produced by Helmholtz Coils

To probe the field profile generated by the Helmholtz coils the use of a Lakeshore gauss probe, with a resolution 10^{-5} mT up to $\sim$1 Tesla, was employed. The probe was mounted to a linear stage which was driven by a stepper motor and measurements were taken at 1 mm intervals along the z-axis. Figure 4.10 shows a comparison of the measured profile of these coils against the calculated model using equation 4.3. It is obvious from this plot that the coils are at their optimum separation and it can be shown that the field in the centre of the coils is homogeneous to better than 50 ppm over 70mm. For the purpose of cross species calibration (see section 4.6.2, the Helmholtz coil set was also calibrated at operational fields of 4.007, 3.045,

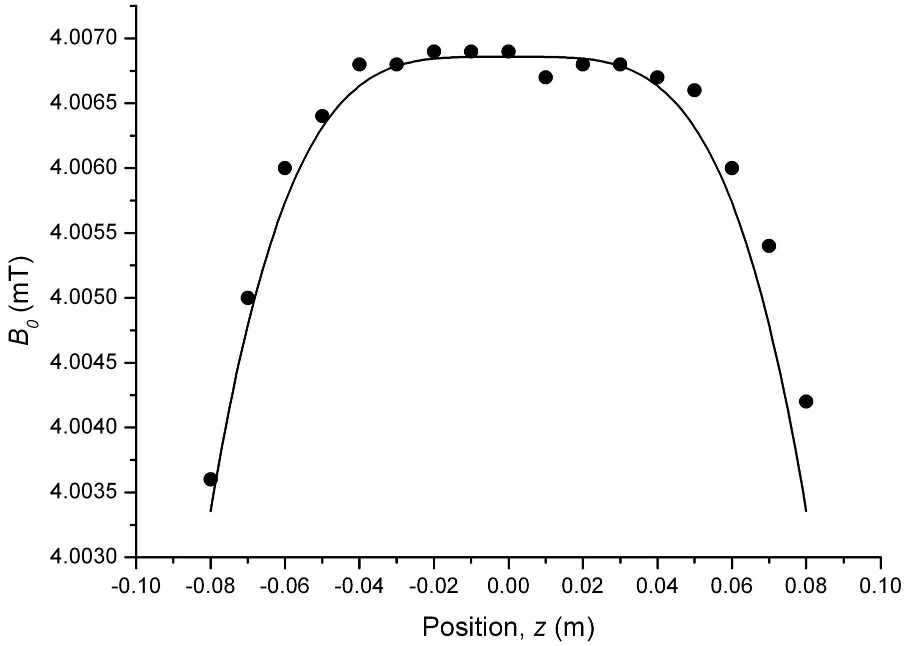

Figure 4.10: Profile of the field generated by the Helmholtz coils along the z-axis. The circles indicate measured data points while the solid line is a model for the coil system generated from equation 4.3.

1.541 and 1.102 mT.

4.3 SEOP Oven

For spin exchange to occur between an alkali metal and a noble gas, the metal must be vaporised such that it obeys the conditions of equ. 2.8 and is dense enough (the required density depends upon the pump laser power) for highly efficient spin exchange. Hence, it is the role of the SE oven to allow homogeneous and accurate heating of the SEOP cell and have facilities for efficient laser beam propagation, optical sampling and access for inlet and outlet gas lines for flow cells.

The SEOP oven and cell for the Nottingham polariser were designed taking into account the relative merits of Hersman's counter flowing low pressure polariser [16] while maintaining the safety issues associated with high pressure systems. The general design of the oven is dependent very much on the geometry of the polarisation cell with consideration for the efficiency of the laser optical pumping and heating of the oven.

4.3.1 SEOP Oven Design

The oven for our SEOP apparatus has been constructed from 20 mm, high temperature Ertalon 66-GF30. This material is a 30% glass fibre reinforced nylon grade plastic offering an increased maximum service temperature of 240 °C as well easy engineering due to increased strength and stiffness. The rectangular oven measures 110 × 100 × 70 mm (l × w × h) internally and incorporates a double glazed, optical window of 50 mm diameter antireflection coated glass. Optical access out of the oven (into the optical spectrometer) is facilitated via a 10mm diameter borosilicate double glazed aperture. The walls of the oven, were designed to be interchangeable to allow for the installation and polarisation of different SEOP cells. In general a new pair of oven sides were manufactured for each design of SEOP cell.

The heat input for the oven is provided by a 400 W in-line process heater (Omega Engineering Ltd.), situated outside of the Helmholtz coil arrangement. Air flow for the heater is provided via the physics department auxiliary low pressure compressed air line. The heated air is introduced through the base of the oven via an inlet positioned in the front right hand corner (see fig. 4.11). The hot air exhaust for the oven is located in the base of the oven diagonally opposite from the inlet. This ensures a good circulation of hot air within the oven and therefore homogeneous heating of the polarisation cell. A type T thermocouple is positioned at the base, towards the

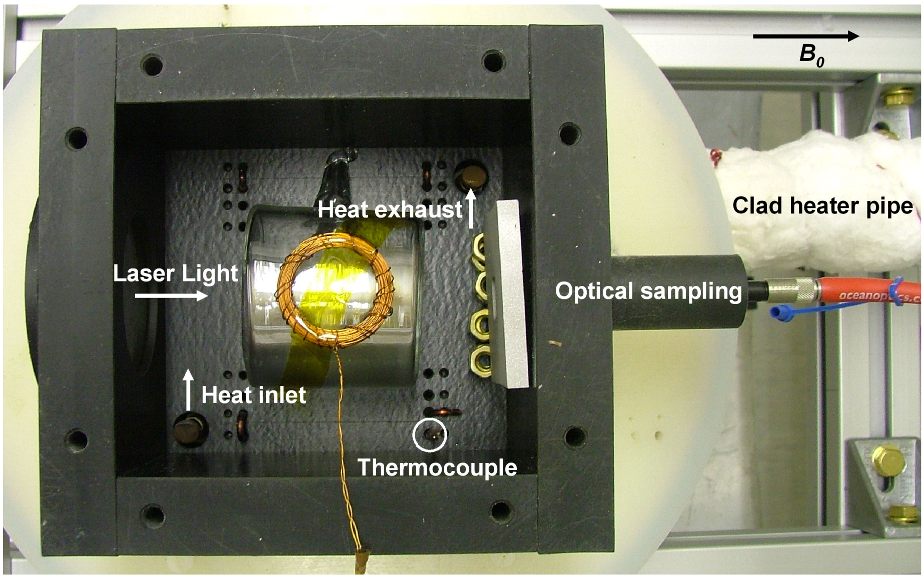

Figure 4.11: A birdseye view of the SEOP oven.

rear of the oven. The thermocouple communicates the temperature of the cell to a CAL9400 temperature controller (Cal Controls) which pulse-width-modulates the power to the process heater through a solid state relay (see appendix A for a circuit diagram of this system). The temperature controller switch and heater power isolator are mounted in the same 19” rack unit, which also contains an RS232 port used for logging the temperature of the oven on a PC, as it heats or cools. The oven is capable of reaching a stable temperature of 140 °C in about 20 minutes.

4.4 SEOP Cells

At the heart of a SEOP apparatus is the SE cell, where hyperpolarisation of ^{129}Xe takes place. The cell contains a small quantity of Rb which provides the vapour required for SEOP when heated. The cell also contains the gas mixture, including ^{129}Xe, to be polarised. Different groups choose to operate their systems at different pressures, generally between 1 and 10 bar (depending to some extent on the laser linewidth) and therefore choose the best design of SE cell to suit their pressure regime: spherical cells provide the mechanical strength for high pressure systems whilst cylindrical cells offer more efficient, homogeneous light propagation. For example, the group of Hersman operate a low pressures of the order 0.1 bar and use a very large (1.8 m) polarisation column which has a cylindrical and a conical section [84]. In general, the quantity of polarised gas required for an application largely determines the size and pressure of the cell. In turn, the cell geometry greatly influences the design of the remainder of the SEOP apparatus.

During this project, a range of SEOP cells were produced and investigated and subsequently used to generate hyperpolarised ^{129}Xe for NMR studies. This section describes the operating regimes of our polariser and gives details of the individual cell designs.

4.4.1 Pressure Regime

Many older ^{129}Xe polarisers utilise high pressure cells as their SE cavity. This is largely due the broad optical pumping sources which were available in the past, which required substantial pressures within the cell to pressure broaden the absorption spectra to match that of the emission from the pump laser. For high pressure systems, thick walled spherical cells are required which limit both the transmittance of light into the cell and the homogeneous pumping of the gas within. Increased number densities of the polarised gas leads to increased spin lattice relaxation also.

It has been shown that low pressure systems are best suited for achieving the highest levels of polarisation in ^{129}Xe [16,19] but even these systems have their drawbacks. Firstly, one requires a very large system else only small production rates may be achieved, whilst the absorption spectrum of the Rb is difficult to match to even with modern frequency narrowing techniques. This renders the optical pumping inefficient. Finally working at pressures of less than one atmosphere introduces the constant risk of contamination from oxygen leaking into the polarisation cell. In the case of contamination, irreversible oxidation of the Rb occurs.

With the above in mind, our system was designed to operate in the mid pressure regime of 1 to 3 bar with normal operation at 2.5 bar. At this pressure we can benefit from excellent matching between Rb absorption and the laser emission spectrum whilst avoiding the risk of detrimental contamination of the system by air. At these moderate pressures we were also able to utilise cylindrical cells without the fear of mechanical rupture. Gas connections to the glass are easier whilst we also benefit in the aspect of safety.

4.4.2 Cell Design

Three sealed Pyrex cells (fig 4.12) were produced such that SEOP optimisation could be performed before the completion of the gas manifold system. The three cells are of different pressures, 0.8, 2.5 and 2.85 bar, all with identical gas compositions (1:10:89 enriched ^{129}Xe (86%):N_2:He) and geometries (35 mm diameter by 50 mm length with 2 mm thick walls and 3 mm thick optical flats). The cells were filled via a dedicated rig at the Rutherford Appleton Laboratory. Details of a similar system can be found in reference [85]. Essentially, Rb is distilled into the cells through an open stem, whilst under very high vacuum (10^{-8} mbar). The gas mixture is then added slowly through a getter filter to the desired pressure. The cell is then flamed off from the rig by sealing the stem which leaves a teat on the side of the cell. This system has been used extensively to generate sealed ^{3}He cells with high

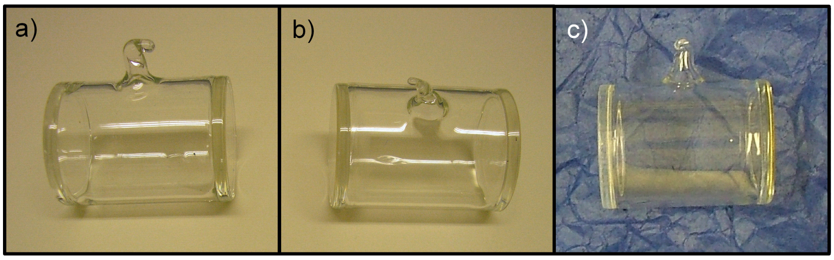

Figure 4.12: Sealed ^{129}Xe SEOP Cells used in this work. a) Xe1: 2.5 bar, b) Xe2: 0.8 bar and c) Xe3: 2.85 bar.

Figure 4.13: Photograph of the spherical flow cell.

purity gas, leading to very high polarisation and long lifetimes [86].

Two flow cells were used in the course of this study, the first was a spherical cell designed and produced by the Institute for Cancer Research, Sutton, and is a replica of their high pressure cell. The cell has two ports on either side of a 44 mm spherical bulb (fig 4.13). The ports enable gas to be flushed through the cell continuously such that polarised gas may be produced in a flow mode. High vacuum PTFE valves (J. Young Ltd.) allow the cell to be sealed without fear of contamination from atmosphere when not in use. A cold trap U-tube facilitates the capture of any unwanted Rb leaving the SEOP cell through the exhaust, which would contaminate the collected hyperpolarised ^{129}Xe sample.

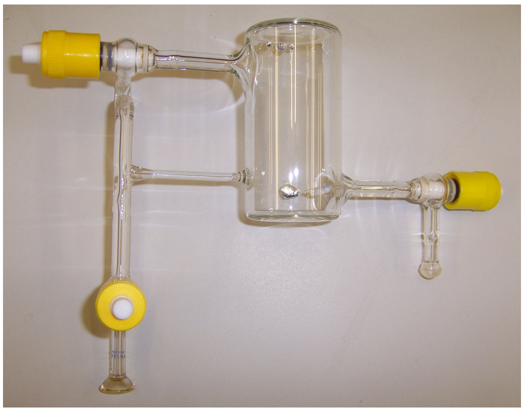

Figure 4.14: Photograph of the cylindrical flow cell. Rb droplets are visible at the base of the cell.

A cylindrical flow cell (fig 4.14) was designed specifically to be incorporated into our polariser. The cell (which measures 50 mm diameter by 100 mm length is manufactured from 2 mm Pyrex) and is positioned inside the SEOP oven in alignment with the external magnetic field and with the optical inlet window. The cell has two ports similar to the cylindrical cell, although the inlet is at the rear left of the cell and the outlet at the front right. This arrangement (fig 4.15) ensures that the front of the cell is the hottest (near the heat inlet) and therefore the highest Rb vapour pressure exists in this region of the cell. Since the laser intensity is greatest here also, the highest polarised ^{129}Xe should be found in this region. As with the spherical cell, the outlet tubing incorporates a Rb freeze out trap to condense any Rb vapour flushed from the cell. Glass pistoned PTFE valves provide the high vacuum seal for the gas ports.

The glass to glass connections on the flow cells are half inch ball and cup joints (J. Young Ltd.). A light application of 'Apiezo H' grease (M&I Materials Ltd.) helps form a vacuum tight seal between the ball and cup mating surfaces whilst in-house made non-magnetic nylon clamps hold the joints to-

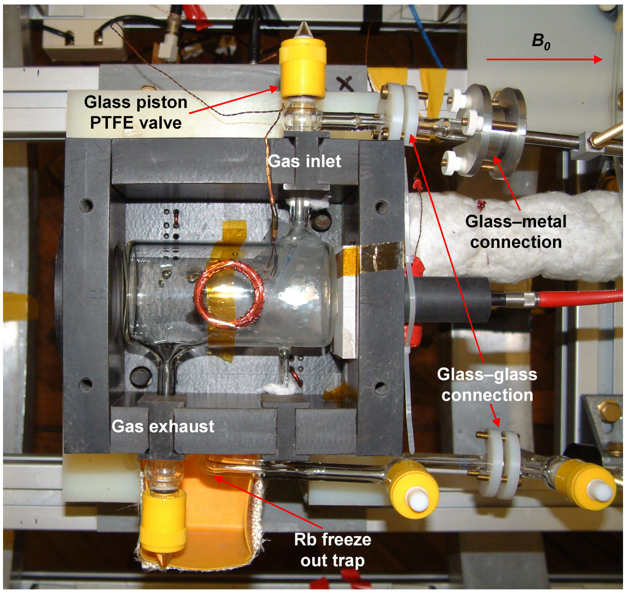

Figure 4.15: Photograph of the cylindrical flow cell installed inside the SEOP oven.

gether for sealing at pressures above 1 bar. Glass to metal interfaces used to connect the glass cells to the stainless steel gas manifold (see section 4.5), are formed by one inch flanges with a locating rubber O-ring, secured by large aluminium compression clamps.

4.4.3 Cell Wall Coating

One of the major relaxation mechanisms within a polarisation cell is due to the interaction of ^{129}Xe with the cell wall. Paramagnetic oxygen atoms contained in the glass wall of the cell provide a mechanism for longitudinal relaxation of the hyperpolarised ^{129}Xe. To reduce the extent of this relaxation, the flow cells used during this project were coated using a solution containing octadecyltrichlorosilanes (OTS) which consist of long hydrocarbons with trichlorosilane at one end. In the process of cell coating, the trichlorosilanes are bound to the silica in the glass which leaves the hydrocarbon chain forming the inside wall of the cell [87]. These hydrocarbons allow collisions from polarised ^{129}Xe atoms with a much reduced relaxation rate.

By coating our flow cells with OTS a significant enhancement in the T_1 of polarised gas was observed. The T_1 of the gas was increased from less than one minute for an uncoated cell to over 15 minutes once the cell walls had been coated.

The remainder of this subsection describes the OTS coating procedure carried out at Nottingham for our 200 ml cylindrical cell, but is largely based on the notes provided by Walsworth [87] who, in turn, refers to Matt Rosen of the University of Michigan group.

Before coating any glassware, the surfaces must be cleaned thoroughly. If the glassware has just been made and has come straight from the glassblower, it may contain a lot of dust and/or grease. With the valve bodies removed, the cell was rinsed with a laboratory grade degreaser (Teepol) to remove these unwanted particulates and then the degreaser flushed from the cell using tap water. The chemicals used in the cleaning and coating procedure, are toxic and the remainder of the procedure, where possible, was carried out in a fume cupboard and whilst wearing PPE including goggles, a protective lab coat and gloves.

To thoroughly clean the glassware, a highly corrosive ‘piranha’ solution was made by adding 7 parts of sulphuric acid to 3 parts of 30% hydrogen peroxide being careful to mix them in this order to avoid violent reaction. The piranha solution becomes very hot very rapidly and care was taken when pouring the mixture into the glass cell. PTFE tape was used to prevent the solution from unintentionally pouring out of glassware openings. Once filled, the cell was left to soak for about an hour. After use, the piranha solution was disposed of slowly down the sink with copious amounts of running water.

Following this, three rinses of the cell with methanol, followed by three rinses with distilled water ensured that the piranha solution had been completely rinsed from the cell and that the cell was clean and ready to be coated.

To aid the binding of the OTS to the surface of the glassware, the cell is whetted in preparation. This is done by introducing a few drops of distilled water into the cell and swilling them around to distribute small droplets on its surface. A flow of nitrogen for about 5 minutes mostly removes this water but ensures that the cell is not bone dry. The cell was now ready to be filled with an OTS solution made my mixing (for 250 ml) 50 ml of chloroform to 200 ml of hexane and finally adding 0.2 ml of OTS. Because the OTS is stored in a fridge (to prevent oxidation) it solidifies, but is easily melted by immersing the lower part of the bottle in warm water. The small volume of OTS can be difficult to measure with typical laboratory equipment but it has been found that the exact amount of OTS is not that critical. Generally about one fifth of a pipette of 2 ml capacity is used. The solution is mixed well and poured into the cell where it is left to bind to the surface for about five minutes. Again PTFE tape is suitable for preventing the solution from unintentionally pouring out of glassware openings. The OTS mixture was disposed of in a non-halogenated waste bottle. Three rinses with chloroform ensured that any unbound OTS was removed from the cell.

Heating the cell to about 180 °C and evacuating it with the turbo pump overnight eliminates any remaining chloroform and causes polymerisation of the OTS wall coating layer. The cell was now ready for Rb filling.

4.4.4 Rb Filling

For SEOP to occur, an alkali metal vapour is required which means that the metal must be introduced into the SEOP cell. One method of introducing

Rb into SEOP cells is by distillation (used for our sealed samples) and is described by Rich *et al.* [85]. This ‘clean’ distillation method however, is not suitable for flow cells where a greater quantity of Rb is required and where the cell may need to be refilled in the event of contamination. For these reasons, a Rb filling procedure for cells was developed by using a nitrogen purged glove box where oxygenation of the Rb is unlikely to occur during the filling process.

All equipment was passed through the glovebox’s antechamber which was vacuum cycled five times before being opened to the main glovebox area. The cell has one valve removed before passing it through to the nitrogen environment. Inside the glovebox, the Rb ampoule (we use 1 g prescored ampoules, Strem Chemicals UK) was opened by placing it inside a finger of a disposable rubber glove and snapping the top off. The opened ampoule was placed inside a shallow glass bowl and the Rb melted using heat gun on low power[2]. It is important, unless the glovebox has an automated pressure regulator, to have an assistant at this stage to reduce the pressure in the box, as the heating of the gas will increase the pressure and force the user out of the access gloves. Rb liquefies at about 40 °C and so heating does not take long, but the Rb should be heated a little further than its melting point to ensure it is workable for long enough to introduce into the SEOP cell. A pipette was used to pass the Rb into the cell, but the pipette was heated first also, to prevent solidification of the Rb inside it. Passing the Rb filled pipette into the cell body through the opened port, a couple of small droplets (typically $\sim$0.05 g is used) were introduced into the cell. It is at this stage that the success of the OTS coating procedure becomes obvious as the Rb forms small spheres (see fig. 4.14) since the OTS produces a non-whetting

---

[2] The heat gun was initially tested inside the glovebox to ensure no outgassing occurred from its element.

surface. Reattaching the removed valve to the cell and closing it provides a nitrogen filled SEOP cell containing Rb which was passed out of the glovebox for use in the polariser.

The remaining Rb was placed into a suitable airtight container and stored inside the glove box for future cell filling. Glassware contaminated by Rb was placed inside a fume cupboard and the Rb ‘deactivated’ using a destructive solution mixed from 20% isoproponal alcohol and 80% toluene. Under no circumstances should water be used.

4.5 Gas and Vacuum Manifold

An intrinsic part of any gas flow polariser is the gas manifold. It is possible to mix gas compositions from individual isotopic gas bottles in order to generate the best possible magnetisation production rates for particular polarisers. However, we decided to choose specific mixtures for our SE system and to buy premixed gases, which enabled significant simplification of our gas handling manifold. There are published results of investigations using different gas mixtures [47, 48] making it possible to select a suitable mixture for a new system without first having to test a wide variety of compositions. For our polariser, we chose a premixed gas (Spectra Gases Inc.) of composition 3% natural abundance Xe (26.4% of which is ^{129}Xe), 10% N_2 and 87% He.

4.5.1 Gas System

Our manifold was designed by N. Hosny of ICR, Sutton and was built by Chell Instruments Ltd. The tubing for the manifold is 1/4 inch stainless steel and connections are made almost exclusively by Swagelok VCR fittings. The manifold has the capability of two input gas lines, one for our gas mixture

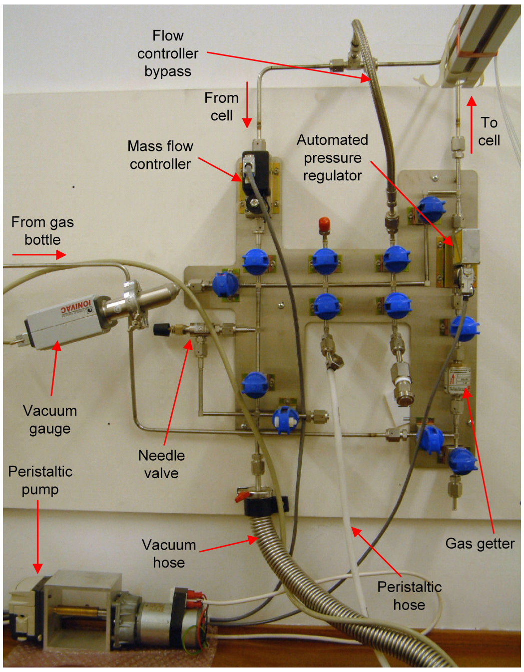

Figure 4.16: Photograph of our gas handling manifold.

and one for a nitrogen purge facility. The second of the lines was actually utilised for a gas recirculation system described in section 4.7.2. The gas from the bottle is purified by an SAES MicroTorr ambient gas purifier which feeds directly into an EL PRESS electronic pressure regulator (Bronkhorst) which is capable of operation between 0 and 10 bar and controls the pressure at which we perform SEOP. The gas mixture is piped a few meters overhead to the SEOP apparatus where the stainless steel gas line is connected to the glassware of the SE cell.

On leaving the SEOP apparatus, the gases are brought back to the manifold by a similar overhead route. On entering the manifold, the gases pass through a mass flow controller (Teledyne Hastings Instruments) which regulates our gas flow through the cell to between 0 and 200 standard cubic centimetres per minute (sccm). On the exit side of the flow controller, the manifold connects to a vacuum system.

4.5.2 Vacuum System

The vacuum in the system is generated by a Leybold PT70 B Compact dual stage pump which incorporates both a diaphragm pump and a turbo pump into the same unit. Because of the acoustic noise and heat generated by the device, the pump is situated outside of the partitioned laboratory, some 4 metres away. This limits the maximum achievable performance of the pump, though pressures as low as 10^{-4} mbar have been achieved. The pressure in the system is measured by a Leybold Ionivac ITR 90 hot ion gauge which is connected to the manifold directly after the mass flow controller (fig. 4.16). Because the system is designed for the continuous flow of new gas and contains a number of connections, the ultimate achievable vacuum by the pump is not generally the limiting factor to the cleanliness of the cell. Small leaks in the system are inevitable but the effect of these on on the quality of gas in the system are reduced by ensuring the system is kept above atmospheric pressure. Although not ideal, the Rb vapour in the cell will also act as a getter for impurities at the ppm level.

The vacuum system is designed such that practically any part of the manifold or glassware arrangement can be evacuated independently. A bypass line has been installed across the flow controller, as evacuating the system through the tiny orifice in the flow device can be a time consuming process.

For cleaning of the gas flow system, the turbo pump is used as with any ordinary vacuum system. However, in flow mode only the diaphragm pump is used to expel the gas from the system protecting the turbo pump from damage by the high flux of gas. In our experience we have found that there is no detrimental affect to the Rb droplets by evacuating the cell for short periods of time using only the forepump through the gas inlet port.

4.6 NMR Spectrometer

The optical spectrometer in a SEOP system is important for the continual monitoring of light absorption by the Rb vapour within the polarisation cell, but the NMR spectrometer is vital for analytical studies of the polarised gas. The optical spectrometer has been described earlier in this chapter. The NMR spectrometer facilitates evaluation of the polariser setup and real time polarisation gas measurements which may indicate faults within the polariser. The NMR spectrometer also enables measurements of longitudinal and transverse relaxation rates of polarised nuclei. A spectrometer design should be such that it does not interfere in any way with the process of polarisation of the noble gas, but is optimised to ensure maximum SNR with low polarisation destruction rates. The basic principles of an NMR spectrometer are relatively simple and are explained in the following section with details of the design of the hardware and software components of our NMR spectrometer.

4.6.1 Spectrometer Design

In principle, an NMR spectrometer consists of two halves; a transmit circuit and a receive circuit. The transmit function is facilitated by an RF pulse generator, a power amplifier to increase the signal to one of high voltage and a tuned set of transmit (Tx) coils. Likewise, the receive circuit consists of a receive (Rx) coil set, a preamplifier and some form of signal acquisition. The transmit and receive functions are carefully timed using a control system. Variations on this theme exist to suit individual needs and different designs of research systems.

The NMR spectrometer used in the ^{129}Xe SEOP apparatus during this

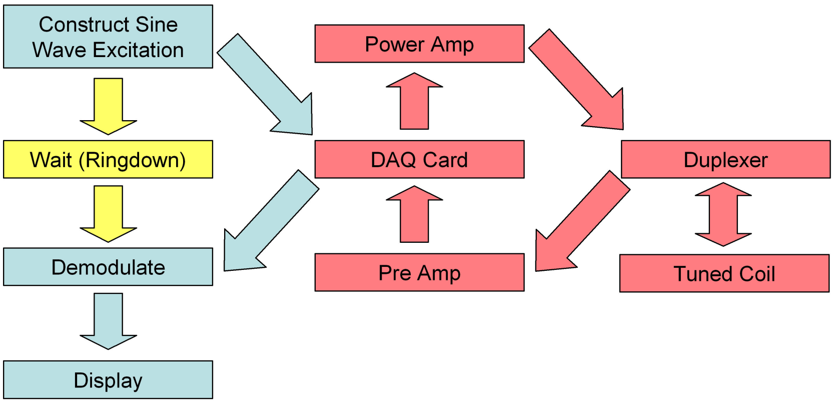

Figure 4.17: A simplified flow diagram of our spectrometer design. The software functions are shown in blue and yellow, whilst hardware is shown in pink.

project incorporated new hardware, designed and built specifically for our frequency of operation and to accommodate our space restrictions and various cell designs. The software for the spectrometer, was an updated version of a LabVIEW based program developed by Fichele for a metastable optical pumping polariser [88]. Essentially, the spectrometer program produces a sine wave excitation at a given frequency for a given period of time (which determines the flip angle θ that the magnetic moment is rotated through) and then waits a user determined idle time before collecting any signal through the receive side of the spectrometer hardware. A similar program and this NMR hardware is described in reference [89]. A flow diagram of our NMR spectrometer's functions is shown in figure 4.17.

The transmit signal is generated by an internal VI (Virtual Instrument) from LabVIEW and sent to a 6111E National Instruments DAQ card connected, via a designated breakout box, to an in-house built 10 W power amplifier. This amplifier has a gain of 10 and a bandwidth of 6 MHz with back to back diodes in series with its output to minimise any low level noise. The power amplifier is connected to a simple purpose designed and built

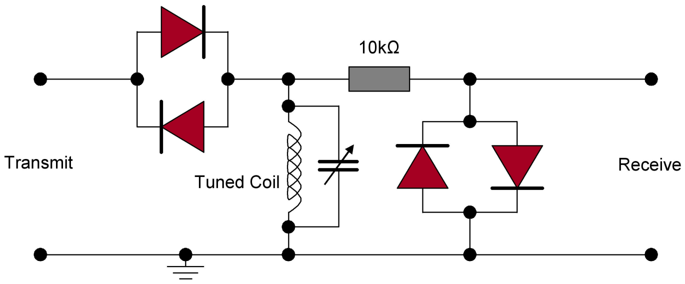

Figure 4.18: Circuit diagram of our low frequency NMR duplexer.

signal duplexer (fig 4.18). The duplexer facilitates the use of a single RF coil to act as both a Tx and Rx coil. Only voltages above 1.2 V, typical of Tx RF signals, are able to overcome the breakdown of the back-to-back diodes (1N4148). Small voltages, less than 1.2 V (*ie.* Rx signals), will only pass to the receive side of the duplexer. This means that high voltages from the power amplifier will only reach the RF coil and the pre-amplifier will be protected, whilst small voltages induced in the tuned coil will only route to the pre-amplifier.

The signal induced in the coil by the precessing nuclei is passed through the duplexer and into the in-house built pre-amplifier based on the LT1222 operational amplifier (G=100, BW=1MHz). The pre-amplifier is connected back to the DAQ card in the computer via the breakout box. The trigger for data acquisition is timed internally from the computer's clock and not from LabVIEW or the operating system as these sometimes have discrepancies. The sample rate of the spectrometer program is at least 10 times that of the base frequency (user defined) and is demodulated by phase detection.

For low amplitude signals (*ie.* low SNR), the spectrometer program has a timed repeat pulse option, which allows several FIDs to be collected at regular intervals. These can then be averaged in a suitable spreadsheet program. This function also allows for the collection of FIDs over long periods to facilitate measurements of long relaxation times.

The tuned RF coil consists of 200 turns of 0.3 mm enamelled copper wire formed around a one inch mandrel. For convenient retuning of the coil for different fields of operation and hyperpolarised species, the coil is parallel tuned (as for a typical Rx coil) using a capacitance decade box. At these relatively low frequencies (10 to 150 kHz), the reduction in SNR normally associated with using a decade box could not be identified. This was verified by tuning the coil with fixed capacitors on a purpose built circuit board. Furthermore, because of the long EM wavelength of such frequencies, the reflectance in the cabling is negligible and hence phase matching of the coil can be omitted. Capacitance tuning the coil in parallel provides a low Q factor for the transmission and a high Q factor for reception of the RF signals. The main advantages of using a single NMR coil are as follows:

- In restricted spaces, multiple coil sets can be avoided
- The coil may be rotated to suit the geometry of the system providing its plane remains perpendicular to B_z
- Effective transmit and receive volumes are identical which avoids inefficiencies due to mismatched sensitivity volumes from multiple coils
- The coil may be positioned directly onto the surface of the cell which facilitates the use of different cell geometries and greatly reduces destruction per NMR pulse of the polarised sample
- For volumes larger than the effective coil pick-up volume, cross calibration of signal is greatly simplified

The last of these points being the most advantageous for a system that uses cells of varying sizes. The important condition being that the volume of gas excitable by the NMR coil is not significantly impaired by the size of the cell to which it is attached. It can be shown for a current loop that the field at a point z along its axis and at a radial distance r is given by [83],

$$B_z = B_0 \frac{1}{\pi\sqrt{\gamma}} \left[E(k) \frac{1-\alpha^2-\beta^2}{\gamma - 4a} + K(k) \right] \tag{4.8}$$

where a is the radius of the loop and $\alpha = r/a$, $\beta = z/a$ and $\gamma = (1+\alpha)^2 + \beta^2$. $K(k)$ and $E(k)$ are complete elliptical functions of the first and second kind respectively. Applying this equation to our coil yields the plot shown in figure 4.19. From this plot it is possible to identify that the excitation volume of the coil is relatively limited to the region close to its turns and along the z-axis. Therefore, providing the coil is always affixed to cells in a similar fashion and that the cell is not smaller than say, twice the radius of the coil, then an equal volume of sample will be excited and detected by the spectrometer during any acquisition. The signal received from the polarised sample is then a function only a function of the sample's polarisation, tipping angle, nuclei density, diffusion and gyromagnetic ratio.

4.6.2 The NMR Signal

When an RF signal is applied to the precessing spin of a nucleus at a frequency equal to that of its Larmor frequency, ω_L, the angle, θ, with which the magnetic moment, μ, precesses around B_z increases (see section 3.1). Once the excitation by RF has ceased, the spin magnetisation relaxes back to its lowest energy state with a time constant T_2. In doing so it can induce an RF electrical signal in the RF coil proportional to the total magnetisation of the sample in the xy-plane, M_{xy}, which is the sum of all the nuclear moments present. Therefore the signal, S, induced in the coil set is proportional to the

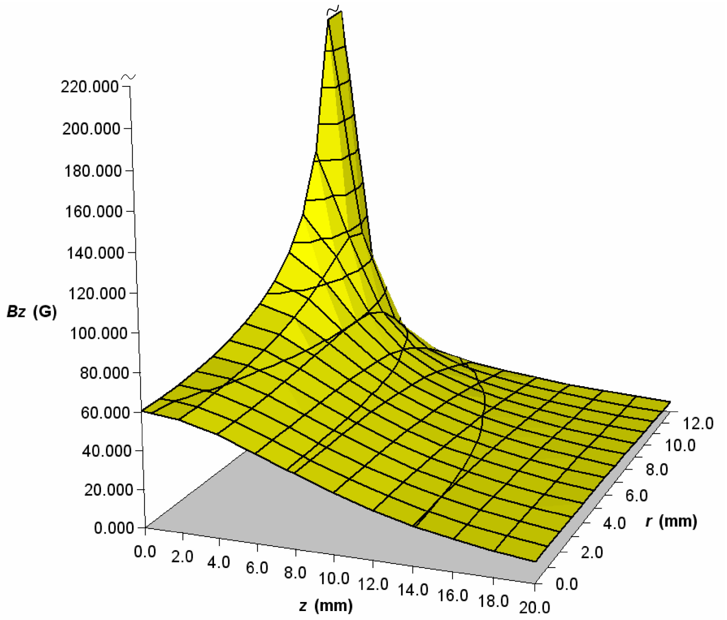

Figure 4.19: Calculated radial and axial field profile from our NMR coil. Note that the top of the plot is clipped. At $z = 0$ and $r = a$ (which lies within the bulk of the coil turns), the field exceeds 500 G.

polarisation, P, of the collection of N nuclei for a given setup,

$$S = AnP\gamma \tag{4.9}$$

where A is a constant for a particular spectrometer setup and n is the nuclei density. For spin $\frac{1}{2}$ nuclei, P is equal to the relative population difference of the two possible spin states as described by equ. 3.14. The energy difference between the two spin states, is equal to $\gamma h B_0$. The polarisation of the same sample in a magnetic field can be predicted by Boltzmann statistics [14],

$$P = \tanh \frac{\gamma h B_0}{2kT} \tag{4.10}$$

where k is Boltzmann's constant and T is the absolute temperature. For $\frac{\gamma h B_0}{kT} \ll 1$, P can be approximated to the expression 3.13. Therefore, using equations 3.14, 4.9 and 4.10, it is possible to calibrate hyperpolarised gas NMR signals with those obtained from thermally polarised samples such as water, which contains a high density of ^{1}H nuclei.

4.7 Hyperpolarised ^{129}Xe Sampling Methods

Three methods were developed for the general sample collection of hyperpolarised ^{129}Xe although the only method used for applications was the pseudo batch-flow method described in detail in section 5.3.6. The other two methods were by the use of a Xe freeze out trap to collect solid hyperpolarised ^{129}Xe and by a continuous recirculation system of the ^{129}Xe in the SEOP apparatus. Both of these latter methods will be described briefly in this section.

4.7.1 Xe Freeze Out

There are two main reasons that make the freezing of hyperpolarised ^{129}Xe desirable and these are the prolonged lifetime of the polarised state and the increased concentration of ^{129}Xe as the Xe is frozen out of the buffer gases which are subsequently pumped away. It is convenient that the solidification temperature of Xe at atmosphere is at 161.4 K and so a liquid nitrogen bath is suitable. It also convenient that the liquid phase of Xe, where very rapid longitudinal relaxation takes place due to very high collision rates between particles, exists only over a very short temperature range (boiling point is 165.0 K). This enables the collection of frozen Xe using liquid nitrogen with little polarisation loss due to relaxation in the liquid phase.

Our Xe freeze out system consists of a coil of 4 mm internal diameter Tygon tubing (fig. 4.20) surrounded by a four pole low field holding magnet

Figure 4.20: Picture of our Xe freeze out coil inside a four pole magnet and liquid nitrogen bath.

immersed in a bath of liquid nitrogen. The polariser was initiated and the flow of gas set at a slow rate (∼30 sccm). The gas mixture containing the polarised ^{129}Xe flows through the freeze out coil. The coil was gradually immersed into the liquid nitrogen (in reality the level of liquid nitrogen in the bath is steadily increased) such that a shallow coating of solid Xe was formed on its internal surface. This ensured that Xe remained as cold as possible, the tubing did not become blocked with frozen Xe and also that the time spent in the liquid phase during freezing and thawing was kept to a minimum. Once the frozen Xe had been collected (generally over 30 minutes), the flow system was shut down and the Xe thawed. Thawing was done by removing the freeze out coil from the holding field and nitrogen bath and swiftly immersing it into a container of boiling water. A gas expansion facility was available in the system to avoid the rapid build up of pressure.

Using this method, a four-fold enhancement in NMR signal has been observed from a sample of ^{129}Xe collected by the freeze out method in comparison to ^{129}Xe polarised and collected without freezing as gas in the original mixture at 2.5 bar. The enhancement in signal is due to the much higher partial pressure of ^{129}Xe. However, a reduction in overall pressure and an increase in relaxation of the gas due to the freeze out process, prevents futher enhancement of the signal strength using the current method.

4.7.2 Recirculation System

With the possibility of using hyperpolarised ^{129}Xe in a high field NMR spectrometer in the adjacent laboratory for materials studies, a polarised gas recirculation system was developed for our SEOP system. The major advantage of such a recirculation system is the reduction in consumption of the expensive high purity gas mixture used for our experiments.

The recirculation of the gas was facilitated by a variable speed peristaltic pump driven by a tuneable power supply. Eight metres of narrow, 1 mm Tygon tubing connects the polariser to the high field spectrometer in the adjacent laboratory. The system pressure is set to 2.0 bar (too high a pressure causes backflush in the peristaltic pump) and the pressure regulator left open to top-up any gas lost through leaks in the system. The peristaltic pump, which operates on the return of the gas from the adjacent laboratory, forces the gas around the SEOP apparatus. The polarisation of the gas is continually monitored in the cell using the NMR spectrometer. An additional NMR coil exists at the return of the gas from the adjacent laboratory to ensure that the gas in the high field spectrometer is still polarised. Outgasing from the peristaltic tubing is a major problem and careful selection of the tubing needs to be made. From our use of MasterFlex C-Flex tubing, severe contamination of the polarisation cell took place and complete deterioration of the Rb in the cell called for complete cleaning and recoating of the cell with replenishment of Rb.

Unfortunately, despite detection of residual polarisation in the ^{129}Xe on its return to the SEOP apparatus from the adjacent laboratory, no ^{129}Xe resonance signal was ever detected in the high field spectrometer. Failure to detect ^{129}Xe polarisation in the high field spectrometer was attributed to repeated vibration problems with the NMR probe.

Chapter 5

SE Polariser Characterisation

The assembly of the spin exchange apparatus for the hyperpolarisation of ^{129}Xe described in the previous chapter, involved evaluation of the system at various stages of construction. Each component of the final design has been characterised and optimised to facilitate maximum polarisation of the ^{129}Xe gas. The previous chapter describes the final design of the polariser and does not concentrate on the functional performance of the system. This chapter gives a more detailed account of the polariser's characterisation and optimisation and in doing so provides information on the operation of the system, whilst demonstrating the process of its development. The work carried out in this chapter is presented in chronological order with a few minor exceptions.

5.1 ^{1}H Thermal Polarisation

A water sample was placed in the centre of the B_0 field generated by the Helmholtz pair which was regulated at 3.045 mT corresponding to a ^{1}H resonance frequency of 129.7 kHz. The B_0 field thermally polarised the ^{1}H in the water sample contained inside a cylindrical Pyrex cell which measures 50 mm length and 50 mm outside diameter with 2 mm thick walls. The water in the sample contains a small amount of copper sulphate which decreases the polarisation time (T_1) of the ^{1}H nuclei. The reduced T_1 enables more frequent acquisition of FIDs from the sample, which is particularly useful when averaging the small signals obtained from thermally polarised water.

The original spectrometer hardware setup, incorporating orthogonal Tx and Rx coil sets, was used to obtain an NMR signal from the thermally polarised H_2O sample. The ratio of signal to background noise was low at roughly 4, but an average from multiple acquisitions could be used to more accurately measure the signal obtained from the sample (fig 5.1). For a ^{1}H 90° excitation pulse, the corresponding peak in the frequency spectrum was found to have a magnitude of 0.369 mV. From equation 4.10, the polarisation of the sample was calculated to be 1.037×10^{-8}.

For a particular NMR coil configuration, the signal obtained from a sample can be calibrated to the polarisation of that sample using equation 4.9 where A defines the sensitivity of the NMR system. For this setup, which is sensitive to sample size because of the fixed coil arrangement, A was found to be 1.253×10^{-29} m^3 V s mT^{-1}.

Because of the relatively short T_2 of the $CuSO_4$ doped water sample, it was not possible to verify the homogeneity of the magnetic field environment using the FID envelope shape (fig 5.1 *inset*). This measurement was made using gas NMR where the transverse relaxation of the excited nuclei is much slower (see section 5.3).

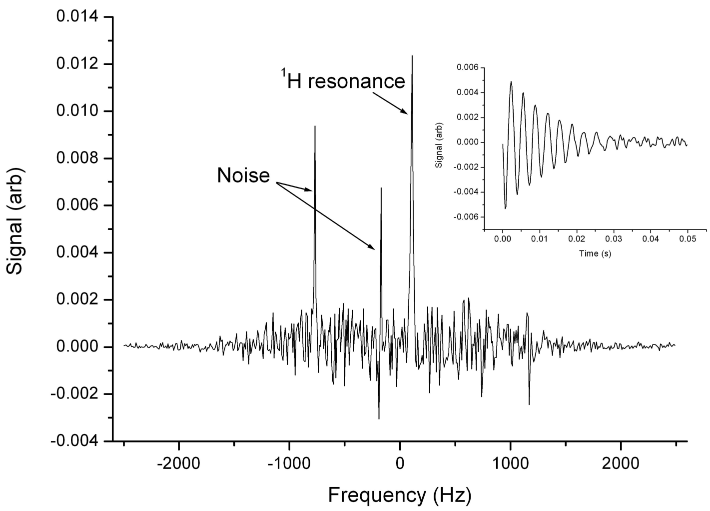

Figure 5.1: An FFT spectrum generated from an average of 254 NMR acquisitions from thermally polarised H_2O. *Inset*, the corresponding FID from the H_2O sample.

5.2 ^{3}He SEOP

Before the production of the sealed ^{129}Xe cells, a sealed ^{3}He cell was borrowed from the Rutherford Appleton Laboratory (RAL) in Oxford. This cell enabled the first test of our apparatus as a spin exchange polariser.

The loaned ^{3}He cell is cylindrical and made from a high purity GE180 aluminosilicate glass, 50 mm length by 50 mm diameter. The cell contains 70 mbar of N_2, 1.93 bar of ^{3}He and a few milligrams of distilled Rb to generate the SE vapour. The increased partial pressure of polarisable gas inside a ^{3}He cell with respect to ^{129}Xe cells partially accounts for the fact that the T_1 of ^{3}He is much longer (10's to 100's of hours) than that of ^{129}Xe. The spin exchange rate between the alkali metal vapour and the ^{3}He gas nuclei is also much slower.

The B_0 field was regulated to 4.00 mT and the ^{3}He cell heated in the SEOP oven to 160 °C, a similar temperature to that used by collaborators at

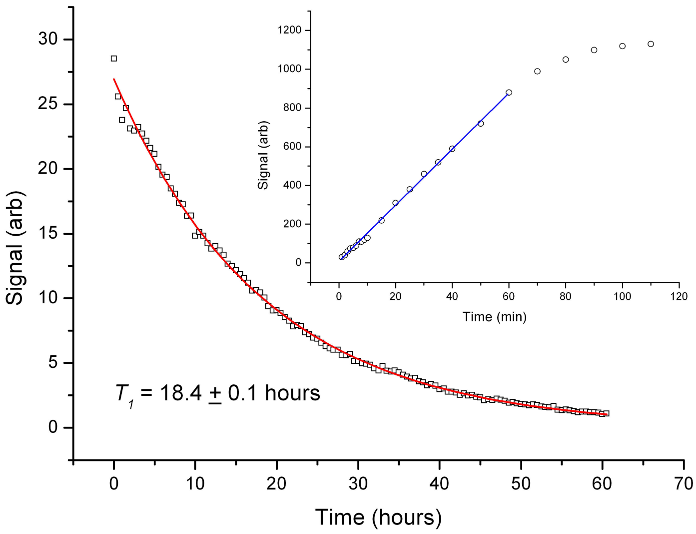

Figure 5.2: Spin lattice relaxation curve of the polarised ^{3}He cell. An exponential model (equ. 3.16) is fitted to the curve. *Inset*, the pump up curve for the same cell. The blue line is a linear fit to the first hour.

RAL for ^{3}He SEOP. The cell was optically pumped using our VHG narrowed diode laser with 35 W output. Regular NMR responses (at 129.7 kHz) were acquired from the cell to attain a polarisation pump up curve for the ^{3}He gas (fig 5.2 *inset*). The pump up curve initially displays a roughly linear relation with time indicating that the rate of polarisation is limited by the number of photons and the SE efficiency and not by the relaxation within the cell. As the cell becomes more polarised, the pump up curve asymptotically converges to a maximum value where the rate of relaxation matches that of polarisation. A spin lattice relaxation measurement is made of the gas in the cell by monitoring the rate at which the NMR signal decays with time (fig. 5.2). A T_1 of 18.4 ± hours is found for the lifetime of the polarised gas in the cell which is comparable to that obtained by RAL for the same cell.

The NMR signal from the ^{3}He cell was calibrated against the signal obtained from the H_2O sample. The comparison can be made since both measurements were performed using an identical NMR setup and similar sized cells. The maximum signal obtained in the frequency spectrum for ^{3}He was 321.5 ± 0.5 mV which from equation 4.9, yields a polarisation of 4.03 ± 0.1 %. This is by no means the maximum polarisation for this cell using this apparatus, since very little optimisation of the polariser had been performed at the time of this procedure.

The polarisation of the sealed ^{3}He cell was a useful process to determine whether the SEOP apparatus was functioning well and that the results obtained were comparable to similar polarisers in other institutions. But the real value of the polarisation measurement of ^{3}He in this apparatus, is that it enables the calibration of ^{129}Xe NMR which is difficult at low fields. For a meaningful calibration, two species should be investigated using identical NMR coils at the same operational frequency. The difference in the gyromagnetic ratios between ^{1}H and ^{129}Xe is almost a factor of 4 (see table 3.1), which means that the polarisation of ^{1}H must be done at a field, roughly one quarter the field that ^{129}Xe NMR is performed. Given the maximum field producible from our coils (4.00 mT), thermal polarisation of the water must take place at $\sim$1.10 mT. The NMR response expected from H_2O in such a low field is below the sensitivity of our NMR spectrometer. The resonance signal is not distinguishable from thermal noise.

The ^{3}He plays an important role in the calibration of ^{129}Xe polarisation with water, as its gyromagnetic ratio is more similar to that of ^{1}H. Since it is possible to calibrate ^{3}He with ^{1}H (as above), then ^{129}Xe can be calibrated with the ^{3}He resonance signal. This is true providing no loss in polarisation is suffered by the polarised ^{3}He in switching between resonance frequencies (B_0 fields). A short investigation was carried out into the losses suffered by polarised ^{3}He in the cell by field cycling from 4.007 mT to 1.455 mT and back again. The change in NMR signal from the ^{3}He before and after the field cycle was indistinguishable from the background noise. Polarised ^{3}He is therefore a suitable medium with which to calibrate ^{129}Xe polarisation indirectly with thermally polarised H_2O in our system.

5.3 ^{129}Xe SEOP

Within our SEOP apparatus, it is possible to individually control four major parameters that affect the experimental conditions and hence the degree of ^{129}Xe nuclear polarisation within the SEOP cell; cell temperature, laser power, cell pressure and gas flow rate. Of these, the most difficult to control is the temperature inside the cell as this does not necessarily correlate closely with the temperature of the oven but is affected by the Rb vapour density, laser power and gas flow rate as described within this section. All of the parameters are affected by one another and these interrelations will be discussed and summarised at the end of this chapter. The investigations presented in this section were performed on both static and flowing ^{129}Xe gas.

Our sealed ^{129}Xe cells were polarised in a similar way to the sealed ^{3}He cell. The polarisation in the ^{129}Xe cells (35 mm diameter by 50 mm length), was investigated initially using the dual coil NMR setup with separate Tx and Rx coils, but later and more usually, using the single surface coil and NMR duplexer. Investigations using the sealed ^{129}Xe cells facilitated partial optimisation of the SEOP apparatus before installation of our flowing ^{129}Xe cells.

Unfortunately, the narrowed laser source was not used to optically pump the sealed ^{129}Xe cells and so only low polarisations were ever achieved. The

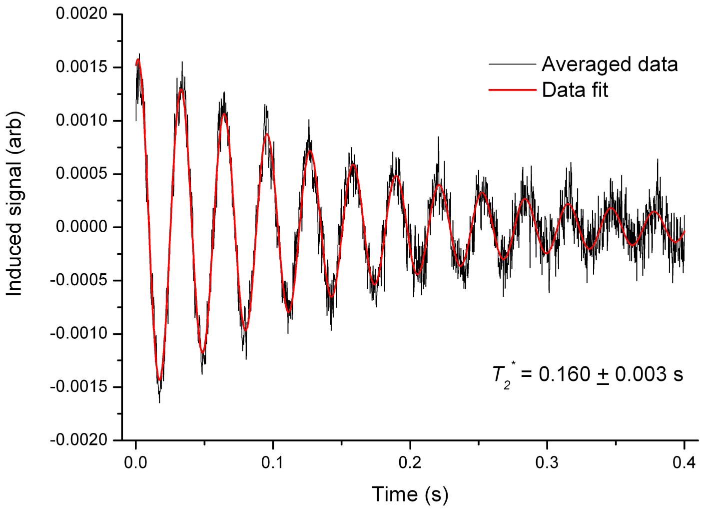

Figure 5.3: An average of 16 FIDs taken from Xe1. The fitted model is produced using equation 3.9.

T_1s of the cells were all short (under one minute) which was later attributed to wall relaxation (the cells are not coated). The FIDs from the cells could be used to assess the homogeneity of the field produced by the Helmholtz coils using equation 3.9 since the T_2 of gas in the laboratory field is long. The T_2^* of the excited gas was found to be 0.160 ± 0.003 s (see fig. 5.3) which relates to a ΔB_0 of 0.53 μT at a 4.00 mT operation field. This equates to an inhomogeneity of 1 part in 7500. The homogeneity of the field had been measured, using a high resolution Lakeshore gauss probe, to be almost 1 part in 7000. The higher homogeneity given by the gas relaxation technique is surprising since the direct measurement approach does not account well for off axis field variations (though these were measured). The gas dephasing measurement is considered the most accurate as it accounts for a bulk volume rather than a single linear profile.

The polarisation characteristics of ^{129}Xe were thoroughly investigated in both of our flow cells as a means to determine the precise conditions for optimal magnetisation production factor, MPF[1]. The cells were initially investigated in a static (no flow) mode before the installation of our flow system. Static cells have many similarities with sealed cells but allow investigations of varying gas pressures within the same environment. NMR diagnosis of these cells was performed exclusively using the single NMR surface coil and duplexer.

5.3.1 Laser Induced Rb Thermal Runaway

When using high powered laser sources to optically pump Rb vapour in a SE cell, it is particularly important to consider the effect of the energy absorbed by the Rb, most of which is lost as heat in the cell. If we consider that the amount of energy required to polarise all of the ^{129}Xe in one of our cells (ignoring the effects of relaxation) is of the order nanojoules, then 18 W (our coupled pump power) is available to heat the cell. Obviously not all of the light is absorbed, but with a spectrally narrowed pump source the percentage of absorbed light is far greater than for unnarrowed sources. Figure 5.4 shows the absorption of laser light by our cylindrical flow cell in the SEOP oven heated to 120 °C. Some 65% of the available light is absorbed which equates to ∼12 W of heating provided by the laser. Some of this heat will be dissipated through the walls of the cell into the temperature controlled oven, but in general, the cell can be expected to stabilise at several °C higher than the air in the oven. An unwanted ramification of this is that the density of Rb in the cell will change after applying the laser pump beam and so too will the absorption of light. In the extreme case, the Rb vapour will become optically thick and thermal runaway will occur. Ordinarily the increased Rb vapour pressure may prevent light propagation to parts of the cell furthest from the

---

[1] MPF is the product of gas polarisation, partial pressure and flow rate.

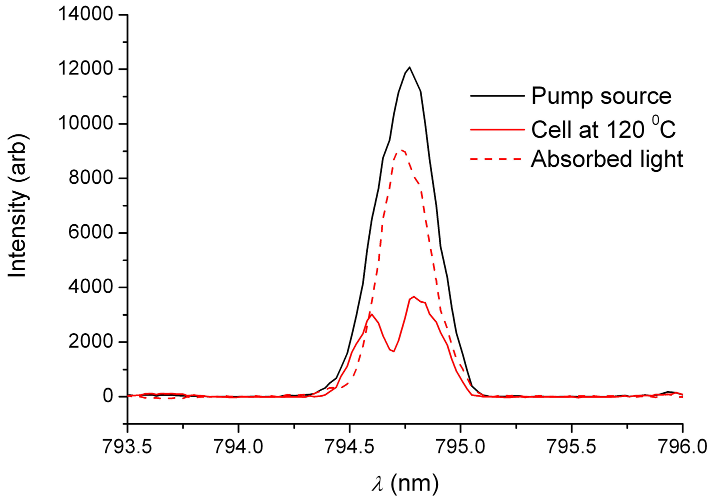

Figure 5.4: Comparison of the pump beam spectra through a cold cylindrical cell and at 120 °C. The absorption line is calculated by subtracting the transmission from the absorption spectra.

laser source which is detrimental to the ultimate polarisation.

The Rb vapour number density will initially be determined by the Killian [40] equation. With the application of a laser pump beam, energy absorbed and re-emitted by the Rb, will be absorbed by the N_2 buffer gas and the resultant thermal energy increase conducts to the other gases present in the cell. The cell temperature, T_{cell}, of the system progresses as shown in figure 5.5 after exposure to the pump beam. In our apparatus, the temperature of the oven, T_{oven}, is maintained by a flow of hot air. The temperature difference between the oven and the cell may be written,

$$\Delta T = T_{LP} - T_{loss} \tag{5.1}$$

where T_{LP} is the temperature increase induced by the absorbed laser power and T_{loss} is the temperature loss in the cell caused by conductive cooling from the cell walls and is therefore proportional to ΔT.

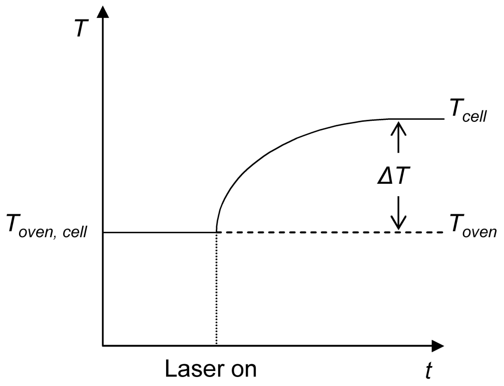

Figure 5.5: Simple representation of the cell and oven temperatures during a polarisation pump-up.

The result of laser induced Rb heating is that a massive discrepancy between measured and calculated gas polarisations can occur at higher temperature and/or laser powers if this thermal runaway affect is not accounted for. Results demonstrating the effects of thermal runaway are presented in sections 5.3.3 and 5.3.4.

5.3.2 Polarisation Pump-Up

At the onset of optical pumping of a SE cell containing Rb vapour, the Rb polarisation will increase rapidly. The level of polarisation reached by the Rb will depend on the vapour's number density, opacity, absorption line width and the laser's power and spectral profile. Steady state Rb polarisation is also determined by the rate of relaxation either through spin rotation or spin exchange (see section 2.2.3). The polarisation achieved in the noble gas is dependent on the Rb polarisation and rises from the moment the pump beam is activated. However, as the Rb is heated by the pump beam, its initial parameters will change and the polarisation of the noble gas will be duly affected. Below we present an example of the time dependence of ^{129}Xe polarisation within a SE cell.

The cylindrical flow cell was prepared at a static pressure of 2 bar and heated in the SEOP oven to 145 °C. Meanwhile the laser was energised with the beam path to the SEOP oven blocked. Once the oven temperature and pump laser had stabilised, the beam path was cleared and both the NMR signal and transmission spectra from the cell were monitored at 5 second intervals. The results are shown in figure 5.6. Currently we do not have the capability of directly measuring the density of Rb vapour, though some groups are able to do this via the employment of a Faraday rotation apparatus [90]. It is evident from the spectra in figure 5.6a, that the cell rapidly increases in temperature which generates a higher Rb vapour density and so the absorption of light increases. The heating of the cell does not stabilise within the 2 minute time frame of the experiment. As a consequence, the polarisation of ^{129}Xe in the cell (fig. 5.6b) which initially increases very rapidly (whilst the cell is less warm), suffers when the Rb vapour density prevents illumination of the whole cell. In such cases, it may therefore be necessary to modify the temperature of the oven from that described by equation 2.9 to account for the effects of laser induced thermal runaway.

Since the ^{129}Xe polarisation in a cell may take several minutes to stabilise, the NMR signals or polarisation measurements presented in the remainder of this chapter refer to steady state values unless otherwise indicated.

5.3.3 Temperature Dependence

It is necessary to optimise the temperature at which SE is performed as a number of factors relating to this parameter affect the ultimate polarisation within the cell. From equation 2.8 we know that the temperature of the cell determines the Rb vapour density [40] which, in turn, has an affect on light

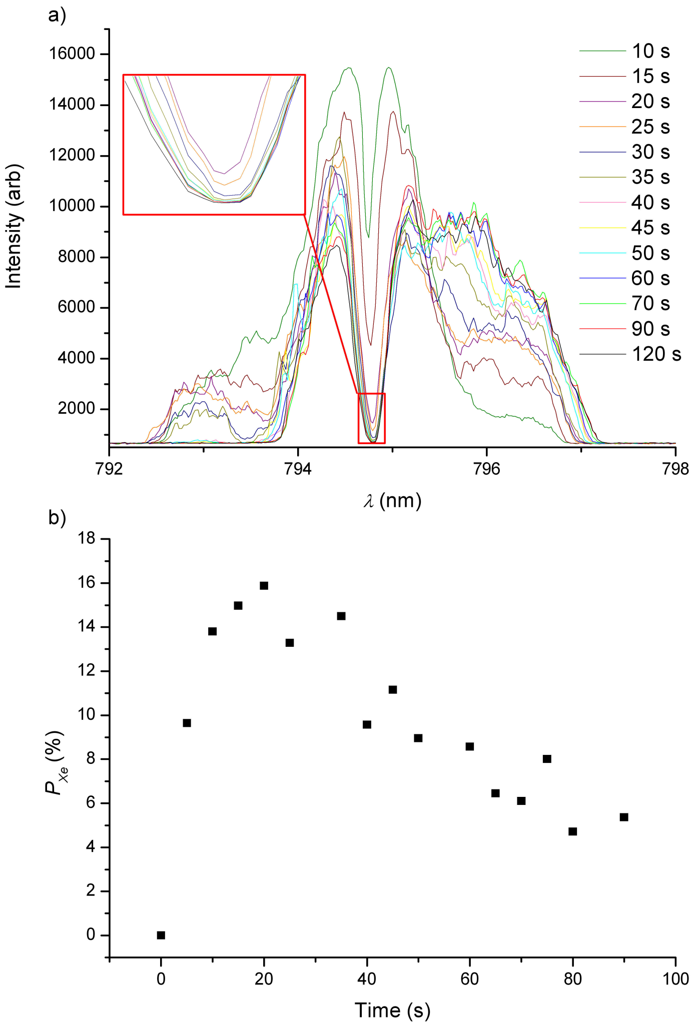

Figure 5.6: a) Absorption spectra and b) polarisation curve from a SE cell at 145 °C.

propagation if the vapour is too dense. Also, at higher temperatures, as the diffusion of the gas in the cell increases so does the rate of collisions between particles with other particles and walls which leads to an increased relaxation rate. Both phenomenona limit the ultimate polarisation achievable in a cell.

To investigate the effect of temperature on a ^{129}Xe cell and find the optimal operation temperature, the cylindrical flow cell was pumped by a narrowed pump beam with a constant 18 W coupled power. The pressure in the cell was maintained at 2.5 bar whilst temperature of the oven was gradually increased by 5 °C increments, with ample stabilisation time between temperature increments and NMR measurements. Both the NMR response from the cell and the spectra from transmitted laser light were recorded as a function of temperature with the results shown in figure 5.7. Optimum light absorption is observed at 135 °C before saturation occurs at higher temperatures. When the absorption saturates, the vapour is too dense to allow some of the pump beam to reach the rear of the cell. This reduces the overall polarisation of the gas which not only decreases the gas magnetisation achievable but acts as an extra source of relaxation to the polarised nuclei. Figure 5.7b shows a comparison of the recorded steady state NMR data from the polarised cell at a range of oven temperatures against a computational model for the optimum ^{129}Xe polarisation achievable (produced by Andrea Cherubini [91]). The model is generated in Matlab and takes into account the Rb vapour density, the photon absorption cross section, skew light and pump beam spatial inhomogeneities and Rb relaxation mechanisms to calculate the overall Rb polarisation. ^{129}Xe polarisation is then calculated using the theory outlined earlier in this thesis (section 2.2.4) which factors in the affects of relaxation mechanisms. However, the model does not account for the heating of the cell by the absorbed laser light or the distribution of Rb and ^{129}Xe polarisations within the cell, and so it is possible by comparison, to determine an apparent difference between the cell and oven temperature (ΔT) for a range of temperatures. It can be seen from figure 5.7 that the optimum oven operating temperature for this cell with these pressure and pump beam parameters is 120 °C.

The apparent ΔT between the cell and oven temperature for our static flow cell is plotted against absorbed laser power in figure 5.8. The plot has been divided into three absorbed power ranges. In range I where the density of Rb vapour is low, the laser power absorbed by the vapour has a nominal affect on the temperature of the cell with an average ΔT of 8.0 ± 1.1 °C. Section II corresponds to the region of the NMR-temperature curve immediately after the ^{129}Xe NMR signal from the cell has reached a maximum. Here, a dense Rb vapour causes enhanced heating which results in poor illumination of the cell and high relaxation rates. The polarisation of the cell is badly affected. In region III of the power curve, the laser light is blocked from reaching the rear of the cell and only part of the cell may be polarised. The measured data rapidly diverges from the computational model as an increasingly small volume of polarised Rb vapour is available to polarise the gas. With practically all of the light being absorbed in the front of the cell, the apparent ΔT for the whole cell reaches almost 300 °C. Though it was not investigated at this oven temperature, it is hypothesised that the polarisation of the gas at the front of the cell is much greater than at the rear of the cell when advanced thermal runaway occurs.

5.3.4 Laser Power

It was useful to investigate polarisation of the cell using a range of laser powers because of the effects of heating from the absorption of the pump

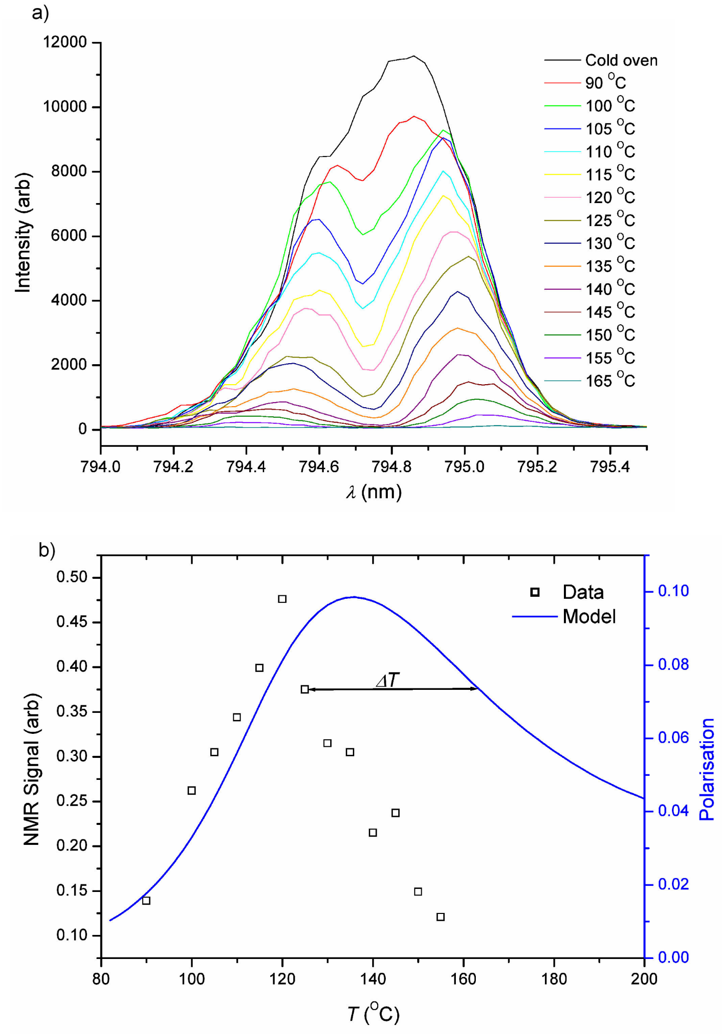

Figure 5.7: a) Laser light transmission spectra through the cylindrical flow cell for a range of oven operating temperatures. The light is absorbed by the Rb at 794.75 nm. b) Measured NMR signal with respect to temperature for our flow cell at 2.5 bar in comparison with a computer generated model using identical parameters. The discrepancy in the signal-temperature curve shape arises since the model does not account for laser heating of the Rb vapour. The temperatures on the x-axis refer to the oven temperature for the measured data and the cell temperature for the computational model.

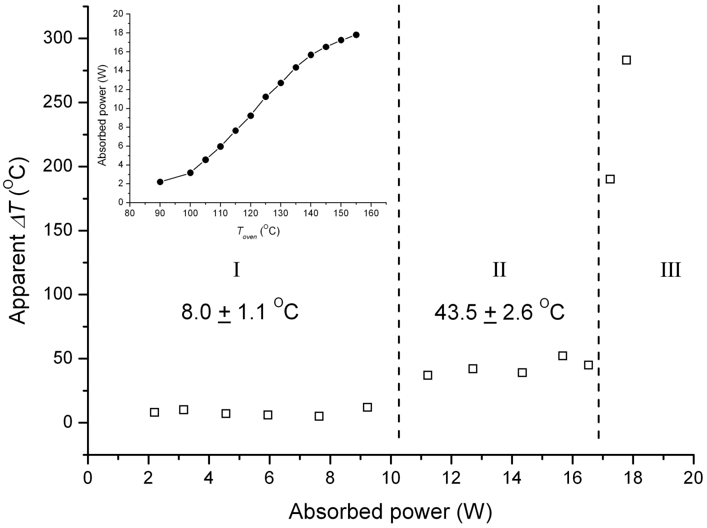

Figure 5.8: The apparent ΔT in our static flow cell a 2.5 bar with respect to power absorbed by the Rb vapour. The 3 sections of the plot are explained in the text. *Inset*, the variation of absorbed light with respect to the oven temperature.

beam, as observed in our NMR-temperature dependence studies. It was hypothesised that as the number of photons available to pump the Rb vapour increased, the probability that a Rb atom would become polarised would also increase. The effects on polarisation of the escalation in temperature within the cell noted in the previous section become relevant here also. However, since the polarisation of Rb is likely to increase with photon density, the polarisation of ^{129}Xe is also likely to increase which will partly combat the unwanted effects of the cell heating.

To investigate the effect of laser power on the polarisation of ^{129}Xe, our spherical flow cell was filled with a static 3.0 bar of enriched ^{129}Xe gas mixture (1 % enriched ^{129}Xe (86 %), 10 % N_2, balance ^{4}He) and heated to 145 °C in the SEOP oven. The unnarrowed laser diode was energised and allowed to stabilise with the beam path to the SE cell obstructed. Once cell temperature

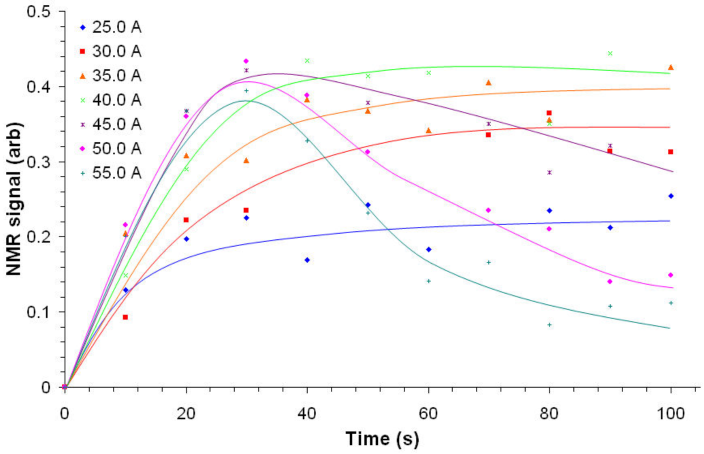

Figure 5.9: The evolution of NMR signal from our static spherical cell at 3.0 bar and heated to 145 °C. The cell is pumped with an unnarrowed laser diode over a broad range of diode drive currents. The solid lines are guides for the eye.

and laser emission were stable, the beam path obstruction was removed and the polarisation of the cell monitored over a couple of minutes using our NMR spectrometer. The results for a range of laser operation currents are shown in figure 5.9. From this plot it is immediately possible to identify that there is a significant dependence on the steady state polarisation of ^{129}Xe with laser power. As expected, there is also a time dependence in the polarisation of the gas as the system progresses to a steady state.

As the power of the laser device is increased, an initial increase in NMR signal from the spherical cell is also observed, but at higher powers, the increase in T_{cell} induced by the laser has a detrimental effect on the overall polarisation of the cell. As the laser power is increased, a denser more opaque Rb vapour is generated which in the first instance provides a faster spin exchange medium, but later can limit the volume of cell that is subject to the pump beam. The overall effect of this is a decrease in polarisation throughout the bulk of the gas. This laser induced thermal runaway determines the steady state polarisation achieved in the cell. For this investigation the optimum laser operation current was found to be 40.0 A.

Repeating this experiment with the cylindrical cell at 2.5 bar and pumping using the VHG narrowed laser yielded similar results with the optimum coupled pump power being measured at 18 W. The polarisation of the cell was monitored over a one hour period with little fluctuation in the steady state NMR response.

5.3.5 Pressure Dependence

It may be intuitive that the magnetisation of a cell will go up with pressure as more gas is available to polarise, but it has been found in this study that the increase in NMR signal from a polarised cell is greater than that predicted by simple pressure-polarisation ratios. That is to say, the polarisation of ^{129}Xe gas becomes more efficient at higher gas pressures.

Our spherical flow cell was heated to 116 °C inside the SEOP oven and the laser energised with a 60.0 A driving current and left to stabilise. The pressure within the cell was varied between 0.6 and 3.0 bar and the steady state NMR signal from the hyperpolarised gas recorded for each pressure. Surprisingly, the gas pressure within the cell did not affect either the FWHM, which remained constant at 0.13 ± 0.02 nm, or the intensity of the laser light absorption by the Rb vapour (see fig. 5.10) for the pressure range tested. High pressure cells have been used in the past specifically to pressure broaden the Rb vapour but over this pressure range there appears to be no evidence of this advantage. In accordance with the theory in section 2.2.2, the FWHM of the absorption spectrum should be directly proportional to pressure, P, but this study shows that in our system this is not the case. Using the model developed by Doebler and Kamke [92], the cross sectional area of a ^{87}Rb-

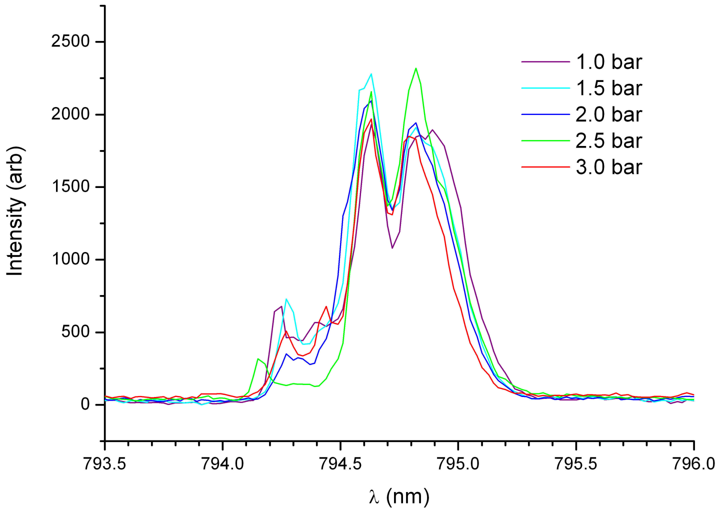

Figure 5.10: A pressure variation between 1 and 3 bar in the cylindrical cell has no observable affect on the Rb vapour density or absorption width.

^{129}Xe binary collision is 54.7 Å^2 at 389 K. From this cross sectional area we calculate that the Rb absorption FWHM at this temperature is 0.1 nm bar^{-1}, twice that reported by Shao [45]. Regardless of this, our Rb absorption line does not change noticeably with cell pressure.

The apparent disassociation of P and absorption width, $\Delta\nu$, indicates that Rb vapour pressure is not dependent on the gas pressure but only the cell temperature. It is well known that the Rb number density is dependent on temperature [40] and so therefore, is vapour pressure. But the partial pressure of Rb vapour does not increase with gas pressure and so the absorption linewidth does not increase with gas pressure either.

The intention of this investigation was to determine the effect of cell pressure on the magnetisation of the ^{129}Xe gas. Figure 5.11 shows the pressure normalised NMR signal (*i.e.* the signal divided by pressure) from the range of cell pressures investigated. Since no flow in the cell is present, the data represent the polarisation achieved in the ^{129}Xe gas. Optimal polarisation of the gas occurs at ∼2.5 bar. At pressures lower than 2.5 bar, a linear relationship between pressure and polarisation is observed. In this region, the efficiency of optical pumping is increased with the introduction of more gas into the cell, and subsequently the polarisation of the gas increases also. As there is no change in optical absorption from the Rb, this increase in efficiency occurs due to suppression of relaxation mechanisms. We have found the major relaxation mechanism in ^{129}Xe SE cells to be wall induced depolarisation. As the pressure inside a cell is increased, the relative amount of ^{129}Xe in contact with the wall reduces. Therefore, the overall rate of bulk relaxation due to these wall collisions also reduces with pressure.

As the pressure increases to 2.5 bar, the relative relaxation rate of the gas becomes slower until a minimum is reached at which the gas is polarised to its highest degree. As the pressure increases from this point, binary collisions start to dominate the relaxation of the gas and the efficiency of the polarisation falls away rapidly.

For our optical pumping system and gas mixture, the optimum pressure regime for maximised magnetisation was found to be 2.5 bar. This is the pressure at which hyperpolarised ^{129}Xe was produced for the applications described in the proceeding chapters of this thesis. The maximum polarisation achieved in the cylindrical flow cell at this pressure was calculated using our dual stage calibration described in section 5.2, to be 34 ± 3 %.

5.3.6 Gas Flow

The previous subsections describe factors concerning the ultimate polarisation of a cell containing ^{129}Xe gas. For studies of human lung spaces or macroscopic materials, large amounts of polarised gas are required to achieve sufficient NMR signal-to-noise and filling factor of the sample. Here we de-

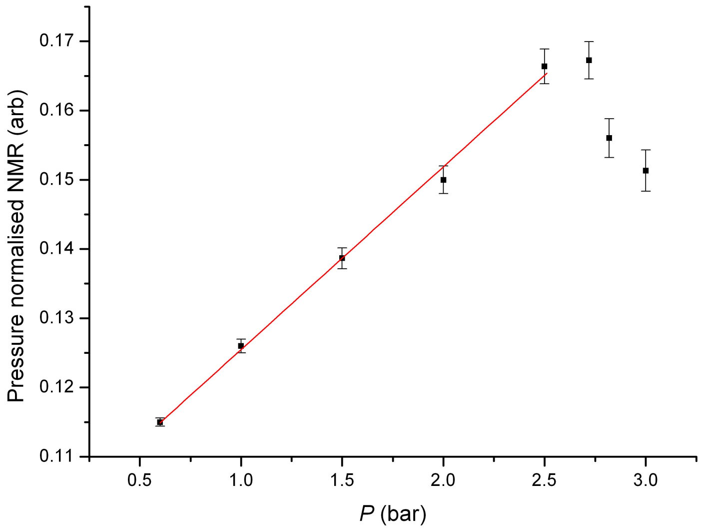

Figure 5.11: Pressure normalised NMR signal from our spherical flow cell over a range of static pressures. At pressures below 2.5 bar a linear increase in signal is observed.

scribe how the overall magnetisation production factor (MPF) is affected by gas flow rate.

For NMR experiments utilising hyperpolarised ^{129}Xe, it is necessary to extract the polarised gas from the cell. In this work, extraction was facilitated by the installation of a gas flow manifold presented in section 4.5. The flow system permits the continuous control of gas flow rate through the cell whilst also maintaining the desired operating pressure. In this section, the term 'flow rate' refers to the number cubic centimetres of gas, at standard temperature and pressure, passing through the flow controller each minute (sccm).

When using a flow system for SEOP, the major consideration is that the flow of new gas is likely to have an affect on the overall temperature of the gas within the cell. Since the Rb vapour density will therefore be affected, a significant affect on the overall polarisation of the ^{129}Xe gas should be expected.

To help rectify the temperature decrease, the operational temperature of the oven may be increased according to flow rate. Further implications on the polarisation of ^{129}Xe within a SEOP cell operating in flow mode are the effects of mixing of polarised and unpolarised gas and the cooling provided by the new gas on the rate of relaxation. It is not practical to prevent the mixing of freshly introduced gas and the polarised gas that has been in the cell some time. This will inevitably lower the overall magnetisation of the gas that is extracted at the exhaust of the cell. However, as the polarised gas is being removed from the cell to a cooler environment, the effect of relaxation in the cell is inconsequential to the slow relaxation of cool gas in the absence of Rb vapour.

In our spherical flow cell, the pressure was maintained at 2 bar and the gas flow through the system was increased from 0 to 70 sccm in 5 sccm increments. The steady state NMR response from the gas was recorded for each rate of flow. Figure 5.12 shows the magnetisation production factor for the 2.0 bar isobaric gas flow. The magnetisation of the gas continues to increase for the range of flow rates investigated. Because the magnetisation continues to increase in an almost linear fashion, it is implied that the rate of Rb polarisation is much faster than that of ^{129}Xe. This is already known, but what is shown here is that the rate of Rb polarisation, R_p, is so fast that the effect of SE transfers to ^{129}Xe on depolarising Rb are insignificant as the flow increases. We know from equation 2.5 that as the overall rate of relaxation of Rb, Γ_{Rb}, increases, which includes SE transfers, the Rb polarisation, P_{Rb}, decreases. This is evident toward the higher gas flow rates as the magnetisation of the gas diverges from its linear progression. At the point of divergence (∼50 sccm), the spin exchange rate, becomes greater than R_p and the laser light cannot sustain the high level of P_{Rb} produced at lower

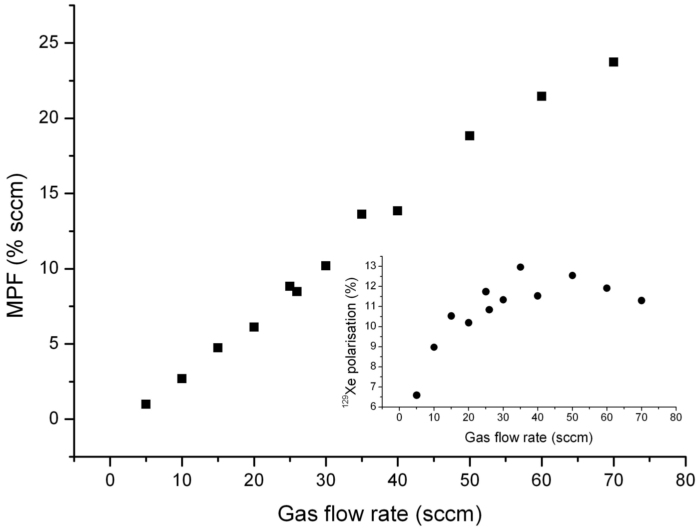

Figure 5.12: MPF in our flow cell as a function of gas flow rate. *Inset*, polarisation of ^{129}Xe as a function of gas flow rate.

flow rates. The increase in Γ_{SE} is a consequence of the increased apparent relaxation of polarised ^{129}Xe as the polarised gas exits the cell and new unpolarised gas enters. Another factor which affects the total number of polarised Rb atoms is the decrease in cell temperature brought about by the influx of much cooler gas which reduces the density of Rb vapour, particularly at the rear of the cell (near the gas inlet).

The maximum flow available in the cylindrical cell was found to be 176 sccm at 2.5 bar which corresponds to a cell volume gas exchange every 136 s. This does not mean that the gas is completely exchanged in this time: convection currents from the flow of gas add to those present within a static cell [93] and the true exchange of gas becomes difficult to model. The high flow rate possible in the cylindrical cell produced MPFs which were not optimised for the system but had the advantage of reducing the transient time of hyperpolarised gas to the high field NMR spectrometer in the adjacent laboratory. Using the flow system to force the gas through to the high field NMR spectrometer, a flow rate of 176 sccm was maintained for long periods of time (>10 min). A small tuned RF solenoid was positioned around a section of 4 mm ID PFA tubing on the return of the gas into the Helmholtz holding field in the SEOP laboratory. This coil was employed to monitor the NMR of the gas returning from the high field spectrometer. Despite readily obtaining an NMR signal from the hyperpolarised ^{129}Xe returning to the SEOP laboratory, no NMR detection of the gas was ever made in the high field spectrometer.

For batch production of hyperpolarised ^{129}Xe collected in Tedlar gas bags, the continuous flow production of gas was superseded by a pseudo batch-flow production method which yields higher MPFs. In this method, the cell is polarised at 2.5 bar in a static mode for 1 minute whilst monitoring of the NMR from the cell is performed at 30 second intervals. Once polarisation in the cell exceeds 10 % (∼0.3 mv NMR response), the cell is opened to the evacuated Tedlar bag and the pressure allowed to equalise. This deposits ∼200 ml of hyperpolarised gas mixture into the bag. The cell is isolated from the bag and repressurised to 2.5 bar. The gas is left to polarise for a further minute before the bag filling procedure is repeated. The bag is full after five cycles and the MPF can exceed 80 % sccm using this method. The installation and pumping out time for a new bag is 5 minutes, so the long term MPF of the system is in the region of 40 % sccm.

The peristaltic pump driven gas recirculation system was not extensively tested as severe contamination of the Rb in the cell resulted from out gassing of the peristaltic tubing.

5.4 Summary of ^{129}Xe SE Polarisation

In our spin exchange optical polariser, the parameters which determine the ultimate polarisation and magnetisation of ^{129}Xe have been investigated. Cell temperature, laser power, gas pressure and gas flow rate all have an affect on the productivity of the polariser. These parameters have been characterised and optimised for our system and significant interdependencies between these parameters have been observed.

The Rb vapour density within our SEOP cell has been shown to be dependent on the temperature of gas, which does not necessarily correlate closely with the SEOP oven temperature. Because of the power coupled from the pump laser into the Rb vapour, an increase in thermal energy conducts to the buffer gases and Xe which increases the temperature of the cell and therefore the Rb vapour density. It has been shown that the increased vapour density will absorb a broader, more intense laser light spectrum and as a result, thermal runaway of the SE cell may ensue.

The initial temperature of the cell, *i.e.* the oven temperature, and the laser spectral intensity define the amount of Rb heating experienced within the cell. If the initial temperature of the cell is increased, enhanced collisional relaxation prevents high polarisations of gas from being produced. It is therefore desirable to operate the SEOP oven at as low temperature as possible whilst still maintaining a suitable Rb density to act as an effective SE medium. If the laser power is increased, the escalation of Rb vapour density will occur predominantly at the front of the cell. This can lead to 'dark' areas at the rear of the cell which reduces the overall magnetisation attainable in the gas.

The optimum operation temperature for our oven was found to be 120 °C when using our sealed ^{129}Xe cells. A laser current of 40.0 A (18 W coupled power) provided an asymptotic approach to a steady state polarisation in the cell with no long term deterioration of NMR signal. These parameters were successfully implemented for all ^{129}Xe SEOP cells.

Varying the gas pressure in one of our flow cells revealed that whilst the magnetisation of the sample could be increased, collisional relaxation was also enhanced. For our gas composition the optimum pressure to achieve maximum magnetisation of the gas was found to be 2.5 bar.

Observing the width of the absorption spectra of laser light by our Rb vapour, as a function of gas pressure inside the cell, revealed that no pressure broadening occurred over the investigated pressure regime (1 to 3 bar). This is not consistent with the use of high pressure cells for broad optical pumping lines although most of the evidence for the pressure broadening of absorption linewidths is from ^{3}He SEOP experiments. We find that careful temperature control would prove more successful.

The rate of gas flow through a polarisation cell was found to significantly affect the magnetisation production factor of the ^{129}Xe gas. The influx of gas into a polarisation cell reduces the overall temperature of the gas and Rb vapour. It is true therefore, that gas flow rate can have a significant affect on the Rb vapour density and the temperature of the cell and hence the overall polarisation of the gas within. Cooling of the gas has the positive effect of reducing relaxation mechanisms due to atomic motion.

For the gas flow range investigated, the MPF of the system continued to increase. The reduction in polarisation caused by high flow rates is more than compensated for by the larger volume of hyperpolarised gas; a consequence of the very fast polarisation rate of ^{129}Xe.

In a static cell, the maximum polarisation of ^{129}Xe gas measured in our system was 34 ± 3 %. The maximum MPF for our system using a continuous flow protocol was 23.7 % sccm and in our pseudo batch-flow production method, the MPF exceeds 80 % sccm if relaxation of the collected gas is neglected. For larger or more concentrated samples of hyperpolarised ^{129}Xe, it will be necessary to improve the Xe freeze out technique described in chapter 4.

We have produced and refined a spin exchange optical polariser capable of producing large enough quantities and magnetisations of hyperpolarised ^{129}Xe to perform medical and materials NMR studies. The methodologies and results of some preliminary studies in these fields are presented in the following chapters.

Chapter 6

Imaging of Hyperpolarised ^{129}Xe for Medical Studies

The high polarisation achievable, with the readiness for absorption into a vast number of biological materials and corresponding chemical shifts, makes ^{129}Xe NMR ideal for a wide variety of medical applications. In recent years, ^{129}Xe has found applications in medicine ranging from studies on lung airspaces and gas uptake [94] to blood dissolved ^{129}Xe NMR in the human brain [95]. This chapter summarises work carried out in this thesis on the feasibility of medical studies using the NMR and MRI facilities available at Nottingham and the hyperpolarised ^{129}Xe gas produced here.

6.1 Experimental

This section describes the experimental setup and procedures carried out during studies of the hyperpolarised ^{129}Xe gas as a potential medium for medical investigations. The polarisation of the ^{129}Xe gas used in the following experiments has been described in the previous chapter as well as the polarised gas collection procedure using the pseudo batch-flow mode.

6.1.1 Gas Samples

Two gas sample containers were used to transport/contain the hyperpolarised ^{129}Xe gas mixture for gas NMR and imaging studies. The first, used for preliminary studies of the gas in a whole body MR scanner, was an OTS coated spherical Pyrex cell (fig 6.1a) of 44 mm diameter (33.5 ml volume) with two ports situated at opposing sides and high vacuum PTFE valves. The cell was connected directly onto the exhaust port of the cylindrical SEOP cell (whilst keeping it well within the B_0 field) using a ball and cup joint, before being evacuated to $\sim 2 \times 10^{-1}$ mbar. The SEOP cell (2.5 bar) was polarised at 110°C until a plateau in polarisation was achieved (generally $\sim$16% polarisation in the ^{129}Xe gas). The two cells were then opened up to one another with the Rb cold trap active on the outlet of the SEOP cell. A redistribution time of a few seconds was allowed for the gas before both the cells were resealed (at 1.96±0.08 bar) and the cylindrical cell disconnected from the system.

The second gas sample container was a one litre Tedlar gas sample bag (fig 6.1b, SKC Gulf Coast Inc., USA). These are chemically inert, non-permeable bags with a single filling valve. The bag was connected to the SEOP cell via a PFA tubing section and a ‘T’ piece which allowed both the evacuation and filling of the bag through the valve (fig 6.2). The flow rate of gas into the bag could be controlled effectively using an adjustable restriction in a short section of narrow bore marprene tubing. The bag was filled using a pseudo batch-flow regime as previously described which enabled a full bag sample to be generated in under 5 minutes. Providing the volume of gas in the bag did not exceed a litre, the pressure of the sample in the bag remained

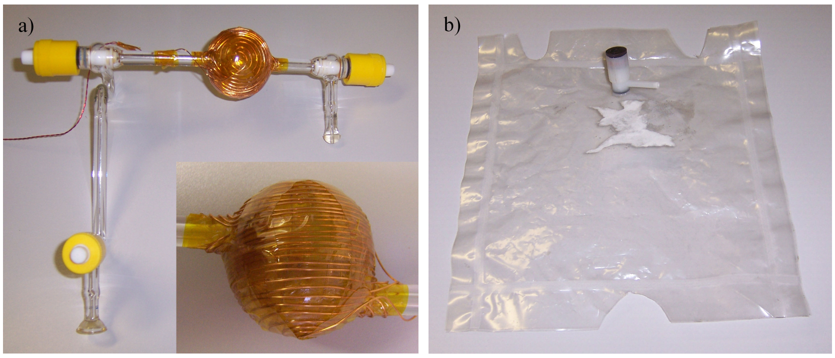

Figure 6.1: a) The 33.5 ml spherical Pyrex cell used as a gas sample holder in the MRI scanner. Inset is a close up of the 'delta z' coil described in section 6.1.3 and b) a 1 litre Tedlar gas bag used in human lung experiments. A magnetic label and rivet have been removed.

exactly 1 bar. The bag could then be sealed via its valve and disconnected from the filling station before transportation to the MRI scanner.

Once prepared, the gas samples were transported 30 m to the MRI scanner in only the Earth's magnetic field. Since the energy of a polarised nuclei is dependent on the strength of its holding field, the rate of relaxation due to spin-spin coupling is also dependent on this field strength and hence, so is the lifetime of the polarised gas. The best way to prevent relaxation of the gas during transportation in this manner is to limit the length of time the sample is exposed to low or varying field strengths. Therefore the sample was transported as quickly as possible between the polariser and scanner before being introduced into the centre of the magnet (through its rapidly varying field) in as short a time as possible.

6.1.2 MRI Scanner

The scanner used for all experiments was a whole body 0.146 T ceramic ferrite permanent magnet (IGC, USA). The magnet has an elliptical bore (0.55 m × 0.68 m) with a length of 1.95 m and has its field in the transverse

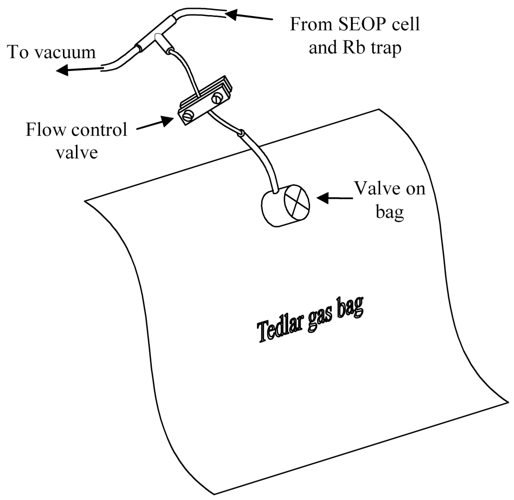

Figure 6.2: Diagram of the Tedlar bag filling setup. There is a pressure difference of 1.5 bar across the flow control valve which restricts the gas flow through a piece of 1.6 mm bore peristaltic pump marprene tubing.

direction. The region of practical field homogeneity stretches 200 mm either side of the magnet's isocentre with the 5 G line at a distance 2.35 m from this point. For the purpose of MR imaging, the scanner is capable of producing magnetic gradients in all three Cartesian planes. The maximum gradients achievable inside the bore are 18.7, 17.8 and 14.4 mT in the x, y (vertical) and z (along bore) axes respectively. A more detailed description of this system is documented in B. Waters' thesis [66].

This magnet is of a much lower field than normally found for MRI scanning (typically of the order of a few tesla), but since the polarisation of the hyperpolarised ^{129}Xe is not dependent on field strength, the scanner is ideal for this kind of experiment. Furthermore, at low field and therefore low resonances, it is easier to build and tune RF coils and to generate signals at these lower frequencies. For imaging, the use of lower amplitude field gradients is permissible whilst the likelihood of susceptibility artefacts is substantially reduced. It is also possible to use sequences such as RARE (see section 6.1.5).

6.1.3 RF Coils

Alhough the MR scanner used during these investigations has a built-in RF Tx coil and associated commercially produced Rx coils, these are all designed and tuned to operate at either ^{1}H or ^{3}He Larmor frequencies for this field. Since the Larmor frequency of ^{129}Xe is much lower than that of ^{1}H and ^{3}He (table 3.1), there was a necessity to build new RF coils for NMR experiments of this species.

RF Transmit Coils

Two separate Tx coils were used for these investigations, each designed to produce a homogeneous RF B_1 field over different sample volumes. The first, built by J. O'Neil, consisted of a Helmholtz pair of 10 turns of 2 mm copper wire per coil with radii 160 mm and a separation of 85mm (fig 6.3a). The coil set was capacitance tuned in series to 1.713 MHz and impedance matched to 50 Ω with a Q of 30. The coil could be located centrally in the magnet bore by removing a cushioned section from the patient bed and locating the tongue on the bottom of the coils into the grove on the bed. The scanner has the capability of centralising the coil set along the z-axis using a laser positioning device. The small size of this coil set made it ideal for measurement of small samples, as low power RF pulses could be used to achieve large transverse tip angles of the nuclei in a sample.

The other Tx coil used was designed to accommodate a human chest and consisted of a 10 turns of 2 mm copper wire around an elliptical solenoid of circumference 1.13 m (fig 6.3b). The turn spacing is at 38.9 mm and the tuning was done as for the Helmholtz Tx coil, with a Q of 17. Unfortunately, it was not possible to locate this Tx coil directly in the centre of the magnet bore as the patient bed restricted the vertical position of the coil. However,

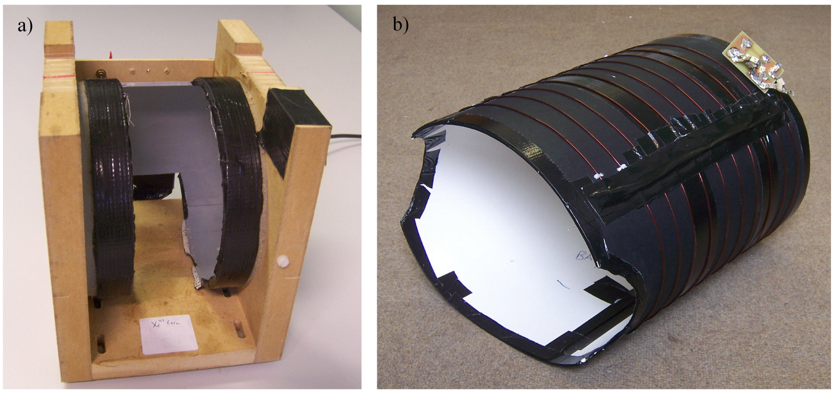

Figure 6.3: a) Helmholtz Tx coils used in conjunction with the 'delta z' and solenoid Rx coils. And b) The body Tx coil.

the region of field used for imaging in the scanner was large enough to overcome this problem, particularly when considering the location of a volunteer was nearly the same with or without the Tx coil.

The NMR pulses for the coils were generated by the scanner console on instruction from the user defined control software. This signal was then processed through a Tomco BT04000-DL power amplifier (Tomco Electronics Pty Ltd., Australia) rated at 4 kW with a bandwidth of 0.5 to 8 MHz. A more detailed description of this amplifier is given in ref [66].

RF Receive Coils

A variety of RF Rx coils were designed and built for the experiments carried out within the scope of this thesis, though some designs proved more successful, in terms of sensitivity, than others. These coils are described in this section.

In the case of the spherical Pyrex sample cell, since it is a fixed size rigid spherical body, a sine theta coil was the most appropriate selection. A sine theta coil may be used over a volume that has a circular cross section and consists of a number of current loops each separated by a constant angle ϕ. The current, I, in each loop is then varied such that $I = I_{max}\sin(\theta)$ where $\theta = n\phi - \phi/2$ for the n^{th} turn and where $\phi = 180/n_{max}(n - 1/2)$ (fig 6.4a). To vary the current in each winding however, generates a problem concerning multiple, coupled resonant circuits and the use of capacitors to produce a phase shift between coil loops or multiple amplifiers. It was hypothesised therefore, that rather than varying the current, if one were to vary the separation angle of the individual turns, this would produce a similar effect. Hence a model was developed in which ϕ no longer remained constant, but instead the separation of the current loops in the z-plane is constant and the current does not vary between turns (fig 6.4b). This 'delta z' coil is such that $\Delta z = 2r/n_{max}$ and $z = r((n_{max}+1)/n_{max} - 2n/n_{max})$ where r is the radius of the cross section and so the field produced by each turn is dependent only on the radius, R, of that loop. The homogeneity of the 'delta z' coil was found to be lower than that for the sine theta design in a comparison of mathematical models, though the central field produced was of a larger magnitude. The comparison of models of the two coil designs for a spherical body are presented in Appendix B.

The 'delta z' coil design was used on the spherical Pyrex cell and constructed from 29 turns of 0.5 mm copper wire over the surface of the 44 mm diameter body (fig 6.1). The coil was tuned in series to 1.713 MHz and impedance matched to 50 Ω with a Q of 42. The sample was filled at the SEOP rig before being carried to the scanner, where it was inserted into the centre of the Helmholtz Tx coil inside the scanner for measurements on the gas.

Another Rx coil designed to be used with the Helmholtz Tx coils was a 100 mm by 70 mm diameter solenoid consisting of 33 turns of 1 mm copper

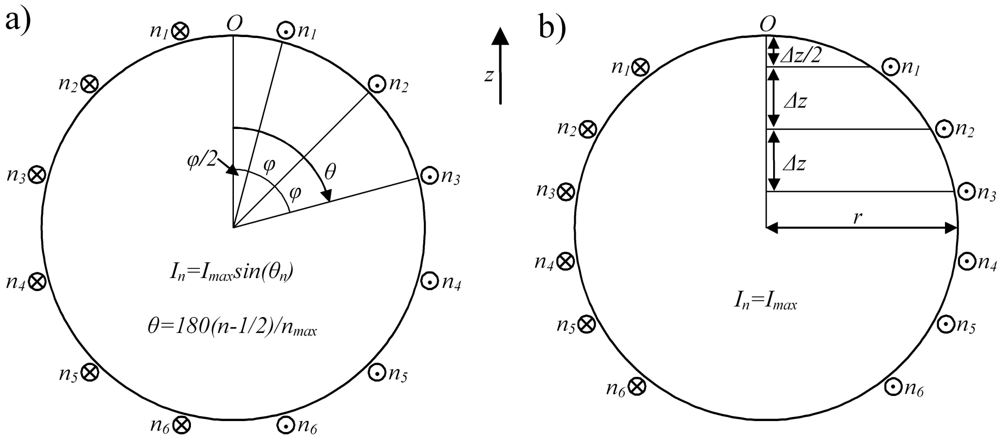

Figure 6.4: Two coil designs for bodies of circular cross section. The sine theta coil (a) has varying current dependent on the position of each turn, whilst the much simpler 'delta z' coil (b) has a constant current in all loops whist varying the angle between adjacent turns.

wire (fig. 6.5a). Again, tuned and matched to the appropriate frequency, the coil has a Q of 58. The internal size of the solenoid is such that a partially filled gas bag may be inserted inside, or inflated whilst already inside the coil. The solenoid fitted vertically into the horizontally orientated Tx coils and so the filled bag and coil could both be introduced into the scanner together. This solenoid was also the main Rx coil used for the materials studies described later in this thesis.

For studies using the body Tx coil, two Rx coils were built and used, one a spiral surface coil (fig 6.5b) and the other a human chest sized spiral saddle coil. To avoid detuning, the coils were tuned and matched whilst inside the scanner and a volunteer loaded in the experimental position. The surface coil consisted of 10 turns of 2 mm copper wire. The radii of the turns (in mm) are: 32.5, 46.0, 56.5, 65.0, 72.5, 79.5, 86.0, 92.0, 97.5 and 103.0. Each turn spiralled out to the next radius in the last quarter. The aim of the design was to achieve as much signal pick-up as possible over the volume associated with

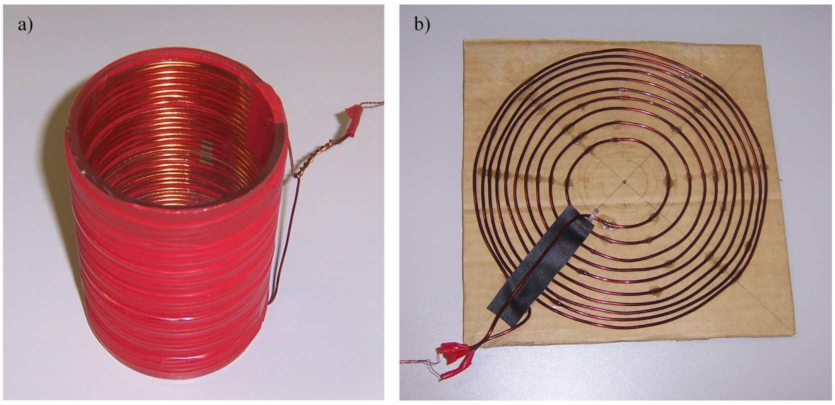

Figure 6.5: a) Small solenoid Rx coil and b) spiral surface Rx coil.

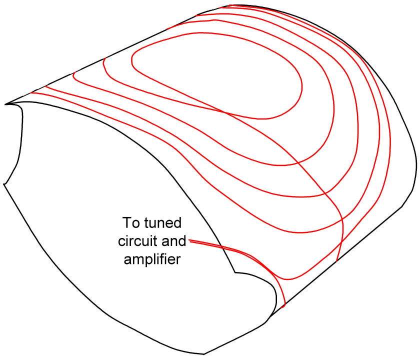

Figure 6.6: Diagram of the body Rx coil.

one of the gas sample bags described earlier. In section 4.6.1 it is shown how a current loop is sensitive to signal with respect to radial and axial position and this prompted the use of the spiralling current loops. The coil was tuned to 1.713 MHz with a Q of 53 and impedance matched appropriately.

The body Rx coil (fig. 6.6) consists of two sets of five turns wound on opposing sides of an elliptical mandrel. Each coil turn traces a path about two foci, with radii ranging from 6 to 14 cm and origin separations 4 to 10 cm respectively. The coil former is 30 cm in length and 1.0 m in circumference. It is tuned and matched appropriately with a Q of 53.

The pre-amp used in conjunction with the Rx coils for all experiments in the MRI scanner was a Miteq (USA) AU-1442-BNC bipolar amplifier with bandwidth 0.01 to 200 MHz and a gain of 35 dB.

6.1.4 Experimental Setup and Gas Delivery

The majority of experimental investigations involving hyperpolarised ^{129}Xe were carried out inside the bore of the 0.15 T magnet previously described. For experiments concerning only the sample of gas in its container in which it was collected, the experimental setup procedure was straight-forward involving the insertion of the sample into the pre-positioned RF coils inside the scanner. Immediate retirement to the adjacent control room allowed a number of desired measurements to be made with no further human intervention.

For experimental work requiring a volunteer to breathe in the gas sample or to act as a control, a greater level of organisation was required for optimisation of procedure and results. The volunteer was pre-loaded into the scanner already donning the body Tx and appropriate Rx coil. The gas sample was then prepared in the Tedlar gas bag, whilst the volunteer and scanner operator waited. When ready, the sample was transported to the scanner room and inserted into the bore of the magnet. Because the volunteer occupied most of the room inside the bore, the bag could not be kept in the centre of the field but instead was held as close to the chest of the volunteer as the situation would allow, thus minimising relaxation of the ^{129}Xe due to field inhomogeneity. The RF cage to the scanner room was then closed with the hyperpolarised gas producer/transporter still on the inside. The signal was then given for the volunteer to breathe in the gas sample, which took between 5 and 10 s. After breathing in the sample, the patient also took a small sip of air to ensure as much of the hyperpolarised gas mixture was

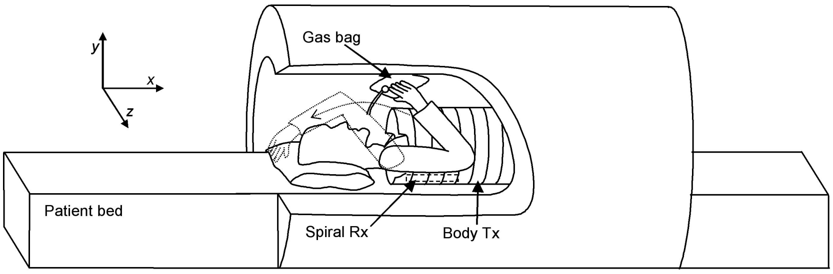

Figure 6.7: Cut-away diagram of a volunteer situated in the 0.15 T body scanner. The Rx coil is positioned inside the Tx coil close to the volunteer's back where the lungs are closest to the skin.

present inside the lungs as possible. At this time, the volunteer extends their arms above their head to a) ensure their arms do not de-tune or deform the RF coils, and b) to show that they are ready to be scanned (obviously they cannot speak). The gas producer, in turn, signals to the control operator to begin measurements/scanning. Once completed, the signal is given for the volunteer to exhale and then they are removed from the bore of the scanner.

6.1.5 MR Pulse Sequences

Before any meaningful measurements can be made within the scanner, a tip angle calibration needs to be performed to determine the RF energy/tip angle relationship of the nuclei. The tipping angle of an RF pulse is a function of both its length and its height (power). Inside the scanner, the calibration was performed by increasing the pulse power from a low value (typically 1% on the scanner console) in small steps, to a value close to the 90° excitation for the sample. The pulses were taken in pairs with a short time interval, and the percentage destruction calculated for the higher power excitations. From these, a 90° pulse power could be deduced which ensured that the correct excitation could be applied during the imaging sequence to achieve the desired spin rotation of the sample nuclei.

For measurements of T_1, a series of small tipping angle RF pulses were taken over a measured time period such that the spin-lattice decay rate of the polarisation could be measured as described in section 3.4. For the purpose of imaging, a tip angle calibration was required of the sample using the same shaped pulse as used during the intended imaging sequence. The sequence used for imaging was Rapid Acquisition with Relaxation Enhancement (RARE) which uses a sinc ($\sin(x)/x$) shaped pulse.

A RARE sequence is a multi spin echo sequence that uses different phase encoding for each echo which allows the accumulation of an entire image within the T_2 of the sample, which is necessary for non-renewable polarisation, as is the case with hyperpolarised gases. A single 90° pulse is applied to the sample with a slice selection gradient (z-axis) active which defines the region of sample that is to be investigated. Whilst the nuclei in the sample dephase from one another, a phase encoding gradient (x-axis) is applied for a short while before being switched off. The phase encoding allows the selection of a single line of k-space to be sampled during signal acquisition. At a time $te/2$ after the 90° pulse, a 180° pulse is applied to the sample to invert the spins of the nuclei in the x-y plane. At a further time $te/2$ after the 180° pulse, a spin echo occurs, during which time a frequency encoding gradient (y-axis) is applied whilst data acquisition occurs. Once the echo has decayed and acquisition ceased, the phase encoding gradient is reapplied but this time, centres on a new line of k-space. Now gradients are required to rephase the nuclei in the excited region ready for the next RF pulse and echo. A further $te/2$ later and another 180° RF pulse is applied, and an echo signal is acquired as before. This process is repeated n times, for the whole of the sample size (64 lines for these experiments) with the entire sequence taking of the order of a second. The sequence operates in a centre out fashion

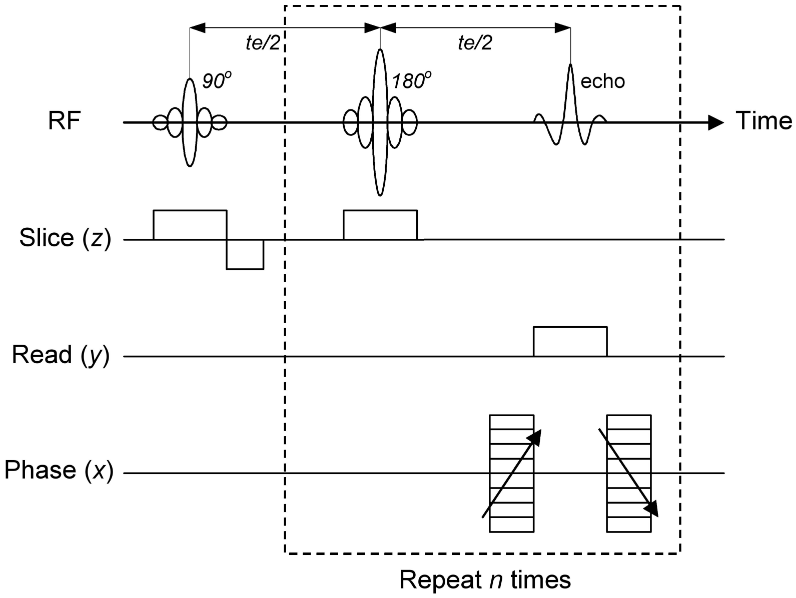

Figure 6.8: 2D RARE sequence diagram.

through k-space.

The general procedure for the measurements of diffusion coefficients made in this work are outlined in section 3.6.2. Two measurements were made of the diffusion coefficient of ^{129}Xe gas in the SE gas mixture; one in the spherical cell (∼2 bar) and one in the Tedlar gas bag (1 bar). The sample production procedures were identical to those used for imaging described above. Both measurements were performed with identical parameters so that a direct comparison could be made. In both cases the diffusion gradient used was 0.03991 mT cm^{-1} with δ and Δ at 1.05×10^{-3} and 14.0×10^{-3} ms respectively. The diffusion coefficient measurement procedure has previously been calibrated for ^{3}He using this system and reported by Waters [66].

6.2 Results

A number of results concerning the feasibility of human lung studies were obtained and are presented in this section along with data defining the lifetime and behaviour of hyperpolarised ^{129}Xe gas both inside the whole body scanner and inside the spin exchange magnetic environment.

6.2.1 T_1 of Polarised Samples

A sample of polarised gas was collected inside the spherical Pyrex cell and taken to the MRI scanner where, it was placed inside the Helmholtz Tx coil. A 13° pulse (2.6% destruction) was taken at recorded intervals and the data plotted in accordance with equ 3.16 (fig 6.9). For comparison, the cell was refreshed with newly polarised gas and placed on top of the SEOP oven with, the surface NMR coil normally used within the SEOP cell, placed underneath. This ensured the sample region of the cell was as close to the region of maximum B_0 homogeneity as possible. A series of 32.7° pulses (over tiny sample volume) were taken at 1 minute intervals and this data plotted and analysed (fig 6.9(inset)). The two values for T_1 of the hyperpolarised ^{129}Xe inside the different environments were 117.1 ± 5 min and 15.1 ± 1 min for the scanner and polariser respectively. This is a significant difference for similar gas samples. The only experimental differences to be considered are the magnetic field strength and homogeneity which are different for the two environments.

Similarly, the spin lattice lifetime was investigated for polarised gas in the sample bag inside both the scanner and SE magnetic field. The bag, at roughly 30% of its capacity, was investigated inside the scanner using the solenoid Rx coil whereas a full litre of gas was investigated on top of the SEOP

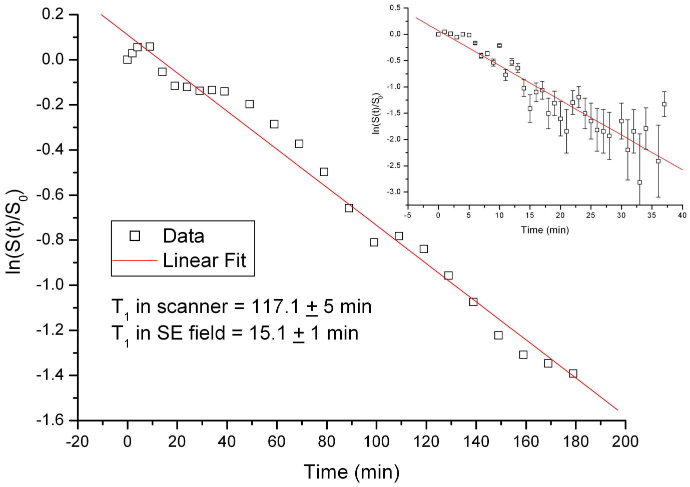

Figure 6.9: A plot of $ln\frac{S(t)}{S_0}$ against t (gradient $= -\frac{1}{T_1}$) for the polarisation of ^{129}Xe inside the spherical Pyrex cell in the MRI scanner reveals a T_1 of 117.1 ± 5 min. *Inset*, a similar plot reveals a T_1 of 15.1 ± 1 min inside the SEOP environment for the same cell.

oven using the NMR spectrometer single surface coil. The results are shown in figure 6.10 with T_1s of the polarised ^{129}Xe calculated to be 139.9 ± 1.6 and 66 ± 21 min inside the scanner and SE environment respectively.

A sample of polarised gas was generated in the gas bag and this was administered to a volunteer inside the body scanner within the body Tx and with the spiral Rx coil positioned under their back for optimum signal detection. The volunteer held their breath whilst a series of 41° pulses were taken. The need for such a large pulse is due to a couple of factors which lead to decreased signal from the Rx coil; increased distance from coil to gas and detuning of the coil by the presence of a body. Because of the large tip angle needed, the correction factor applied to each FFT had a progressively detrimental affect on the SNR of the spectra. Despite this, a measure of the gas relaxation in the lungs was made using four points (number of pulses taken during breath hold), to give a T_1 of 27.6 ± 4.4 s (fig. 6.11). This is a

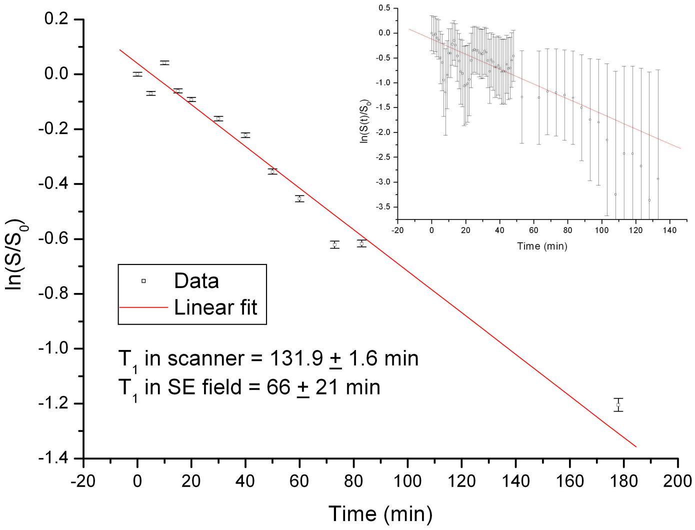

Figure 6.10: A plot of $ln\frac{S(t)}{S_0}$ against t (gradient $= -\frac{1}{T_1}$) for the polarisation of ^{129}Xe held in the gas sample bag inside the MRI scanner and, *inset*, a 5-point average of the data collected for the bag within the SEOP field. The large errors in the data of the inset graph, arise from the low signal to noise obtained in the FFT spectra, a symptom of the small coil sensitivity volume.

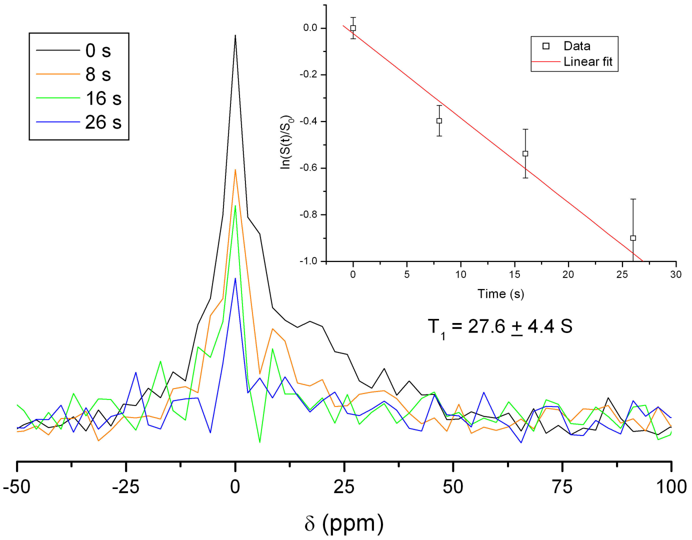

Figure 6.11: The FFT signal from hyperpolarised ^{129}Xe in a human lung over a single breath hold and *inset*, the decay of signal with respect to time. Note the shoulder on the right of the spectrum.

significantly lower lifetime of the gas in comparison to any other measurement made. It is suspected that this is due to oxygen in the lungs where the effect on T_1 has been well documented for ^{3}He [96].

To identify the source of this greatly enhanced relaxation, the T_1 of the gas in the bag was measured which had been contaminated with a small portion of air expelled into the bag from the author's lungs. This reduced the T_1 of the hyperpolarised gas to 206 s from a previous uncontaminated lifetime of 132 minutes. Obviously, the amount of air introduced into the sample bag was uncalibrated but it is reasonable to suggest that the relaxation of the gas in the lung is dominated by the level of contact with air to which it is subjected.

A further finding to note is the presence of a shoulder on the resonance peak of the ^{129}Xe inside the lung. This has not been reported in literature, but may be another resonance peak caused by the existence of ^{129}Xe absorbed

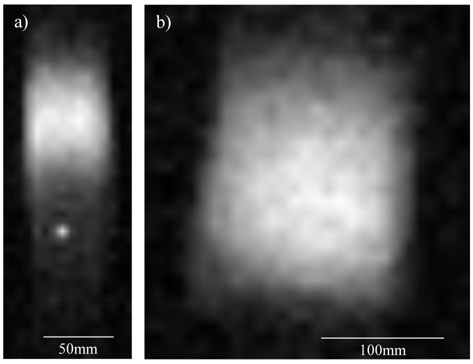

Figure 6.12: Hyperpolarised ^{129}Xe gas images. a) gas bag in solenoid Rx yields SNR of 55. The bright spot in the lower part of the image is a zero offset artefact. b) gas bag in lung imaging setup with SNR of 19.

onto the tissue of the lung.

6.2.2 Imaging ^{129}Xe

With the ability to produce highly polarised samples of the ^{129}Xe gas mixture and transport them to the MRI scanner without substantial loss of polarisation, the next natural progression was to image the hyperpolarised gas.

With the application of the gradients and RARE imaging sequence described earlier, it was possible to image ^{129}Xe in the whole body MRI scanner. Two images are presented in figure 6.12, both of $\sim 16\%$ hyperpolarised gas in the sample bag. The first (fig 6.12a) is taken with the bag partially filled and inserted into the solenoid Rx coil. The field of view was 383 mm square with a resolution of 64×64 bits but the image has been cropped for presentation purposes. The second image (fig 6.12b), is taken with a fully filled bag inside the body Tx coils and using the spiral Rx coil. For this image the original field of view was 630mm square with 64×64 resolution, but this has also been cropped for clearer display.

Several attempts to image the human lungs were made using both the body and spiral Rx coils, but all were unsuccessful. The procedure used for lung gas delivery was as described in section 6.1.4 and imaging attempts used a similar practice to the acquisition of FIDs from within the lungs, but this did not seem to satisfy the conditions for human lung imaging. The FFTs of the FIDs from the lungs did show a reduced level of signal in comparison to the FIDs taken from the bag or cell samples, and this SNR problem is thought to be the main reason for the inability to image inside the lungs at this stage.

6.2.3 Measuring Spin Diffusion

It is useful to be able to measure the apparent (restricted) diffusion coefficient of gas in the human lungs as this may be correlated to the average alveoli diameter. The extent of lung damage, by smoking for example, may then be correlated to alveoli size [66]. With hyperpolarised ^{129}Xe, it is hoped that ADC may be correlated with gas uptake of the human lungs.

The train of echoes received during the diffusion measurement of the gas sample in the Tedlar bag at 1 bar is shown in fig 6.13. The maxima of each echo is determined using Matlab and normalised against S_0. Charting the natural log of these normalised values against n gives a plot with linear coherence from which D may be determined (equ. 3.21). In both cases, only a certain range of points on the linear plot were used to generate the fit which reduces error in the line gradient stemming from the initial settlement and low amplitude region of the echo train. This fitting region is user defined in the Matlab program for each plot. The parameters for the diffusion imaging carried out here have been stated previously and produced values of D obtained for the 1.96 bar and 1 bar samples of 0.26 ± 0.11 cm^2 s^{-1} and 0.42 ± 0.07 cm^2 s^{-1} respectively. Plots for determining the diffusion

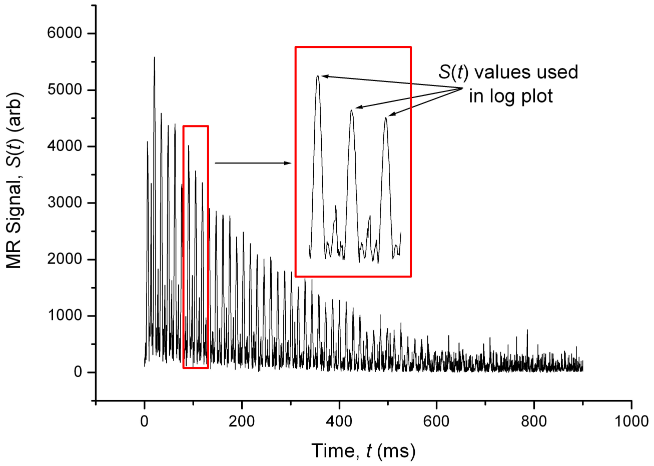

Figure 6.13: Raw data from a diffusion measurement of the gas in the Tedlar bag. In order to calculate D, the peak value of each echo is determined.

coefficient for both the gas in the cell and in the gas bag (1 bar) are shown in figure 6.14. In this study we were unable to achieve a meaningful diffusion measurement from the lung space.

6.3 Discussion

6.3.1 Spin Lattice Relaxation

T_1 measurements were made for identical mixtures of gas in several sample holders in a variety of environments. A summary of the data from these measurements is presented in table 6.1. The longest T_1 values for uncontaminated gas mixtures were measured inside the 0.15 T whole body scanner. If we consider the two lifetimes of the gas measured in the spherical cell, the only differences between the SE measurement and the scanner measurement are that the scanner is at a higher field and because the cell is elevated from the centre of the Helmholtz arrangement in the SE environment, the homo-

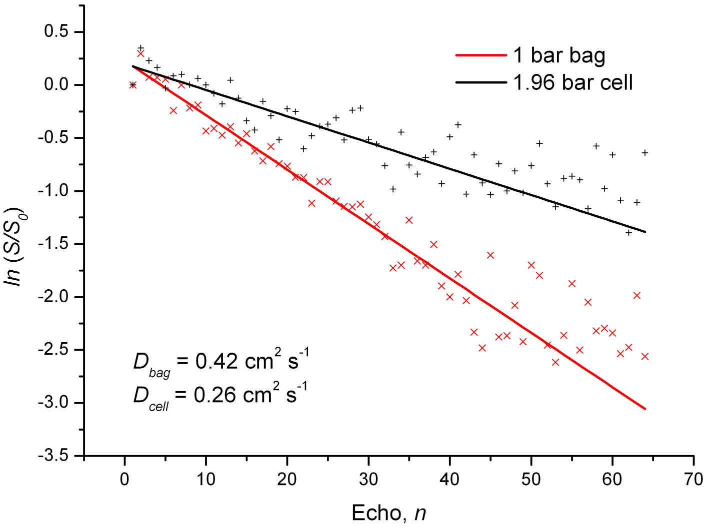

Figure 6.14: A plot of $ln(S/S_0)$ for each spin echo from each of the samples. The diffusion coefficient may be calculated from the gradient of each plot. In both cases the linear fit is made using echoes 3 to 40.

geneity over the sample volume will also be greater in the scanner. There is also perhaps, a small temperature difference of ∼10°C, as the SE oven will still be warm when the T_1 measurement is performed. Now assuming, that the wall relaxation rates, Γ_w, in the two environments are equal (which also assumes the elevated temperature has negligible effect on gas diffusion), the increased relaxation of the gas in the SE environment is due only to spin rotation relaxation, Γ_{sr}. In fact it has been shown for low densities of Xe that $1/\Gamma_w = \kappa r^2/\pi^2 D_{Xe}$ [49] where κ is the probability of relaxation due to a ^{129}Xe - wall collision which, for our OTS coated cell, we would expect to be small.

For low field measurements of ^{129}Xe T_1, it has also been shown that the contribution to spin lattice destruction from binary collisions is [49],

$$\Gamma_b = \frac{56.3hours}{[^{129}Xe]_{amagat}} \tag{6.1}$$

Sample	Pressure (bar)	Vol (ml)	Environment	T_1 (min)
Spherical Cell	1.96	33.5	Scanner	117.1 ± 5
Spherical Cell	1.96	33.5	SE	15.1 ± 1
Bag	1	~300	Scanner	131.9 ± 1.6
Bag	1	1000	SE	66 ± 22
Bag	1	1000	Contam. O_2	3.4
Lung	1	1000	Scanner	0.45
Cylindrical Cell	~2.5	160	SE	15.8

Table 6.1: A table summarising T_1 measurements made of the 3% Xe gas mixture used in this work. SE indicates that the measurement was made on top of the spin exchange oven except for the cylindrical cell where it was made inside the oven. The contaminated bag measurement was conducted inside the scanner.

which for our sample of 3% Xe at natural abundance, yields a T_1 >3600 hours. For this reason, we can assume that the relaxation rate of the polarised ^{129}Xe is due predominantly to Xe-Xe van de Waals interactions, Γ_{vdW}, and that this mechanism of relaxation is therefore either field strength or homogeneity dependant or both.

Unfortunately it is not possible to make a simple comparison between the T_1s for the spherical cell and the cylindrical cell in the SE environment to eliminate the dependence of homogeneity, since the cylindrical cell at the time of the measurement contained Rb and was also at a temperature of <75° C (decreasing due to cooling), but the fact that two T_1s agree does suggest that the effects of field inhomogeneity are unimportant providing the relaxation due to Rb vapour (see section 2.2.2), at this density, is also small.

From the above we conclude that the spin lattice relaxation rate T_1^{-1} defined by the BPP equation [97] for spin $\frac{1}{2}$ nuclei, relates only to van de Waals relaxation for the regimes investigated here,

$$T_1^{-1} = \frac{3}{4}\gamma^4\hbar^2[J(\omega_L) + \frac{1}{2}J(2\omega_L)] \tag{6.2}$$

where $J(\omega_L)$ is the spectral density function. The spectral density may be thought of as referring to the number of nuclei that are tumbling at or near ω_L and hence may give rise to relaxation. For relaxation not involving dipole interactions (ours is only due to van de Waals collisions), the double frequency term in the equation above may be absorbed into the effect of the single frequency term [98].

Hence we describe the decay of polarisation in terms of the time taken for the spin of a nuclei to rotate through a certain angle (1 radian), τ_c, with respect to a reference time, τ, which gives an auto correlation function,

$$G(t) = e^{-\tau/\tau_c} \tag{6.3}$$

where τ_c is normally referred to as the correlation time. The spectral density is simply the Fourier transform of this function $G(t)$ [99],

$$J(\omega_L) = \frac{\tau_c}{1+\omega^2\tau_c^2} \tag{6.4}$$

from which we can understand the effect of field strength on the variation in T_1 of similar samples. So from equations 6.2 and 6.4 we have the gas relaxation equation for our two NMR systems,

$$\Gamma_{Xe} = \Gamma_{vdW} = 3\gamma^4\hbar^2 \frac{\tau_c}{4(1+\omega^2\tau_c^2)}. \tag{6.5}$$

At resonance $\tau_c = 1/\omega_L$, which gives T_1 of,

$$T_1 = \frac{8B_0}{3\gamma^3\hbar^2} \tag{6.6}$$

for nuclei on resonance. This explains why the rate of relaxation decreases as the B-field increases but does not explain exactly the values of T_1 we achieve for our samples. That is to say, according to equation 6.6, T_1 should vary linearly with field for relaxation due only to van de Waals interactions, but our field normalised T_1s for the spherical cell in the scanner and the SEOP environment are 7.8 and 35.6 min $\mu\mathrm{T}^{-1}$ respectively. The exact T_1 of course is defined by $J(\omega)$ which also varies with B_0.

When comparing the relaxation times of different samples in the same environment, magnetic field strength has no effect on the discrepancies in T_1 values. Instead, we must consider the field independent mechanisms (if they exist) of wall and impurity depolarisation. If we consider the T_1 of the gas in the spherical cell and in the gas bag inside the scanner, it is clear to see that there is a measurable difference in relaxation rate between the two samples. Obviously, the spherical cell is at almost twice the pressure and so if both samples were of equal size, the relaxation rate due to wall collisions could be related to a pressure difference. However, the bag is also of larger volume and surface area, and it is constructed from another material. Therefore a comparison between the two samples is rather difficult. It should however be noted that there is a distinct decrease in T_1 by increasing surface to volume ratio and decreasing the pressure in a sample of hyperpolarised gas. These contributions to relaxation have been discussed in section 2.2.6.

One final point of interest with regard the spin relaxation rates of the gas measured in this section is that of the relaxation of ^{129}Xe in the presence of oxygen. For our hyperpolarised gas mixture inside a human lung, the T_1 of the ^{129}Xe was found to be 27.6 ± 4.4 s and for the uncalibrated gas bag contamination of oxygen, the T_1 was measured to be 206 s. Both of these indicate a considerable reduction in lifetime of the polarised state due to the presence of paramagnetic oxygen compared to our uncontaminated gas bag (131.9 ± 1.6 min). Relaxation of gas phase ^{129}Xe in the human lung has been investigated [95] and two values quoted (16 and 22 s) for two different volunteers in identical setups indicating some variation between subjects. The extent of the relaxation of ^{129}Xe due to contamination by O_2 was investigated some time ago by Hunt and Carr [100] with the relaxation of the polarised gas being inversely proportional to the partial pressure of O_2. Others [63] have reported on the significant effect of oxygen contamination with a 1:1 ratio of 90% enriched ^{129}Xe to O_2 reducing the T_1 for the ^{129}Xe by a factor of at least 1000.

Obviously in the lung, there exists a wide range of relaxation mechanisms, and it is the combination of these that result in the rapid increase in longitudinal relaxation rate that we observe. It is supposed that interactions with paramagnetic oxygen and high surface area account for the majority of ^{129}Xe relaxation within the lung. A similar effect is observed with hyperpolarised ^{129}Xe gas inside silica gel, reported in section 7.2.2 of this thesis. Unfortunately in this preliminary study, it was not possible to accurately characterise a correlation between O_2 induced ^{129}Xe relaxation and spin destruction due to surface interaction within the lung.

It was not really appropriate to assume that much of the ^{129}Xe is adsorbed onto the tissue of the lung where relaxation is slower, since, no chemical shift comparable with other studies [101] was observed in the resonance spectra. A broad chemical shift component was observed in the T_1 spectra data (fig. 6.11) which has not been commented on in previous literature despite being observed (eg. in ref. [67]). The most probable explanation for the broad shoulder in the spectra would be due to a field gradient across the lung at the time of imaging, but this has not been observed in ^{3}He studies on the same scanner and so can be eliminated. Mugler *et al.* [95] commented on a shift of the gas peak due to bulk magnetic susceptibility during a breath hold experiment similar to ours, but did not observe the line shape shown here.

It is difficult to comment on such an interesting artefact with such preliminary results though one possibility is that it is due to a semi-adsorbed state of the ^{129}Xe with either O_2 or with the lung tissue. With improvements to the RF detection system suggested later, higher frequency resolution or inside a higher field scanner, it would interesting to resolve the two observed components.

With ^{129}Xe longitudinal relaxation mechanisms present and the uptake rate of Xe into the lung tissue and blood stream, the T_1 of ^{129}Xe in the human lung is of the order of a few 10's of seconds in a breath hold experiment which is long enough to perform NMR investigations. It is therefore SNR and spectral resolution that define the success of these studies.

6.3.2 Imaging Sensitivity

With the polarised ^{129}Xe in the gas mixture produced by the SE polariser described in chapter 4 of this thesis, two gas filled samples were imaged using a RARE sequence. The first of the images, presented in this thesis is of a partially filled ($\sim$300 ml) Tedlar gas bag (fig. 6.12a) yielding a SNR of 55. This is a good clear image with some blurring in the y (phase encoding) direction due to diffusion of the gas [102]. Diffusion causes blurring in images as the gas moves in the sample between the phase encoding and read functions of the imaging paradigm such that a false indication of the position of a nucleus is given in the phase encoding direction only. The application of the gradients also affects SNR of the image. The blurring of MR images is a problem with free gas since the diffusion coefficient is so high unlike protons in the tissue of the body where the effects of blurring due to diffusion are minimal. The effects of blurring due to diffusion of free gas may be subdued by the use of ultra short spin echo (UTE) techniques [103] or by an increase in buffer gas pressures [67].

The implications from the ability to image the partially filled gas bag inside the small solenoid RX coil are good. With a bore of 63 mm the coil is not suitable for imaging the human body but the results imply that investigations on small animals could be carried out without any refinement to the setup.

As a precursor experiment, an image of a filled Tedlar gas bag was taken using the identical setup intended for lung studies. A clear image was achieved with SNR = 19 (fig 6.12b). The square shape of the bag is clearly identifiable with slight blurring due to diffusion. The increased signal in the centre of the bag is a consequence of two factors; there is more gas in the centre of the bag and the spiral Rx coil is more sensitive in this region. Indeed, the slight off-centring of the high signal region is likely to reflect the position of the Rx coil relative to the bag. With an image of this quality from the gas bag it was considered that an image would be possible from the lungs of a human volunteer.

It is with disappointment that no such image was obtained within the scope of this project. Although the system was sensitive enough to detect NMR from within the lungs, there was no evidence of signal in any of the images attempted with either the spiral Rx or body Rx coils. The body Rx coil was, admittedly, a rather rushed design and was not truly expected to ever produce presentable results, but rather was built more to investigate the possibility of 3D coil design in our preliminary imaging setup. In bench-top investigations, the volume dependent signal pick-up was found to be inferior to that of the spiral coil over the region occupied by a human lung. The spiral coil, however had produced quite reasonable results and had proven itself to be reliable, but continued to fail to produce a lung image despite our best efforts in tuning, matching and positioning the coil. It was noticed that the presence of a body next to the coil caused some detuning and so the coil was retuned in the presence of a human subject. Further, both FIDs and images were acquired from a bag of gas in the setup whilst in the presence of a large water bottle, in an attempt to mimic a body. We also managed to image the bag placed on top of our volunteer's chest with the Rx coil in contact with the bag. With this we could eliminate the possibility of detuning and could attribute the lack of image to low SNR. Therefore in order to image the human lungs, a more advanced and sensitive coil design needs to be adopted with the use of higher concentrations of hyperpolarised ^{129}Xe.

An obvious enhancement in the system would be to wind and tune a ^{129}Xe coil around a mandrel designed to be incorporated into the scanner as this would allow a more homogeneous B_1 field to be generated over a larger volume, whilst allowing more freedom in Rx coil design. This would admittedly introduce problems with corrective gradient shimming (which is performed on a proton phantom) as the current Tx coil is capable of resonance at both ^{1}H and ^{3}He (normal scanner operation) frequencies.

Certainly, the design of an appropriate volume Rx coil would enable enough pick-up of signal to perform human imaging. Generally, other ^{129}Xe imaging groups use modified versions of commercially produced sodium NMR coils. The design of such a coil is beyond the scope of this project.

6.3.3 Diffusion of ^{129}Xe

The ability to measure the diffusion of gas within the human lung is a useful method with which to determine alveolar size. Because of the large diffusion coefficients of gases, in small cavities measured diffusion refers to an apparent diffusion of the gas restricted by the boundaries of the cavity. Because free gas at atmospheric pressures diffuses each second of the order one hundred times the diameter of human alveoli, then the ADC of hyperpolarised gas within the lung correlates with alveolar size.

Two diffusion measurements were made of the free gas mixture at different pressures with coefficients 0.42 ± 0.07 and 0.26 ± 0.11 cm^{2}s^{-1} for atmospheric pressure and 1.96 bar respectively. However, it is known that gas diffusion coefficients scale inversely with respect to pressure [104] and so since the gas in the bag is by definition at 1 bar, the gas in the cell (which is of identical composition) can be calculated to be at 1.6 ± 1 bar which agrees with the volume calculated pressure given the fact that it has such a large error margin.

It is possible to calculate the free diffusion coefficient, D, for a gas x in a mixture providing the diffusion of x is known for infinite dilution in each of the present gases and that the partial pressure of each gas in the mixture is known using [67, 105],

$$\frac{1}{D_x} = \frac{P_x}{D(x-x)} + \frac{P_a}{D(x-a)} + \frac{P_b}{D(x-b)} + \dots \tag{6.7}$$

where P_x is the partial pressure of gas x and where $D(x-x)$ and $D(x-a)$ are the diffusion coefficients of gas x in gases x and a respectively. In practice, D varies with temperature, but since our measurements were conducted at room temperature, the effects of this variable shall be ignored.

For our experiments, the gas composition remained constant and consisted of 3% natural abundance Xe, 10% ^{14}N$_2$ and 87% ^{4}He. Since, with NMR, we are observing only one of the nine natural isotopes of Xe, the likelihood of being able to cite values for D_{129Xe} in each of the remaining isotopes is small and the above equation may become rather cumbersome. But it has been shown that the difference between D_{3He} in ^{3}He and ^{4}He where the properties of the nucleus are greatly affected by the difference of 1 nucleon is only a ratio of 1.069 [105]. It is therefore reasonable to assume that the average effect on the diffusion of the much larger atom ^{129}Xe from its isotopes is negligible and so $D(^{129}Xe -^{n} Xe)$ may be treated simply as $D(Xe - Xe)$, the self diffusion coefficient of Xe. This means that for our experiment, equ. 6.7 may be rewritten as,

$$\frac{1}{D_{xe}} = \frac{P_{Xe}}{D(Xe - Xe)} + \frac{P_N}{D(Xe - N)} + \frac{P_{He}}{D(Xe - He)}. \tag{6.8}$$

From Mair *et al.* [104] we know that the self diffusion coefficient at 1 bar for Xe, $D(Xe-Xe)$, is 0.0571 cm^2 s^{-1}. Two conflicting values of the diffusion of Xe in N$_2$ are found in references [106] and [107] where $D(Xe-N)$ is stated as 0.120 cm^2 s^{-1} and can be inferred (using a method described in ref [104]) to be 0.0283 cm^2 s^{-1} respectively. In a recent study of binary mixtures, Acosta *et al.* [108] finds $D(Xe-^3He)$ to be (on average) 0.625 cm^2 s^{-1}. If we incorporate the relationship derived from ref [105], we find that $D(Xe-He)$ is 0.585 cm^2 s^{-1}.

For our gas in the Tedlar bag, the partial pressures of the gases are; $P_{Xe} = 0.03$, $P_N = 0.10$ and $P_{He} = 0.87$ bars. From equ 6.8 we then get $D_{Xe} =$ 0.351 cm^2 s^{-1} (using $D(Xe - N)$ from [106]) which, within error, agrees with our measured value of diffusion. Using the value of $D(Xe - N)$ from ref. [107], we obtained $D_{Xe} =$ 0.180 cm^2 s^{-1} which does not agree with our measured diffusion. The precise conditions under which this reference value was obtained are a little ambiguous and it is hypothesised that the diffusion of the gas was restricted yielding a lower value for the observed ^{129}Xe than would be found in a truly bulk sample. For this reason, the second of the two calculations will be disregarded.

The agreement between our measured diffusion coefficient and our calculated diffusion coefficient shows that we are able to reliably measure ^{129}Xe spin diffusion in a gas mixture and correlate this value to pressure. Being able to measure differences in the apparent diffusion coefficient of ^{129}Xe in lung spaces will be useful for determining alveoli sizes and oxygenation levels in this difficult to probe environment.

Chapter 7

^{129}Xe in Liquids and Porous Materials

Applications of hyperpolarised ^{129}Xe reach further than gas imaging and spectroscopy to include dissolved solution NMR and analysis of porous materials and surfaces. The solubility of Xe in lipids and globins, and its interactions with proteins [15] makes ^{129}Xe an ideal tool for probing the function of the human body. In particular, the solubility of Xe in blood [109] makes it ideal for NMR studies of the human circulatory system and organ function. Further, the very high Ostwald coefficients for Xe in solvents, suggests ^{129}Xe is ideal for the study of flow systems and porous media, though little work has previously been reported in this area.

The structure of silica gels has previously been investigated using high pressure thermally polarised ^{129}Xe NMR [110, 111] and hyperpolarised ^{129}Xe [112, 113] with empirical correlations proposed between the porous structure and chemical shift of the ^{129}Xe. The porosity and effective permeability of porous rocks have been simultaneously measured using hyperpolarised ^{129}Xe [114]. The measured porosity was comparable to industry standards but the effective permeability was found to vary with gas flow rate. The proportion of ^{129}Xe adsorbed onto pore surfaces yields information on the general porosity of the material, whilst effective porosity is revealed by flow of hyperpolarised gas through a material.

Relating studies of porous media to those of lung spaces, Butler *et al.* [115] have demonstrated a technique that measures the surface to volume ratio in soft porous materials. They simultaneously monitor both the diffusion of the free gas and the rate of uptake of ^{129}Xe onto the material surface with the potential to measure *in vivo* lung function.

This chapter details investigations carried out using ^{129}Xe in solvents and lipids and of some gaseous and dissolved state studies of ^{129}Xe in silica gel and sintered glass.

7.1 Experimental

The production and transportation of hyperpolarised ^{129}Xe gas has already been described as has the design of the whole body MRI scanner used in all experiments. The NMR setup used for these smaller scale experiments consisted of the Helmholtz Tx and solenoid Rx coils presented in section 6.1.3. The NMR pulse sequences are appropriate to each experiment and are described in sections 3.6 and 6.1.5.

7.1.1 Solutions

The applicability of two liquids, olive oil and toluene, to dissolved solution NMR were investigated using hyperpolarised ^{129}Xe. With an Ostwald coefficient[1] of 1.79 [12] for Xe in olive oil, it is possible to increase the signal

---

[1] The volume of gas which dissolves into 1 unit volume of liquid at a standard temperature.

density of hyperpolarised ^{129}Xe by dissolving it in a sample of this lipid. For this experiment, 20 ml of olive oil was introduced into a 60 ml syringe and any free gas or bubbles ousted by tapping the vertical syringe and expelling the headspace gas. A Luer-Lok valve, attached to the end of the syringe, was closed once the free gas was expelled, reducing the risk of leakage or contamination of the oil by air. The syringe was then placed inside the Rx coil located within the body scanner. A bag of hyperpolarised ^{129}Xe gas mixture was produced, transported to, and placed inside the magnet bore. The gas bag was connected to Luer-Lok valve via a short length of PFA tubing (see fig. 7.1). Just before connection, any air in the tubing of the bag was flushed out with a small burst of gas from the bag. With the valves on the bag and the syringe opened, 40 ml of hyperpolarised ^{129}Xe gas mixture was introduced into the syringe. The valves were then closed and the bag and syringe disconnected. For optimal dilution of Xe in oil, the syringe was shaken vigorously for 10 seconds, which is a compromise between Xe uptake and relaxation of the dissolved gas. One sample of oil could be used for a number of experiments with the recognition that the effective Ostwald coefficient reduces with use, as fewer sites for absorption become available.

The second liquid investigated was toluene, which for Xe has an Ostwald coefficient of $\sim$5 [116]. The higher Ostwald coefficient, coupled with the fact that toluene is less viscous than oil, enabling smaller particulates and a larger surface area to be generated for adsorption of Xe during mixing, makes the uptake of Xe into toluene much more efficient then for Xe into oil. Preparation of toluene samples were carried out in much the same way as for olive oil and a range of volumes were investigated. Because of its solvent characteristics, toluene presented a few problems with degradation of some components of the sample preparation and gas filling system. The toluene

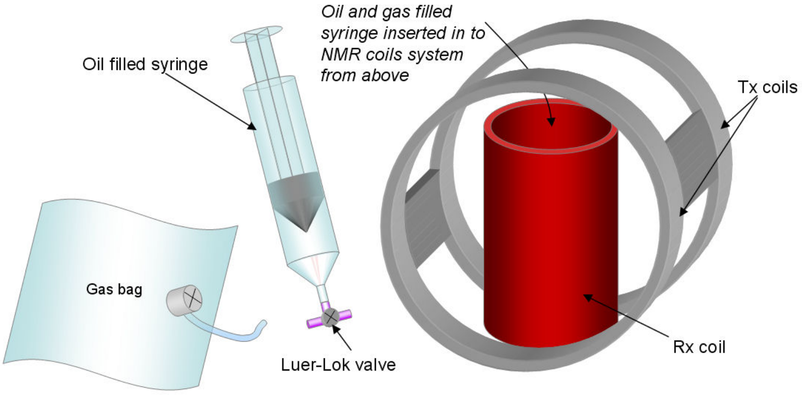

Figure 7.1: Diagram of setup used during NMR investigations on ^{129}Xe gas in olive oil.

also absorbed into the rubber plunger of the syringe (in a relatively short length of time), which caused it to swell and seize. These problems were resolved by regular replacement of the affected components.

7.1.2 Porous Media

Four porous samples were investigated using hyperpolarised ^{129}Xe; a 15 cm^3 volume of silica gel (grade 646, 35-60 mesh, 150 Å, W. R. Grace & Co., Maryland) and three sintered glass samples with porosity reference numbers 0, 1 and 2 (relating to mean pore sizes 150-200, 90-150 and 40-90 μm respectively). The silica gel was encapsulated inside a 20 ml cartridge which included a small volume of foam at each end to prevent loss of the silica. The silica sample was evacuated for 1 hour at 120 °C. A combination of a T-piece Luer-Lok valved connector at the inlet of the cartridge and a one-way valve at the outlet, facilitated the filling of the sample with the hyperpolarised gas mixture whilst reducing the possibility of contamination from the atmosphere. The gas was introduced into the sample by squeezing the bag for a second (max flow was ~100 ml s^{-1}) which displaced the silica's interstitial gas volume a number of times over, ensuring a minimal amount of depolarised gas remained. For timed experiments, the interval between a flush of gas and a pulse was estimated, but was intended to show a trend in the characteristics of ^{129}Xe in silica rather than a means to perform accurate measurements.

The sintered glass (SG) samples required drying before experimentation took place. Each sample was dried by a continuous flow of nitrogen gas over night. The glass was considered dry, when no more residue could be seen in the end spaces of the Perspex cylinder and this condition was verified by the absence of a proton NMR signal from the samples. Any condensation of atmospheric vapour into the SG was monitored by weighing the samples once dry and then at frequent intervals.

All three sintered glass samples are 33 mm diameter by 50 mm cylinders affixed into 50 mm diameter perspex cylinders by epoxy resin. A small volume of free space exists at either end of the perspex cylinders which are hermetically sealed except for one inlet and one outlet port which are both Swagelok NPT 1/4". The introduction of gas was facilitated by a Luer-Lok manifold which connected two 60 ml syringes and the polarised gas bag to the perspex cylinder (fig 7.2). The gas was drawn into the syringes from the bag, which was then sealed. The syringes were emptied through the sintered glass sample, which depending on porosity, provided a certain level of resistance and therefore variable flushing times. Any time dependent measurements were conducted from the cessation of flow.

SG0 was investigated when whetted with toluene, which was introduced through one of the ports and forced through the porous material using a flow of nitrogen. This was repeated in both directions to ensure an even filling of the sample. Unfortunately the toluene had a detrimental effect on the

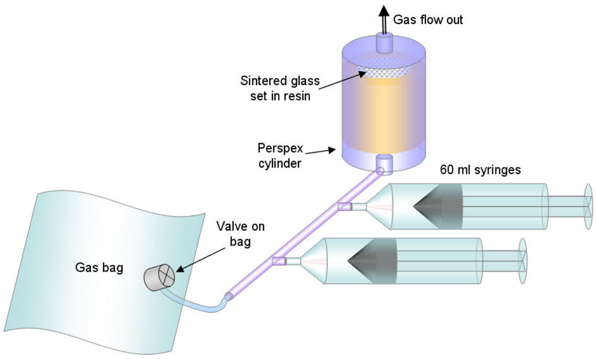

Figure 7.2: Diagram representation of the setup used during studies on sintered glass. The sample resides inside the solenoid Rx coil within the scanner whilst the gas is forced through the porous glass. Both the inlet and outlet ports have the capability of being sealed.

perspex, causing major stress lines and eventual fracture of the material.

7.2 Results

Preliminary results concerning the ability to use hyperpolarised ^{129}Xe as an NMR marker in lipids and solvents inside a low field whole body MRI scanner are presented in this section. NMR data taken from hyperpolarised ^{129}Xe gas inside materials with various porosities and from studies using dissolved solution ^{129}Xe NMR in the pores of sintered glass are also presented.

7.2.1 ^{129}Xe in Lipids and Solvents

With a relatively short T_1 when dissolved in olive oil, it was not possible to achieve complete absorption of Xe before significant relaxation of ^{129}Xe polarisation had occurred. Therefore the observed resonance spectra contain both the absorbed and free gas resonances (fig 7.3). The shift in frequency of the absorbed ^{129}Xe is 321 Hz for the 0.15 T field, which corresponds to a

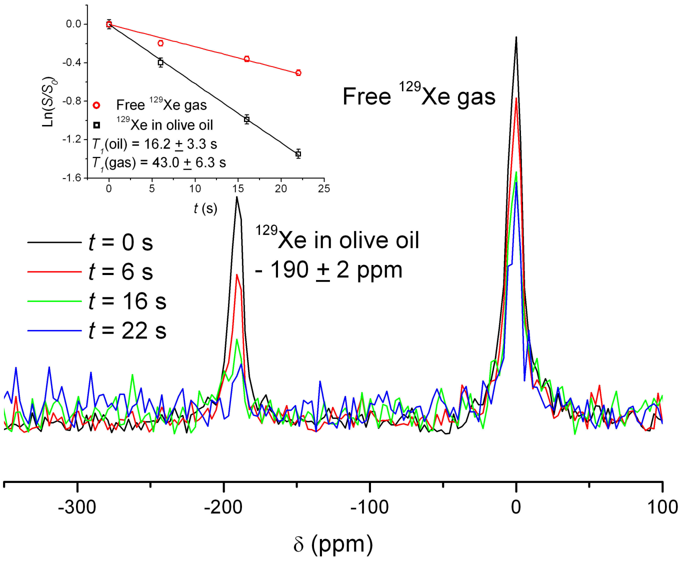

Figure 7.3: Resonance spectra from ^{129}Xe dissolved in olive oil (showing δ = -190 ± 2 ppm). The free gas peak arises from the non-absorbed gas remaining in the 'headspace' of the syringe and is not present if this gas is expelled. *Inset*, a plot of Ln(S/S_0) over time for both the dissolved and free gas, from which the corresponding spin lattice relaxation times for ^{129}Xe can be deduced.

chemical shift of -190 ± 2 ppm. The T_1 of the gaseous and absorbed ^{129}Xe were measured by pulsing the sample as rapidly as the NMR system would allow (which is at $\sim$ 6 s intervals) with a 50° tipping pulse. T_1s were found to be 43.0 ± 6.3 s and 16.2 ± 3.3 s for the gas and absorbed states of ^{129}Xe in olive oil respectively.

The receptivity of toluene to Xe meant that a 10 second shake of the syringe containing both the liquid and gas mixture was sufficient for practically all of the ^{129}Xe to be dissolved (fig 7.4). The corresponding chemical shift was found to be similar to that of ^{129}Xe in olive oil at -190 ppm. A T_1 measurement of the dissolved gas was made using 2.0° tip angle pulses and the lifetime found to be 268 ± 27 s. A T_1 measurement of the non dissolved gas in the syringe could not accurately be made because of large relative errors in

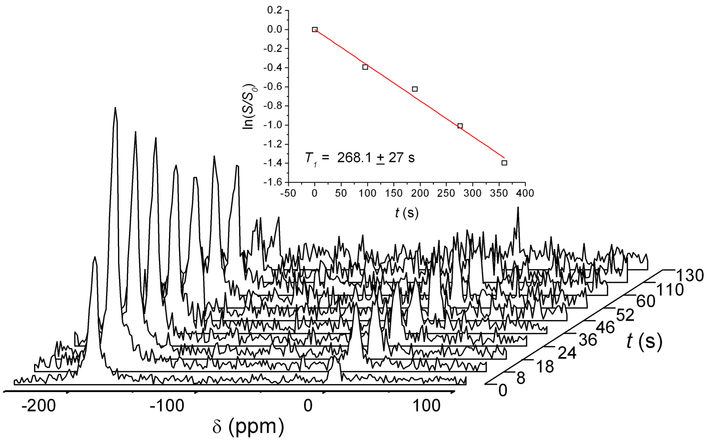

Figure 7.4: Spectra of ^{129}Xe in toluene (-190 ppm) and free ^{129}Xe gas (0 ppm) over 130 s time period. The t axis is not linear and the increase in background noise over time is due to a correction factor which accounts for the 8.3° tipping pulses used during data acquisition. *Inset*, a T_1 plot for dissolved ^{129}Xe in a renewed toluene sample.

the gas phase value due to a low partial pressure of undissolved ^{129}Xe. From a plot showing the evolution of the two (gas and dissolved) resonance peaks (fig 7.4) after a 10 second shake of the toluene and gas filled syringe, an initial rise in the size of both peaks (which have similar linewidths) is present which is interesting, since the total amount of ^{129}Xe remains constant. Therefore, some condition of the gas prevents it from being either efficiently excited or detected by the NMR hardware.

With Xe from 40 ml of gas (0.29 ml of hyperpolarised ^{129}Xe) dissolved into 20 ml of toluene, it was possible to image the solution using MRI. Figure 7.5 shows an image of the solution in the bottom of a syringe, with a SNR of 60. The image was taken using the sequence described in section 6.1.5 with a field of view of 45 mm and no slice selection.

Attempts were made at the cross polarisation of hydrogen within the toluene, using hyperpolarised ^{129}Xe by thermal mixing. Cross relaxation

Figure 7.5: Image of ^{129}Xe dissolved in toluene in the bottom of a 60 ml syringe. The image has an SNR of 60 and it is possible to make out the conical shaped end of the syringe. There exists practically no signal from ^{129}Xe in the gas phase above the toluene.

does not occur between nuclei with different gyromagnetic ratios in large magnetic fields as the allowed energy transitions of the two types of nuclei do not match. To overcome this, the magnetic field may be cycled rapidly to almost zero where the energy transitions between the two nuclei are similar ($\gamma_1 \hbar B_0 \approx \gamma_2 \hbar B_0$) allowing relaxation of the polarisation of one species to enhance the polarisation of the other. With the reapplication of the high field, a transfer in polarisation from species 1 to species 2 should be observed. Unfortunately our attempts at thermal mixing were unsuccessful within the scope of this thesis. The failure to achieve an enhancement in ^{1}H polarisation using this method was attributed to the our slow method of field cycling; the toluene dissolved ^{129}Xe sample had to be removed a sufficient distance from the bore of the permanent field MRI scanner and then replaced manually. Relaxation of both the ^{129}Xe and ^{1}H polarisations were greatly enhanced by this long period (∼10 s) outside of the scanner's homogeneous magnetic field.

7.2.2 ^{129}Xe in Silica Gel

The polarised gas mixture was successfully introduced into a cartridge containing 15 ml of silica gel. FIDs (using 90° tipping angles) from the ^{129}Xe

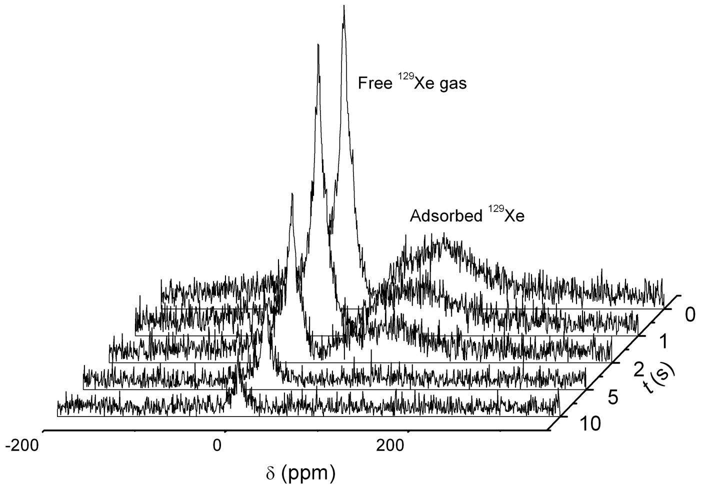

Figure 7.6: Decay of ^{129}Xe spectra in silica gel sample over a 10 s time period. The signal from the gas phase ^{129}Xe decays almost as fast as the signal from the adsorbed ^{129}Xe .

inside the cartridge were taken at various time intervals ranging from 0 to 10 seconds (fig 7.6). The spectra show one narrow peak, typical of the free gas phase of ^{129}Xe, and one broad peak, attributed to the absorbed ^{129}Xe on the surface of the silica, with a central chemical shift of $\sim$ 103 ppm and a FWHM of $\sim$ 80 ppm. The T_1 of the adsorbed component could only be estimated since the signal decayed too quickly and it was not practical to improve the timing intervals of the NMR pulses. The T_1 for ^{129}Xe adsorbed onto the silica gel surface is in the region of 1 s. The signal from the gas phase ^{129}Xe was also short lived and was found to be 4.5 $\pm$ 0.5 s.

It was hypothesised that the majority of the gas signal emanated from the sponge regions either side of the silica sample in the cartridge. This was verified by taking a series of 1D MR images of the gas in the sample and plotting the results using a pixel by pixel intensity analysis. A 1D image is taken using the spin echo technique described earlier in this work (section 3.6.1) and by omitting the frequency encoding read gradient. The

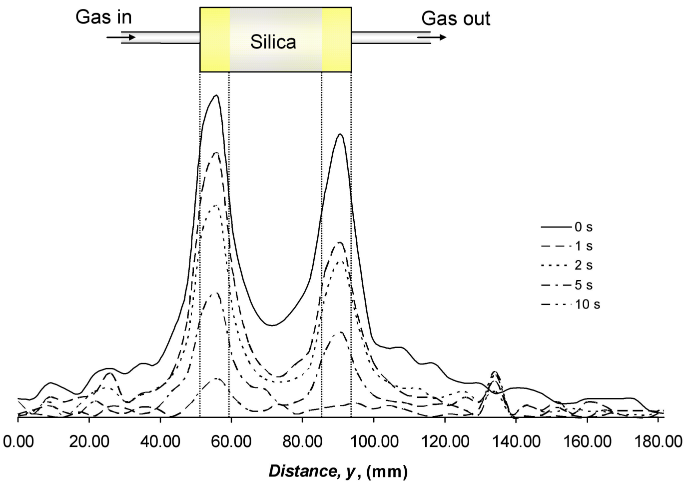

Figure 7.7: Signal from ^{129}Xe along y (vertical) axis of silica cartridge with respect to time. The majority of the signal emanates from the gas in the sponge filled regions of the cartridge.

result is shown in figure 7.7. From this, it is clear to see that the majority of the gas signal originates from the gas in the sponge regions. This is not unexpected however, since these regions are by far the most porous inside the cartridge and therefore contain most gas. Further, the continual adsorption-desorption of interstitial gas inside the silica sample introduces an effective decay of the NMR signal from the gas in these regions. The adsorbed gas contributes very little to the signal in the 1D images as its T_2^* is very short; a consequence of its broad resonance. One final observation, is the reduction in polarisation of the gas due to its passage through the silica gel. Obviously this is a function of the ^{129}Xe concentration in the gas and its rate of flow through (or rather residence time inside) the silica. In this case the gas was forced through the sample at a rate $\sim$100 ml s^{-1} (residence time $\leq$0.2 s) which caused an average reduction in polarisation between the first and second sponge filled regions, of 29%.

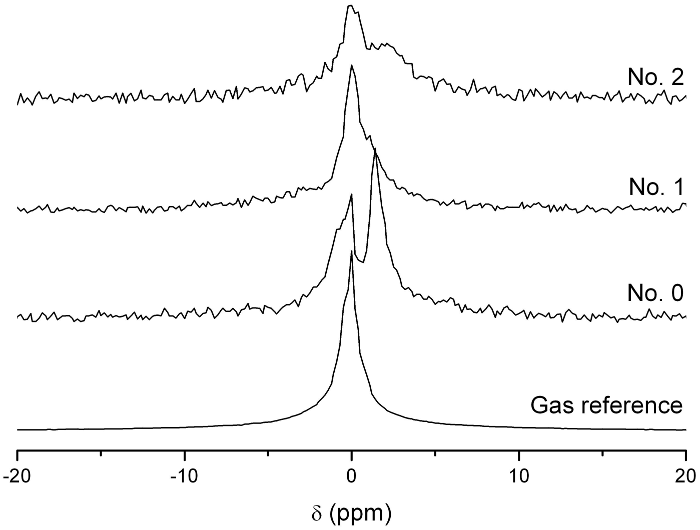

Figure 7.8: Resonance lineshapes from ^{129}Xe inside the three sintered glass samples. The peak attributed to gaseous ^{129}Xe for each spectrum is centred on 0 ppm. The spectra from the sintered glass samples are all on the same scale whereas the reference peak has been normalised to the signal from SG0.

7.2.3 ^{129}Xe in Sintered Glass

The dry sintered glass samples were subject to basic NMR analysis at high frequency resolution (0.31 Hz). The hyperpolarised ^{129}Xe in each of the samples exhibited a different resonance line shape (fig 7.8). To verify the existence of these multiple resonances, the decay of polarisation was measured in each sample. With reduced tipping angles required for T_1 measurements, SG1 and SG2 produced low signal to noise, but SG0 showed two distinct peaks with independent decay times (fig 7.9). The frequency shift of this 2nd resonance, which is attributed to gas phase resonance, is 2.4 ± 0.3 Hz, much smaller than any adsorbed or dissolved state shift observed previously.

The lower frequency resonance component from ^{129}Xe in the sintered glass samples, is thought to arise from the gas mixture in the end voids of the perspex sample holder (see fig 7.2) where relaxation of the ^{129}Xe stems from wall relaxation and atmospheric contamination. The higher frequency peak is hypothesised to emerge as a result of the interstitial ^{129}Xe within the pores of the sintered glass. The increased surface area inside the sintered glass is the cause of the enhanced relaxation whist the frequency shift observed can be attributed to a magnetic signature of the porous glass. The existence of magnetic impurities within the silica glass was verified by repeating the experimental procedure for these samples using hyperpolarised ^{3}He which also revealed two resonance peaks in the frequency domain. ^{3}He does not exhibit a chemical shift and so the double resonance was proven to arise from magnetic impurities within the sintered glass. For the sintered glass sample 0, the frequency shifts from the ^{129}Xe and ^{3}He gases were normalised with respect to their gyromagnetic ratios, and the average field experienced from the sintered glass material was found to be 0.222 ± 0.004 and 0.254 ± 0.001 μT for ^{129}Xe and ^{3}He respectively. These values agree within error, the extent of which, are determined by the resolution of data acquisition.

The magnetic impurities in the sintered glass are likely to have been introduced during manufacture from the Glassblower's tools. Since the production of these sintered glass samples was not commissioned by our group, the exact cause of contamination is difficult to trace. The applicability of hyperpolarised gases for the possible analysis of magnetic impurities in materials has been realised in this result. Unfortunately poor signal to noise prevented further investigation into the possibility of hyperpolarised gas NMR characterisation of these porous media.

Sintered glass sample SG0 was filled with 2.582 ml (2.226 g) of research grade toluene and hyperpolarised ^{129}Xe was introduced in the same way as with the dry sample. Two distinct resonance peaks were observed which could be attributed to ^{129}Xe dissolved in toluene at a chemical shift of -

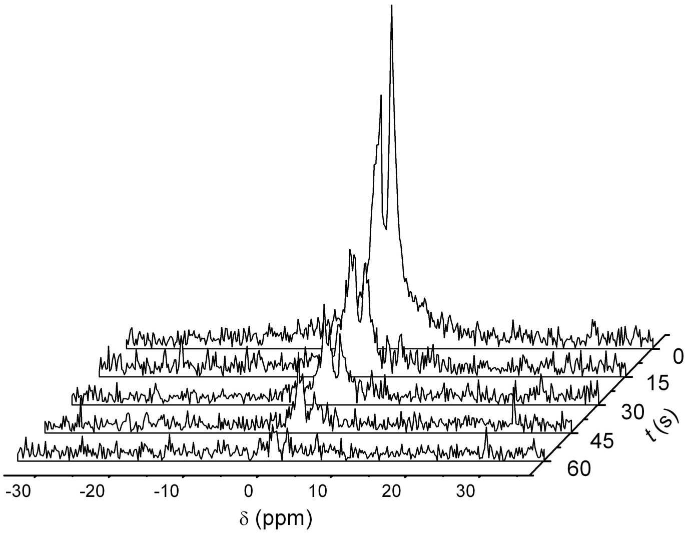

Figure 7.9: The decay of signal within the No. 0 sample. The two peaks decay at different rates with the T_1 of the left hand peak attributed to free gas in the end spaces of the sample, equal to 30.0 s. The T_1 of the right hand peak which has been attributed the interstitial gas within the sample, equal to 20.5 s.

186 ppm and the gas phase resonance. The T_1 of each of the free and dissolved ^{129}Xe resonance peaks was measured and the results shown in figure 7.10. Also presented is the spectrum from the sample filled with 5.935 ml (5.118 g) of toluene. The decay of signal from the resonance peaks does not follow the normal T_1 decay line. From the decay of the toluene peaks, there appears to be a definite slowing down factor of signal decay whilst the decay of the free ^{129}Xe signal increases with time. This behaviour can be attributed to uptake of ^{129}Xe by adsorption into the toluene with time. Unfortunately, fracture of the sample holder caused by chemical attack from the toluene prevented further investigation of this sample.

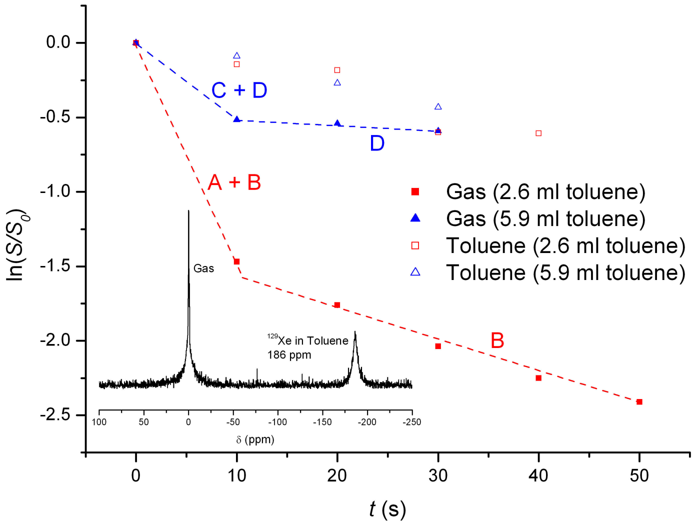

Figure 7.10: The decay of signal for the gaseous and dissolved states of ^{129}Xe in the toluene impregnated sintered glass samples do not follow the normal T_1 exponential decay, but rather follow a combination of exponential functions determined by the transition of ^{129}Xe between states. The dashed lines are guides for the eye with associated gradients labelled. *Inset*, the spectrum from a single NMR acquisition.

7.3 Discussion

The observed chemical shift of ^{129}Xe in olive oil of -190 ± 2 ppm does not agree with that found in literature of -197 ppm [117] at infinite dilution. The density dependence of chemical shift has been linked to pressure [118], but has minimal effect in our experiments and the temperature dependence of the chemical shift has been shown to be in the region 0.2 ppm $^{\circ}C^{-1}$ at room temperatures [117]. Therefore, experimental conditions do not significantly contribute to the discrepancy in chemical shift observed.

If we consider the chemical shift of -190 ppm measured for ^{129}Xe dissolved in toluene, we find that it agrees very well with published values found in references [116, 117, 119]. Therefore, system induced errors or malpractice can be eliminated from the source of the olive oil chemical shift discrepancy. It is possible that the specific type or grade of oil has a significant impact on the distortion imposed upon the electron cloud of the ^{129}Xe which transpires as a variation in chemical shift. This exemplifies the sensitivity of the chemical shift of ^{129}Xe to its local environment and indicates the applicability of hyperpolarised ^{129}Xe to species specific NMR.

Interestingly, the T_1 of the non-dissolved ^{129}Xe in the oil filled syringe fell from over two hours (for the gas mixture in the Tedlar bag) to 43.0 ± 6.3 s. The enhanced relaxation is considered to be induced by atmospheric contamination and increased (oil coated) wall relaxation.

With a short T_1 (16.2 ± 3.3 s) in the dissolved state for olive oil, the applicability of hyperpolarised ^{129}Xe in lipids for biological studies is limited to short spectroscopic and imaging studies rather then lengthy functional studies. These studies would rely upon rapid uptake of ^{129}Xe into the lipid based subject otherwise high signal to noise results are unrealistic. However, the relaxation of ^{129}Xe in toluene was found to be slow enough to perform accurate T_1 measurements and so lends itself to experimental NMR studies with the time scale of the order of one minute.

After shaking the toluene and gas filled syringe and swiftly placing within the NMR Rx coil, an initial rise in signal from both the free gas and dissolved phase ^{129}Xe was observed (fig 7.4) on a number of occasions, and was also witnessed after the introduction of the hyperpolarised gas mixture into sintered glass samples. Since on all occasions, the amount of ^{129}Xe in the system was fixed, the initial suppression of NMR signal proves a rather curious phenomenon. Some condition of the ^{129}Xe prevents it from being either excited or detected efficiently by the NMR hardware. The possibility that Xe may have been entering from outside the region of interest during this period has been ruled out. No adequate explanation could be contemplated for this initially subdued signal and no reports of similar observations were found to have been reported in literature.

It is clear from the presented spectra (figs 7.3 and 7.4), that for similar experimental procedures, the uptake of Xe in toluene is much more efficient than for Xe in oil. The absorption sites for Xe in toluene are benzene rings which accept a single Xe atom each, which is why the solubility of Xe in this and similar substances is so high. The chemical shift in ^{129}Xe is caused by polarisation of its large electron cloud, which for aqueous solutions normally results in a deshielding effect [117]. The chemical shift observed for ^{129}Xe in the toluene sample concurs with this. The method used here for NMR of ^{129}Xe dissolved in solvents is successful. This suggests toluene and most likely other solvents with high Ostwald coefficients for Xe, such as ethanol, 2.5 [120], are ideal for spectroscopic experiments in flow systems and porosity measurements of materials.

Within the silica gel sample, Xe rapidly undergoes a sorption-desorption cycle with the silica surface. Hence it may be expected that the FID of the ^{129}Xe spectrum can be split into a gas phase component and an absorbed component. However, the large spectral width of the adsorbed resonance prevents these components from being resolved. The short T_2^*, due to a broad resonance linewidth, explains the absence of NMR signal from the silica region of the 1D images taken of the gas filled sample 7.7. The lack of signal from this region implies that the free gas in the interstitial regions of the silica gel are in constant sorption interactions with the surface of the silica. On average, the farthest distance from the surface that the ^{129}Xe can be is half of the general pore size of the sample, which in this case is 75 Å. At a Xe diffusion rate of the order 0.4 cm^2 s^{-1} (for free gas in our mixture), the mean time between wall collisions is a fraction of a microsecond. This defines the upper limit for the rate of the sorption cycle of ^{129}Xe onto the surface of the silica. This rapid absorption rate is the reason for the absence of free gas signal in our 1D images.

The possibility of performing diffusion measurements of ^{129}Xe in silica gel using the current facilities is not realistic, especially for samples with smaller or comparable pore sizes to our silica gel sample. T_1 measurements are only really possible providing good SNR can be achieved with rapid pulse repetition times. NMR measurements on silica gel using a continuous flow of polarised ^{129}Xe could hopefully facilitate characterisation of samples with unknown properties.

To increase the density of polarised nuclei, toluene was utilised for investigations of a sintered glass sample and it was found that the polarisation of the dissolved and free ^{129}Xe did not decay as described by equ. 3.16 for either state. Instead, the NMR signal from the gas phase decayed with a double exponential. Conversely, the train of signals from the dissolved state nuclei represent the subtraction of one exponential from another, each having different decay constants. These extra exponential factors in the time dependent signal are ascribed to the time dependent absorption of Xe into the toluene. For absorption to occur, the Xe gas must first physiadsorb onto the surface of the toluene. The rate of this adsorption is the product of the flux, F, of atoms reaching the surface of the absorbant and the probability, P_{ads}, that a colliding molecule will be adsorbed,

$$R_{ads} = F \cdot P_{ads}. \tag{7.1}$$

For a fixed volume of gas, F itself is dependent on time, since the reduction in the number of free Xe atoms, N_{free}, as they absorb into the toluene will lead to a subsequent decrease in flux. Since for one particle in a box of length L with velocity ν_x the rate of collision with one wall is $2L/\nu_x$, it can be shown that for a fixed volume, V, in a system containing N_{free} absorbates that,

$$F(t) = \frac{\bar{\nu_x}}{2V} N_{free}(t) \tag{7.2}$$

assuming elastic collisions and where $\bar{\nu_x}$ is the mean velocity of the adsorbate perpendicular to the plane of the adsorbant.

The rate at which N_{free} decreases is dependent on the rate at which atoms are absorbed into the liquid and this gives rise to an absorption time constant, T_{abs}, assuming no desorption occurs. Therefore we have,

$$N_{free}(t) = N_0 e^{-(t/T_{abs})} \tag{7.3}$$

where N_0 is the number of free Xe atoms at $t = 0$.

The adsorption probability is a property of the particular adsorbate-adsorbant system and obeys the condition: $0 > P_{ads} > 1$. This probability depends on a number of particular factors relating to the two substances of interest, but foremostly, it depends upon the adsorbates existing inhabitance of the adsorbant liquid. If we assume that due to self diffusion of the toluene, the coverage of adsorption sites is minimal throughout the experiment[2], which implies that the number of absorption sites is much greater than the number of Xe atoms, P_{ads} can be assumed to be a constant value.

Since adsorbed gas becomes absorbed with the self diffusion of toluene, the rate of desorption is initially much lower than the rate of absorption and is dependent on the Xe coverage of the surface layer of the toluene. This has a counteracting affect to the true absorption rate giving rise to a lower apparent absorption rate which has the effect of increasing the absorption time constant of the free gas. At some point after the introduction of gas into the environment containing toluene, the rates of absorption and desorption will equate and no overall transfer of Xe will occur. The rate of overall absorption is described by,

$$R_{abs} = P_{ads}\frac{\bar{\nu_x}}{2V}N_0 e^{-(t/T_{abs})}. \tag{7.4}$$

Hence, the overall spin lattice relaxation rates of the ^{129}Xe in the free gas and absorbed states are not as straightforward as those described by equ 3.16. The T_1 of the free gas is determined by the spin lattice relaxation of the gas in the free state plus the relaxation of any nuclei that have been adsorbed and desorbed from the toluene, within which the spin lattice relaxation will be at a different rate. Likewise, the relaxation rate of the ^{129}Xe within the

---

[2] In our experiments, the absorption capacity of the toluene is seven fold the quantity of Xe used in the worst case.

toluene will have a contribution from desorbed and readsorbed nuclei which will have been subject to the free gas relaxation rate. At the steady state of Xe transfer condition, the effects of these additional relaxation factors will remain constant and can be incorporated into the overall T_1 of the ^{129}Xe atoms in each state.

The absorption of ^{129}Xe into toluene has an affect on the signal between the initial introduction of hyperpolarised ^{129}Xe to the toluene ($t = 0$) until a steady state of absorption-desorption has been reached (at $t = t_{sorp}$). The manifestation of this in a plot showing the signal of polarised gas as it dissolves into a liquid, is that the data may be split into two regions; the earlier data showing a decay in signal due to the combination of absorption of gas into the liquid and the spin lattice relaxation of the free gas, and the latter data, with a decay dominated by the spin lattice relaxation of the remaining free gas. Accounting for the restricted affect of R_{abs} and incorporating the effect of equ 3.16 into equ 7.3, we get for the polarised ^{129}Xe gas,

$$S(t) = M_{z0} e^{\frac{-t}{T_1}} \times \left[N_0 e^{\frac{-t}{T_{abs}}} \right]_{t=0}^{t=t_{sorp}} \tag{7.5}$$

given that the maximum possible signal is the product of the magnetisation of the gas M_z and the number of free gas atoms N at $t = 0$. Similarly for the ^{129}Xe dissolved in the toluene we get,

$$S(t) = M_{z0} e^{\frac{-t}{T_1}} \times \left(N_{0Liq} + \left[N_{0Gas} (1 - e^{\frac{1}{T_{abs}}}) \right]_{t=0}^{t=t_{sorp}} \right). \tag{7.6}$$

The model of the signal from the free gas phase of ^{129}Xe inside the toluene impregnated SG0 sample was fitted to the data obtained from the sample when filled with 2.582 ml and 5.935 ml of toluene (fig 7.11). Unfortunately the limited number of data points means that the absorption time constants

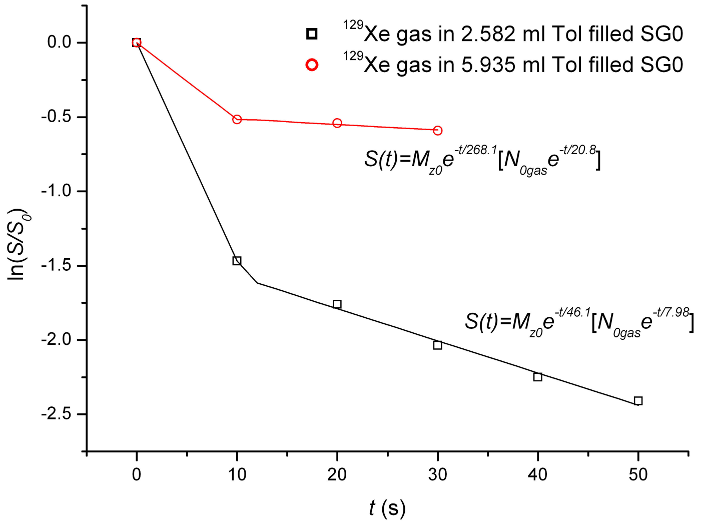

Figure 7.11: Model described by equ 7.5 fitted to data for the signal from the free ^{129}Xe inside the toluene filled SG0 sample over time. The absorption phase model is applied between $t = 0$ and $t = 10$ s.

for the gas in the presence of 2.582 ml and 5.935 ml of toluene (which are 7.98 and 20.8 s respectively) should be considered as the upper limits. However, it is possible to see a clear distinction between the free gas relaxation times in the two similar environments. Counter intuitively, the free ^{129}Xe in SG0 impregnated with the lower amount of toluene, has the shortest T_1, despite more free space being available for the gas to reside and hence a lower relaxation rate due to wall collisions. No satisfactory explanation of this observation could be made from this data.

Unfortunately, due to a low SNR and the damage to the SG0 sample holder caused by the toluene, the number of data points obtained were too few to reliably fit the model described in equ 7.6 to the decay of signal from the ^{129}Xe dissolved in the toluene.

Chapter 8

Conclusions

The need for hyperpolarised gases in both medical and materials sciences has been highlighted in the introduction to this thesis, with special emphasis on the potential roles of hyperpolarised ^{129}Xe and its advantages over ^{3}He. Having considered the theory of optical polarisation and reviewed recent developments, we have designed and built an intermediate pressure (0.6 - 3 bar) spin exchange polariser for the hyperpolarisation of ^{129}Xe gas. In this pressure regime we gain a significant reduction in the relaxation rate of the polarised gas. We are also able to employ the use of cylindrical polarisation cells which offer better optical transmittance than high pressure spherical cells.

We have described the first use of a volume holographic grating (VHG) frequency narrowed high power laser diode as the optical pumping source for hyperpolarised gases. The VHG device has permitted a significant reduction in the length of the optical setup required for frequency narrowing the laser spectrum in comparison to the external cavity diode laser arrangement. Also, laser line widths of 0.21 ± 0.01 nm have been achieved with 35 W of optical power coupled into the SEOP cell.

The effect that four major operational parameters (temperature, laser power, gas pressure and gas flow rate) have on gas polarisation have been investigated and discussed. The effect of laser induced thermal runaway has been measured for the first time by comparison of experimental results to those produced by a computational model [91]. It is necessary to account for heating of the Rb vapour by high powered laser devices when designing a SE polariser. As more high powered laser diode arrays are incorporated into SE polarisers, more work on the characterisation of laser induced thermal runaway is strongly advisable.

A maximum polarisation of 34 ± 3 % was achieved in ^{129}Xe gas contained in our cylindrical flow cell at 2.5 bar gas pressure and heated to 120 °C. In a pseudo batch-flow mode, the magnetisation of the ^{129}Xe gas can exceed 80 % sccm under optimum conditions. High nuclear polarisations in the gas are made possible by coating the cell walls in an OTS solution which results in reduced relaxation via wall collisions.

We imaged various quantities of polarised ^{129}Xe gas inside a 0.15 T whole body MRI scanner. The resolution and signal to noise of these images are high enough to distinguish clearly the shape and depth of the gas container. The diffusion of ^{129}Xe gas was measured within a gas mixture and the free gas diffusion constant calculated using published results.

A T_1 measurement of hyperpolarised ^{129}Xe inside a human lung during a single breath hold was made. The measured T_1 of 27.6 ± 4.4 s for hyperpolarised ^{129}Xe gas within the lungs defines the time scale future studies of this difficult to probe environment. Unfortunately we were unable to obtain an MR image from hyperpolarised ^{129}Xe gas inside a human lung within the scope of this thesis. The inability to obtain an MR image from within the lung was attributed to poor signal pick-up from our RF receive coil. A new coil is needed to perform lung space imaging using hyperpolarised ^{129}Xe within the 0.15 T whole body MRI scanner.

Dissolved solution NMR was successfully performed using hyperpolarised ^{129}Xe in olive oil and toluene. The chemical shift and T_1 of polarised ^{129}Xe in these two liquids was measured and found to agree with published literature. An MR image of hyperpolarised ^{129}Xe dissolved in toluene was achieved with a signal to noise ratio of 60. Implications of the high NMR signal achieved from hyperpolarised ^{129}Xe in liquid include the tracking of ^{129}Xe in the bloodstream after injection or perfusion through the lungs.

Hyperpolarised ^{129}Xe was introduced into a toluene filled sample of sintered glass with the intention of characterising the porosity of the sample. Chemical attack by the toluene on the sample holder prevented extensive studies of the sintered glass. However, by tracking the decay and growth of the ^{129}Xe NMR signal in the dissolved and free gas state, it was possible to deduce the rate of absorption of gas into the liquid. It is hoped that this may be used to characterise porosity of zeolites.

The very short T_1 of hyperpolarised ^{129}Xe inside silica gel prevents characterisation of the material at 0.15 T. It is predicted that repeating the experiment inside a high field NMR spectrometer will increase the signal to noise, facilitating more accurate measurements on this short time scale.

This project has successfully produced a world class ^{129}Xe hyperpolarisation facility and explored a number of possible and feasible applications of the polarised gas. A continuation of this work will focus on the characterisation of porous materials using a continuous flow of hyperpolarised ^{129}Xe gas through a high field NMR spectrometer. Perfection of a Xe freeze out system will facilitate the collection of larger quantities and more concentrated hyperpolarised ^{129}Xe with no buffer gases for studies on large porous samples or human lung spaces. For increases in the magnetisation production factor of the SEOP apparatus, further matching of the laser beam shape to cell geometry should be a priority. In the long term, modification of the SEOP apparatus to operate in the low pressure regime should be considered.

Appendix A

Temperature Controller Circuit Diagram

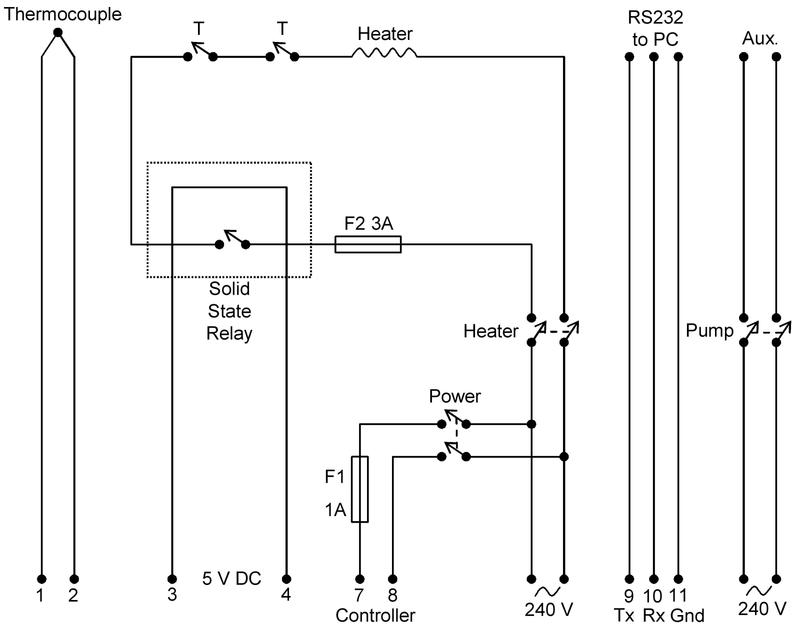

NB. Numbered terminals are connected to corresponding terminals on temperature controller. Switches labelled ‘T’ refer to bi-metal safety triggers.

Appendix B

Delta z Coil Model

The use of sine theta coils has been documented for B_0 holding fields of circular cross section. The requirement of the system to vary the current between adjacent coils leads to numerable power supplies or intricate electronics design, which are not necessarily suitable for portable cavities and certainly not convenient for NMR coil designs. Below we present a model for a 'delta z' coil, having coils of common current but a varying separation angle, ϕ, and though exhibiting lower homogeneity, provides a field of greater magnitude based on a fixed maximum current.

The magnetic field, B_z, due to a current loop at some distance, z, along the z-axis is given by,

$$B_z = \frac{\mu_0}{2} \frac{IR^2}{(Z^2 + R^2)^{3/2}} \tag{B.1}$$

where I = current and R = the radius of the loop.

For a sine theta coil around a cavity of radius r, the current and radii of loops vary with $I_{max}sin(\theta)$ and $rsin(\theta)$ respectively, where $\theta = n\phi - \phi/2$ for the n^{th} turn and where $\phi = 180/n_{max}(n - 1/2)$. Therefore equation B.1 can be re-written for this case as,

$$B_z(n) = \frac{\mu_0}{2}\frac{I(n)(R(n))^2}{(Z^2+(R(n))^2)^{3/2}}. \tag{B.2}$$

If instead of varying the angle between adjacent current loops by ϕ, we vary the axial spacing by Δz whilst keeping the current common, this equation becomes,

$$B_z(n) = \frac{5\mu_0}{16}\frac{I(R(n))^2}{(Z^2+(R(n))^2)^{3/2}} \tag{B.3}$$

where,
$R(n) = \sqrt{r^2-(1-z(n))^2}$,
$z(n) = n\Delta z - \Delta z/2$
and $\Delta z = r((n_{max}+1)/n_{max} - 2n/n_{max}$.

As the current in each loop of the 'delta z' coil is I_{max} then the central field of this formation is greater than that of the sine theta arrangement. In fact, as $n \rightarrow \infty$, $\frac{B_{\Delta z}}{B_{sin(\theta)}} \rightarrow \frac{\pi}{2}$ in the centre of the cavity.

A comparison of fields produced by mathematical model for the sine theta and 'delta z' coils is presented in fig B.1.

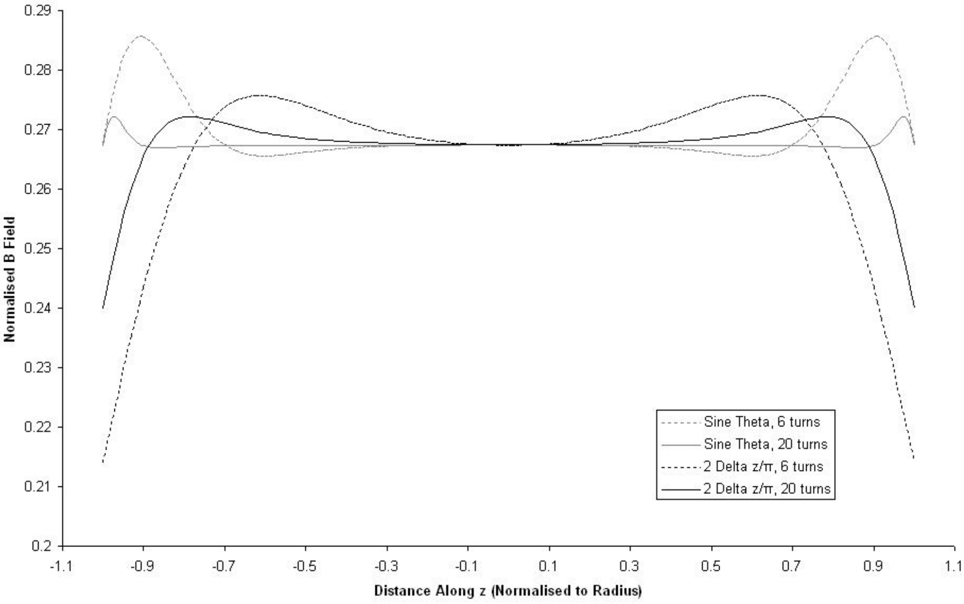

Figure B.1: A comparison of calculated fields produced by sine theta and 'delta z' coils in identical cavities for 6 and 20 turn arrangements. The models are normalised against n and the 'delta z' results divided by a factor of $\pi/2$. A small trade-off in homogeneity for greater simplicity and central field is made for the 'delta z' coil in comparison to the sine theta design.

Bibliography

[1] Anthony P, Arnold R, Band H, Borel H, Bosted P, Breton V, Cates G, Chupp T, Dietrich F, Dunne J, Erbacher R, Fellbaum J, Fonvieille H, Gearhart R, Holmes R, Hughes E, Johnson J, Kawall D, Keppel C, Kuhn S, Lombard-Nelsen R, Marroncle J, Maruyama T, Meyer W, Meziani Z-E, Middleton H, Morgenstern J, Newbury N, Petratos G, Pitthan R, Prepost R, Roblin Y, Rock S, Rokni S, Shapiro G, Smith T, Souder P, Spengos M, Staley F, Stuart L, Szalata Z, Terrien Y, Thompson A, White J, Woods M, Xu J, Young C, and Zapalac G. *Phys. Rev. Lett.*, **71**, 959, (1993).

[2] Wu Z-K, Happer W, Kitano M and Daniels J. *Phys. Rev. A*, **42**, 2774, (1990).

[3] Raftery D, Long H, Meersmann T, Grandinetti P, Reven L and Pines A. *Phys. Rev. Lett.*, **66**, 584, (1991).

[4] Newbury N, Barton A, Bogorad P, Cates G, Gatzke M, Saam B, Han L, Holmes R, Souder P, Xu J and Benton D. *Phys. Rev. Lett.*, **67**, 3219, (1991).

[5] Chupp T, Hoare R, Walsworth R and Bo Wu. *Phys. Rev. Lett.*, **72**, 2363, (1994).

[6] Thompson A, Bernstein A, Chupp T, DeAngelis D, Dodge G, Dodson G, Dow K, Farkhondeh M, Fong W, Kim J, Loveman R, Richardson J, Schmieden H, Tieger D, Yates T, Wagshul M and Zumbro J. *Phys. Rev. Lett.*, **68**, 2901 , (1992).

[7] Stoltz E, Meyerhoff M, Bigelow N, Leduc M, Nacher P-J and Tastevin G. *Appl. Phys. B*, **63**, 629, (1996).

[8] Kastler A. *J. Phys. Radium*, **11**, 255, (1950).

[9] Kastler A. *Physica*, **3-4**, 191, (1951).

[10] Bouchiat MA, Carver TA and Varnum CM. *Phys. Rev. Lett.*, **5**, 373, (1960).

[11] Walker TG and Happer W. *Rev. Mod. Phys.*, **69**, 629, (1997).

[12] Oros AM and Shah NJ. *Phys. Med. Biol.*, **49**, 105-153, (2004).

[13] Appelt S, Ben-Amar Baranga A, Erickson C, Romalis M, Young A and Happer W. *Phys. Rev. A*, **58**, 1412, (1998).

[14] Goodson BM. *J. Magn. Reson.*, **155**, 157, (2000).

[15] Cherubini A and Bifone A. *Prog. Nucl. Mag. Res. Sp.*, **42**, 1, (2003).

[16] Hersman FW and Ruset IC. *Design, Implementation, Performance and Numerical Simulation of Low-Pressure High-Flow Xenon Polariser.* Xe-Mat. May 2003, France.

[17] Dabbs JWT and Roberts LD. *Phys. Rev. Lett.*, **95**, 307, (1954).

[18] Chann B, Babcock E, Anderson L, Walker T, Chen W, Smith T, Thompson A and Gentile T. *J. Appl. Phys.*, **94**, 6908, (2003).

[19] Ruth U. *Appl. Phys. B.*, **68**, 93, (1999).

[20] Driehuys B, Cates G, Miron E, Sauer K, Walter D Happer W. *Appl. Phys. Lett.* **69**, 1668, (1996).

[21] Wittgrefe F, Hoogerland MD and Woerdman J P. *Meas. Sci. Technol.* **2**, 304, (1991).

[22] Chann B, Nelson I and Walker TG. *Opt. Lett.*, **25**, 1352, (2000).

[23] Wieman C and Hollbeg L. *Sci. Instrum.*, **62**, 1, (1991).

[24] Romalis MV. *Appl. Phys. Lett.*, **77**, 1080, (2000).

[25] Nelson I, Chann B and Walker TG. *Appl. Phys. Lett.*, **76**, 1356, (2000).

[26] Babcock ED. *PhD Thesis.* Spin Exchane Optical Pumping with Alkali-Metal Vapours. University of Wisconsin-Madison, USA. 2005.

[27] Volodin B, Dolgy S, Downs E, Melnik E, Ban V and McIntyre E. *Upgrading Performance of High Power Laser Diodes and Arrays With LuxxMaster^{TM} Wavelength Stabilization.* White Paper, **PD-LD Inc.**, New Jersey, 2003.

[28] Volodin B, Dolgy S, Melnik E and Ban V. *A New Platform Technology for WDM Applications.* White Paper, **PD-LD Inc.**, New Jersey, 2003.

[29] Woolley EB, Barlow MJ and Owers-Bradley J. *Improved Spin Exchange Optical Pumping of ^{129}Xe using a Volume Holographic Grating Narrowed Laser Diode.* Poster presented at XeMat *III*, Ottawa, 2006.

[30] Barden S. *Volume Phase Holographic Gratings.* **NOAO**, Arizona, 1998.

[31] *Volume Holographic Gratings (VHG).* White Paper, **Ondax Inc.**, California, 2005.

[32] Zeng X, Wu Z, Call T, Miron E, Schreiber D and Happer W. *Phys. Rev. A.*, **31**, 260-278, (1985).

[33] Jau Y-Y, Kuzma NN and Happer W. *Phys. Rev. A.*, **69**, 1-4, (2004).

[34] Baranga A-BA, Appelt S, Romalis M, Erickson C, Young A, Cates G and Happer W. *Phys. Rev. Lett.*, **80**, 2801-2804, (1998).

[35] Borel I, Sogaard L, Svendsen W and Andersen N. *Phys. Rev. A.*, **67**, 062705, (2003).

[36] Levron D, Walter D, Appelt S, Fitzgerald R, Kahn D, Korbly S, Sauer K, Happer W, Earles T, Mawst L, Botez D, Harvey M, DiMarco L, Connolly J, Mller H, Chen X, Cofer G and Johnson G. *Appl. Phys. Lett.*, **73**, 2666, (1998).

[37] Babcock E, Nelson I, Kadlecek S, Driehuys B, Anderson L, Hersman F and Walker T. *Phys. Rev. Lett.*, **91**, 123003, (2003).

[38] Serkland D, Peake G, Geib K, Lutwak R, Garvey R, Varghese M and Mescher M. VCSELs for Atomic Clocks. *Proceedings of SPIE – Volume 6132*, (2006).

[39] Ruset IC, Ketel S and Hersman FW. *Phys. Rev. Lett.*, **96**, 053002, (2006).

[40] Killian TJ *Phys. Rev.*, **27**, 578, (1926).

[41] Lide D *ed. CRC Handbook of Chemistry and Physics 83rded.*, The Chemical Rubber Co., Florida. (2002).

[42] Barrat JP, Brossel J and Kastler A. *Compt. Rend.*, **239**, 1196, (1954).

[43] Kadlecek SJ. *PhD Thesis.* Spin Relaxation In Alkali Vapours. University of Wisconsin-Madison, USA. 1999.

[44] Happer W, Miron E, Schaefer S, Schreiber D, van Wijngaarden W and Zeng X. *Phys. Rev. A.*, **29**, 3092, (1984).

[45] Shao W. *PhD Thesis.* Studies and Applications of Hyperpolarised ^{129}Xe. California Institution of Technology, USA. 2004.

[46] Wagshul ME and Chupp TE. *Phys. Rev. A.*, **40**, 4447, (1989).

[47] Fukutomi J *J. Magn. Reson.*, **160**, 26, (2003).

[48] Zook AL, Adhyaru BB and Bowers CR. *J. Magn. Reson.*, **159**, 175-182, (2002).

[49] Moudrakovski IL, Breeze S, Simard B, Ratcliffe C, Ripmeester J, Seideman T, Tse J and Santyr G. *J. Chem. Phys.*, **114**, 2173, (2001).

[50] Pfeffer M and Lutz O. *J. Magn. Reson.*, **108**, 106, (1994).

[51] Chann B. *PhD Thesis.* Studies of Spin Exchange Optical Pumping. University of Wisconsin-Madison, USA. 2003.

[52] Purcell EM, Torrey HC and Pound RV. *Phys. Rev. Lett.*, **69**, 37, (1946).

[53] Bloch F, Hansen WW and Packard M., *Phys. Rev. Lett.*, **69**, 127, (1946).

[54] Levitt MH., 2001, *Spin Dynamics*, John Wiley & Sons, West Sussex, UK.

[55] Fukushima E and Roeder SBW., 1981, *Experimental Pulse NMR: A Nuts and Bolts Approach*, Westview Press, USA.

[56] Wong G, Tseng C, Pomeroy V, Mair R, Hinton D, Hoffmann D, Stoner R, Hersman F, Cory D and Walsworth R. *J. Mag. Res.*, **141**, 217, (1999).

[57] Autschbach J and Zurek E. *J. Phys. Chem. A.*, **107**, 4967, (2003).

[58] Stapf S and Han S-I. *Eds.* 2006, *NMR Imaging in Chemical Engineering*, Wiley-VCH, Weinhiem.

[59] Hahn EL. *Phys. Rev.*, **80**, 580, (1950).

[60] Mansfield P and Grannel PK. *J. Phys.*, **6**, 422, (1973).

[61] Lauterbur PC., *Nature*, **242**, 190, (1973).

[62] Alexander AL., *MR Imaging with 3D Fast Spin Echo Using Projection Reconstruction: Technique, Description and Applications* Nuclear Science Symposium Proceedings. **2**, 1087, (1999).

[63] Mair RW, Wong G, Hoffmann D, Hrlimann M, Patz S, Schwartz L and Walsworth R. *Phys Rev Lett.*, **83**, 3324, (1999).

[64] Driehuys B, Cofer G, Pollaro J, Mackel J, Hedlund L and Johnson G. *PNAS.*, **103**, 18278, (2006).

[65] Stejskal EO and Tanner JE. *J. Chem. Phys.*, **42**, 288, (1965).

[66] Waters B. *PhD Thesis.* Imaging the Lungs using Hyperpolarised ^{3}He. University of Nottingham, UK. 2006.

[67] Mair RW, Hoffmann D, Sheth S, Wong G, Butler J, Patz S, Topulos G and Walsworth R. *NMR Biomed.*, **13**, 229, (2000).

[68] Tastevin G and Nacher J-P. *J. Chem. Phys.*, **123**, 064506, (2005).

[69] PD-LD Inc., *Optical alignment for wavelength locking by use of a LuxxMaster^{TM} element* [online]. Available at: <http://www.pdld.com/pdf/VBGAlignmentProcedure100703.pdf> [Accessed 14 May 2007].

[70] Chann B, Babcock E, Anderson L and Walker T. *Phys. Rev. A*, **66**, 033406, (2002).

[71] Barlow MJ., *Private communication.*

[72] CVCP, 1992, *Safety in Universities: Notes of Guidance. Part 2:1 Lasers.*

[73] Zhu H, Ruset IC and Hersman FW., *Opt. Lett.*, **30**, 1342, (2005).

[74] Cacak RK and Craig JR. *Rev. Sci. Instrum.*, **40**, 1468-1470, (1969).

[75] Barker JR. *J. Sci. Instr. Phys. Ind.*, **26**, 273-275, (1949).

[76] Caprari RS. *Meas. Sci. Technol.*, **6**, 593-597, (1995).

[77] Alldred JC and Scoller I. *J. Sci. Instrum.*, **44**, 755-760, (1967).

[78] Merritt R, Purcell C and Stronik G. *Rev. Sci. Instrum.*, **54**, 879-882, (1983).

[79] Rudd ME and Craig JR. *Rev. Sci. Instrum.*, **39**, 1372-1374, (1968).

[80] Daniels JM, Kiang ACK and Kirkby P. *Can. J. Phys.*, **49**, 576-581, (1970).

[81] Hanson RJ and Pipkin FM. *Rev. Sci. Instrum.*, **36**, 179-188, (1965).

[82] Ohanian HC. *Physics.* 2nd ed. W. W. Norton & Co. 1998.

[83] Dennison E. 2005. Axial Field of a Real Helmholtz Coil Pair [online]. Available at: <http://www.netdenizen.com/> [Accessed 24 June 2005].

[84] Ruset IC. *PhD Thesis.* Hyperpolarised ^{129}Xe Production and Applications. University of New Hampshire, USA. 2005.

[85] Rich D, Gentile T, Smith T, Thompson A and Jones G. *Appl. Phys. Lett.*, **80**, 2210, (1980).

[86] Boag S, Parnell S, Frost C, Andersen K and Babcock E. Demonstration of the use of polarised ^{3}He as a broadband polariser on a pulsed time-of-flight neutron source., *Physica B., In Preparation.*

[87] Walsworth R. Coating Glass Cells with OTS [online]. Available at: <http://www.cfa.harvard.edu/Walsworth> [Accessed 29 May 2006].

[88] Fichele S. *PhD Thesis.* Hyperpolarised ^{3}He Gas Production for Magnetic Resonance Imaging of the Human Air-Ways. The University of Nottingham, UK. 2002.

[89] Parnell S, Woolley E, Boag S and Frost C. Digital Pulsed NMR Spectrometer for Nuclear Spin-Polarised ^{3}He and Other Hyperpolarised Gases. *In preparation.*

[90] Wu Z-K, Kitano M, Happer W, Hou W and Daniels J. *Appl. Opt.* **25**, 4483, (1986).

[91] Cherubini A. Numerical Evaluation of ^{129}Xe Nuclear Polarisation in an Optical Pumping System [online]. Available at: <http://www.btrp-hyperpolarised.ac.uk/dec2004/ICR3.ppt/> [Accessed 03 November 2007].

[92] Doebler H and Kamke B. *Z. Physik A.*, **280**, 111, (1977).

[93] Fink A, Baumer D and Brunner E., *Phys. Rev. A.*, **72**, 053411, (2005).

[94] Driehuys B., *Imaging Pulmonary Gas Exchange Using Hyperpolarized* ^{129}*Xe MRI* International Workshop on Functional Lung Imaging. September 2006, Pennsylvania.

[95] Mugler III J, Driehuys B, Brookeman J, Cates G, Berr S, Bryant R, Daniel T, De Lange E, Hunter Downs J, Erickson C, Happer W, Hinton D, Kassel N, Maier T, Phillips C, Saam B, Sauer K and Wagshul M. *Mag. Reson. Med.*, **37**, 809, (1997).

[96] Saam B, Happer W and Middleton H. *Phys. Rev. A*, **52**, 862, (1995).

[97] Bloembergen N, Purcell EM and Pound RV., *Phys. Rev.*, **73**, 679, (1948).

[98] Cowan B, El-Nasr L, Fardis M and Hussain A. *Phys. Rev. Lett.*, **58**, 2308, (1987).

[99] Tofts P *ed. Quantitative MRI of the Brain.* John Wiley and Sons, Chichester. (2003).

[100] Hunt ER and Carr HY., *Phys. Rev.*, **130**, 2302, (1963).

[101] Ruppert K, Brookeman J, Hagspiel K, Driehuys B and Mugler III J. *NMR. Biomed.*, **13**, 220, (2000).

[102] Ruan C. 2003. *MRI Artefacts: Mechanism and Control* [online]. Available at: <http://ric.uthscsa.edu> [Accessed 29 March 2007].

[103] Waldman A, Rees J, Brock C, Robson M, Gatehouse P and Bydder G. *Neuroradiology*, **45**, 887, (2003).

[104] Mair R, Cory D, Peled S, Tseng C-H, Patz S and Walsworth R. *J. Magn. Reson.*, **135**, 478, (1998).

[105] Bidinosti C, Choukeife J, Nacher P-J and Tastevin G. *J. Magn. Reson.*, **162**, 122, (2003).

[106] Rust DR. 1998. *Pressure Dependence of Leakrate in 1997 Beam Test Prototype TRT Barrel Model* [online]. Available at: <http://hep.physics.indiana.edu> [Accessed 04 April 2007].

[107] Kaiser L, Meersmann T, Logan J and Pines A. *PNAS.*, **97**, 2414, (2000).

[108] Acosta R, Agulles-Pedros L, Komin S, Sebastiani D, Spiess H and Blumler P. *Phys. Chem. Chem. Phys.*, **8**, 4182, (2006).

[109] Wolber J, Cherubini A, Leach M, Bifone A. *NMR Biomed.*, **13**, 234, (2000).

[110] Terskikh VV, Mudrakovski IL and Mastikhin VM., *J. Chem. Soc. Faraday. Trans.*, **89**, 4239, (1993).

[111] Terskikh VV, Moudrakovski I, Breeze S, Lang S, Ratcliffe C, Ripmeester J and Sayari A. *Langmuir*, **18**, 5653, (2002).

[112] Pietrass T, Bifone A and Pines A *Surf. Sci.*, **334**, 730, (1995).

[113] Knagge K, Smith J, Smith L, Buriak J and Raftery D. *Solid State Nucl. Mag.*, **29**, 85, (2006).

[114] Wang R, Mair R, Rosen M, Cory G and Walsworth R. *Phys. Rev. E.*, **70**, 026312, (2004).

[115] Butler J, Mair R, Hoffmann D, Hrovat M, Rogers R, Topulos G, Walsworth R and Patz S. *J. Phys. Condens. Matter*, **14**, 297, (2002).

[116] Appelt S, Hasing F, Kuhn H, Perlo J and Blumich B. *Phys. Rev. Lett.*, **94**, 197602, (2005).

[117] Miller K, Reo N, Uiterkamp A, Stengle D, Stengle T and Williamson K. *Proc. Natl. Acad. Sci. USA*, **78**, 4946, (1981).

[118] Jameson CJ., *J. Chem. Phys.*, **63**, 5296, (1975).

[119] Acosta R, Blumler P, Han S, Appelt S, Hasing F, Schmiedeskamp J, Heil W and Spiess H. *Mag. Res. Imag.*, **22**, 1077, (2004).

[120] Månsson S, Johansson E, Svensson J, Olsson L, Stflahlberg F, Petersson J and Golman K. *Acta Radiologica*, **43**, 455, (2002).